Universitetet i Stavanger

Faculty of Science and Technology

MASTER'S THESIS

Study program/Specialization: Petroleum Engineering/Natural Gas Technology	Spring semester, 2017 Confidential
Writer: KINGSLEY AZUATALAM	…… (Writer's signature)
Faculty supervisor: Prof. Zhixin Yu Co-Supervisor: Dr. Fengliu Lou	
Thesis title: Preparation of Activated Carbon from Biomass for High Performance Supercapacitors	
Credits (ECTS): 30	
Key words: Activated Carbon Supercapacitor Surface area and porosity Electrochemical Performance Scanning Electron Microscopy Waste Paper	Pages: 91 + enclosure: 0 Stavanger, 15.06.2017

Abstract

Activated carbon was successfully synthesized from waste paper by physical, chemical and a combination of both activation procedures. The chemically activated carbon samples was achieved by using H_3PO_4 and KOH as agents. The samples exhibited hierarchical pore structures, and showed adsorption isotherms range from type 1 to type 5. The samples were analysed by Nitrogen Physisorption to determine the surface area and pore size distribution, and characterization by Scanning electron microscopy (SEM) examinations with energy dispersive x-ray spectroscopy (EDX) to study the surface morphology. The achieved activated carbon had surface area of $1014\,m^2/g$, with a narrow pore size distribution (of about 2 nm). In addition to this, the SEM and EDX results shows that samples with irregular pore size distribution and low surface area had other major elements in their structure asides from the usual carbon, calcium and oxygen.

When utilized as electrode material to evaluate their capacitive performance, the samples presented impressive rate capabilities, as a result of high values of specific capacitance (114 F/g), and energy density (26.7 Wh/Kg). These numbers were considerably higher than that obtained from a state-of the art reference material (106 F/g and 24.84 Wh/Kg). From the analysis, we can easily decipher that a temperature of 850 °C and Potassium hydroxide for 60 - 120 minutes gives the best results.

Acknowledgements

I would like to acknowledge Professor Zhixin Yu and Dr. Fengliu Lou, two individuals with finesse and great academic prowess, for guiding and supporting me through this field of electrochemical engineering. Also the staff of Beyonder AS has been an amazing team to work with. I would also like to thank PhD candidate Donald Azuatalam who was of immense help, to introduce and guide me through the use of latex in so few days. Finally, all thanks goes to God for making everything possible.

Contents

List of Figures

List of Tables

Abbreviations

2D Two Dimensional

3D Three Dimensional

BET Brunauer-Emmett-Teller

CNT Carbon nano tubes

CuO Copper II Oxide

EDL Electrical Double layer

EDX Energy-dispersive X-ray spectroscopy

EIA U.S. Energy Information Administration

KOH Potassium Hydroxide

LNG Liquefied Natural Gas

nm Nanometre

REDOX Oxidation Reduction

SEM Scanning Electron Microscope

Nomenclature

ΔV : Voltage change

C : capacitance of the supercapacitor/Specific Capacitance

c : Constant

m : Mass of cell

P : Adsorbate Pressure/N_2 Partial Pressure

P_0 : Gas saturation pressure

P_d : Power density

R : Cell resistance

t : Time in seconds

V : Voltage of the Supercapacitor

V_a : Gas adsorbed volume at Pressure, P

V_m : Gas Volume required to form monolayer

W_{TS} : Total weight

Z : Energy stored by supercapacitor

Chapter 1

Introduction

1.1 Background

Over two centuries ago, Alessandro Volta invented the Voltaic pile. This was a sequel development to an 'animal electricity' observation made by Galvani in 1786. Volta could demonstrate to the public that joining two metal disk plates to an alkaline soaked cloth, electricity could be generated. However, other sources believe that there was an earlier battery in existence in the city of Baghdad [26–29].

The late 1880's saw the emergence of electricity as the best energy form, and since then, there has been an insatiable increase in the demand for electrical energy. The EIA reports that there would be an estimated 139% increase in the demand for electricity in 2035 from the 1980 value [30]. This increase stems from respective reasons such as: the need for cleaner energy, projected increase in fuel cost, accessibility to energy resources, and the development of portable electronics [28]. Some of this energy needs to be used immediately, or must be stored for later use. Plants store energy in form of starch to be used in later stages, but animals do this differently. Humans, as even higher animals have a way of managing this deficit externally; the use of a storage device, a battery.

As the most electropositive and lightest metal, Lithium fits as a perfect candidate for batteries [22]. Lithium ion batteries have become popular in this dispensation because of their ability to store large energy volumes. This is referred to as having large energy density. However, retrieving this energy per unit mass at a later stage is not so easy. Supercapacitors however, have the opposite, a smaller storage space, and a high-power density. To mitigate this conundrum, a hybrid supercapacitor was created. This was achieved by replacing the metal oxide in the cathode of the lithium ion battery with activated carbon. This action improves power density but decreases energy density. To improve the energy density, we replace the activated carbon in the anode of the supercapacitor with graphite. These modifications would enhance

the ability of the hybrid supercapacitor to dissipate enough power and contain larger volume of energy. Also, this device would be safer and more environmentally friendly because the metal oxide electrode is replaced with activated carbon.

Over 85% of adults subscribe to news from papers daily in Norway. Stavanger Aftenblad recorded 68000 as its circulation figure for 2005 [31]. Since, the hybrid supercapacitor employs waste paper as its precursor material, it would ensure that there is an alternative way to utilize this wastepaper. There is a huge demand for batteries that meet these standards in the maritime sector and road transport, because the world strives towards a cleaner environment. The portable electronics space would also benefit from this development as devices would become much less hazardous to use. This project focuses on the procedures and steps involved in the preparation of activated carbon with the required pore size distribution, pore size and surface area. The produced activated carbon would be used as an electrode to power an electrochemical device, and its supercapacitive performance would be evaluated by galvanostatic charge and discharge tests.

1.2 Research Objectives

This research attempts to provide details on how to prepare activated carbon from an everyday waste material as precursor. To achieve this, the known preparatory methods are employed, plus a healthy blend of variations between them. Added to this, the effects of different parameters such as activation time, temperature, dehydrating agent, are considered. The surface area and pore size distribution of the produced activated carbon would be determined by nitrogen physisorption analysis procedure; also the morphology and structure of the produced samples were analysed by scanning electron microscopy (SEM). Furthermore, a supercapacitive performance evaluation would be carried out.

The objectives of this research project are listed as follows:

- To prepare activated carbon from waste newspaper as precursor material by physical and chemical activation procedures.
- To characterize the produced activated carbon by the Brauner Emmner and Teller analysis method.
- To carry out visual characterization of the samples using Scanning Electron Microscope.
- To optimize the surface area to more than $1500\,m^2/g$ and specific capacitance of 100 F/g
- To analyse the effects of different preparation agents on the produced activated carbon.

- To evaluate the supercapacitive performance of the samples by charge and discharge tests.

The interim targets of this research project are listed as follows:

- To perform literature review on the preparation of activated carbons.
- To identify details that affect this process.
- To learn how to use the nitrogen physisorption and how to operate the equipment therein.
- To provide an interim report for this process.

1.3 Research Scope

This study covers methods for preparing activated carbon from biomass, and focuses on how to modify these procedures to make the best activated carbon for supercapacitor application. It ventures into, but does not fully showcase the full details of the supercapacitor.

1.4 Thesis Contribution to Knowledge

This research work would provide an insight on how to use waste biomass material as precursor to produce activated carbons. Along this path, a lot of factors affecting this procedure would be considered, and their respective effects would be made known. Also, the performance of produced precursor in electrochemical devices would be evaluated.

1.5 Organization of Thesis

This thesis is composed of six chapters

Chapter 1: This chapter introduces the work, and gives an overview of the background, motivation and relevance of the study

Chapter 2: This chapter provides a review of literatures and theories behind this study, and is a decent repertoire for the understanding of this piece. The relevant terminologies applied are defined for proper understanding of the thesis

Chapter 3: This chapter introduces the methodology, in addition to tools and techniques that was used to achieve the results.

Chapter 4: The results of the analysis are shown in this chapter and discussed.

Chapter 5: Conclusion is made here and summarizing statements too.

Chapter 6: Suggestions for future work.

In the next chapter, the related scholarly publications will be reviewed, and their pros and cons will be analysed.

Chapter 2

Literature Review

2.1 The Energy Shift

A little more than six decades ago, coal was a principal element in the energy landscape, it was so relevant that it accounted for over half the energy needs of the world. Recently however, the supply of energy would no longer come from coal, because the carbon footprint of coal is relatively high [1, 32]. The figure 2.1 shows that the carbon footprint is highest for coal, but there are ways to cutback on this trend with carbon capture and storage.

There is a rising need to reduce the level of greenhouse gas emissions in our environment, so the world resorts to the use of cleaner forms of energy, such as wind, solar, hydro, biomass and even natural gas. Also, the Canadian oil sands and US shale gas revolution are other key details that control the demand and supply of energy [32].

The European Union made a remarkable decision to truncate the emission levels of Kyoto greenhouse gases to about 40% by 2030 [33, 34]. This sparked up actions directed towards the realisation of this target. Governments set up policies to foster this plan. Norway seems to be at the fore front of this development. For example, the Norwegian Government set out with some attractive incentives such as: provision of free public-charging stations, letting electric cars use the bus lanes, free toll, free public parking and tax reductions [2]. Because of this, individuals switched preferences to electric cars, hybrid vehicles, LNG vessels, and other machinery that emitted less carbon to the environment.

This decision propagated the proliferation of energy storage devices, as these plug-in Cars and portable electronics need energy on the go. A battery basically powers everything in the electric car for example, in contrast to powering just a few items on the regular gasoline automobiles. Figure 2.2 displays the increase of plug-in electric vehicles in Norway, which happens to be the country with the highest number of electric car users.

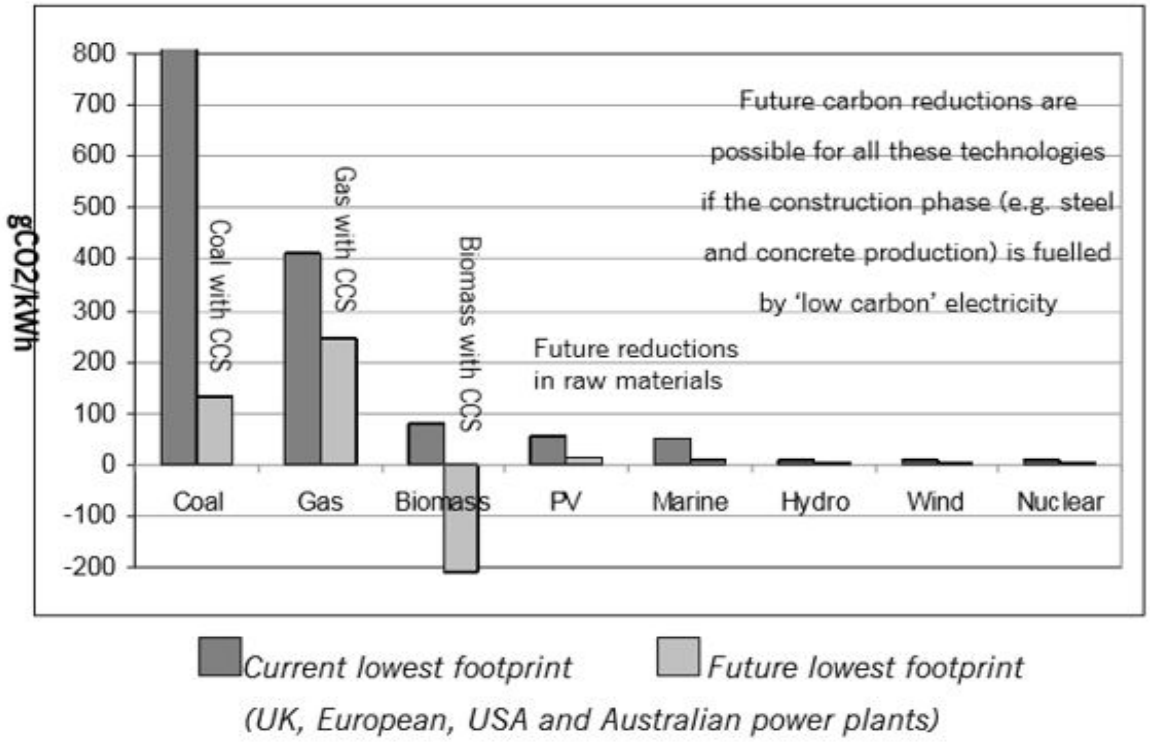

FIGURE 2.1: Range of carbon footprints for UK and European 'Low Carbon' Technologies [1]

.

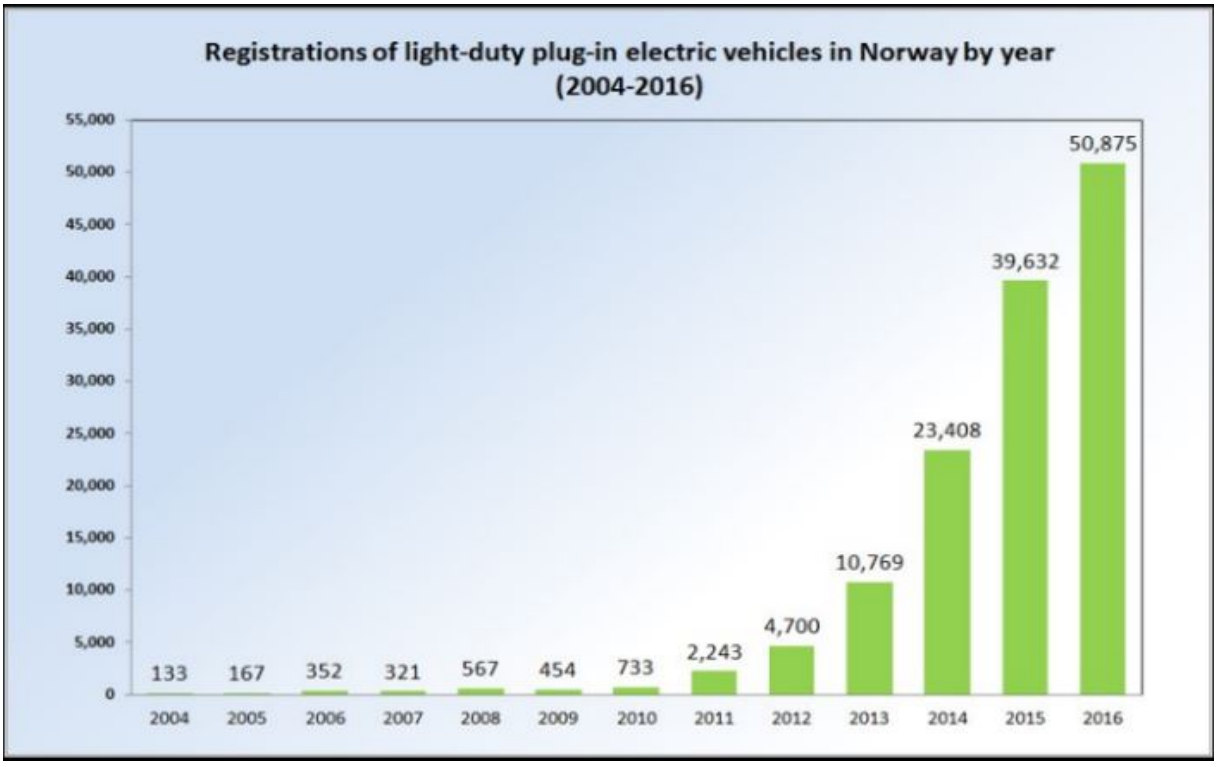

FIGURE 2.2: Registration of plug-in electric vehicles in Norway by year between 2004 and 2016 [2]

2.2 General Principles of Electrochemistry

2.2.1 Scope of Electrochemistry:

Electrochemistry as defined by Brett et. al[35] involves 'chemical phenomena associated with charge separation'. Rubinstein however thought it as a 'field of science that deals with the relation between electrical current or potential and chemical systems'[**?**]. Juxtaposing these definitions, we can decipher that Electrochemistry involves chemical phenomena that initiates charge movement. This movement, which occurs from one element to another in a REDOX reaction is known as electricity [35, 36]. It encompasses extents such as physical electrochemistry, bio electrochemistry analytical electrochemistry and electro organic chemistry. It also encroaches into applied areas such as corrosion, batteries, fuel cells, and solar energy conversion [37].

The features of electrode reactions: [37]

- They always involve transfer of electrons
- Heterogenous in nature
- The current indicates the rate of reaction
- It is like regular chemical kinetics in terms of reaction rate changes
- For current to move through an electro chemical cell, there must be a transition between electrical conductivity (in the electrodes) and ionic conductivity (in the solution)

Successful separation of charge at an electrode represents capacitance, while a charge transfer snag depicts resistance. Electrode reactions are always conveyed as reductions and has an associated standard electrode potential [35]. Jones [3], defined Standard Electrode Potential as the 'electrode potential (in volts) measured under standard conditions relative to the standard hydrogen electrode' He identified standard conditions as:

- Solutions with a concentration of 1.0 mol/dm^{-3}
- Gases at a pressure of 100 KPa
- Temperature of 298 K

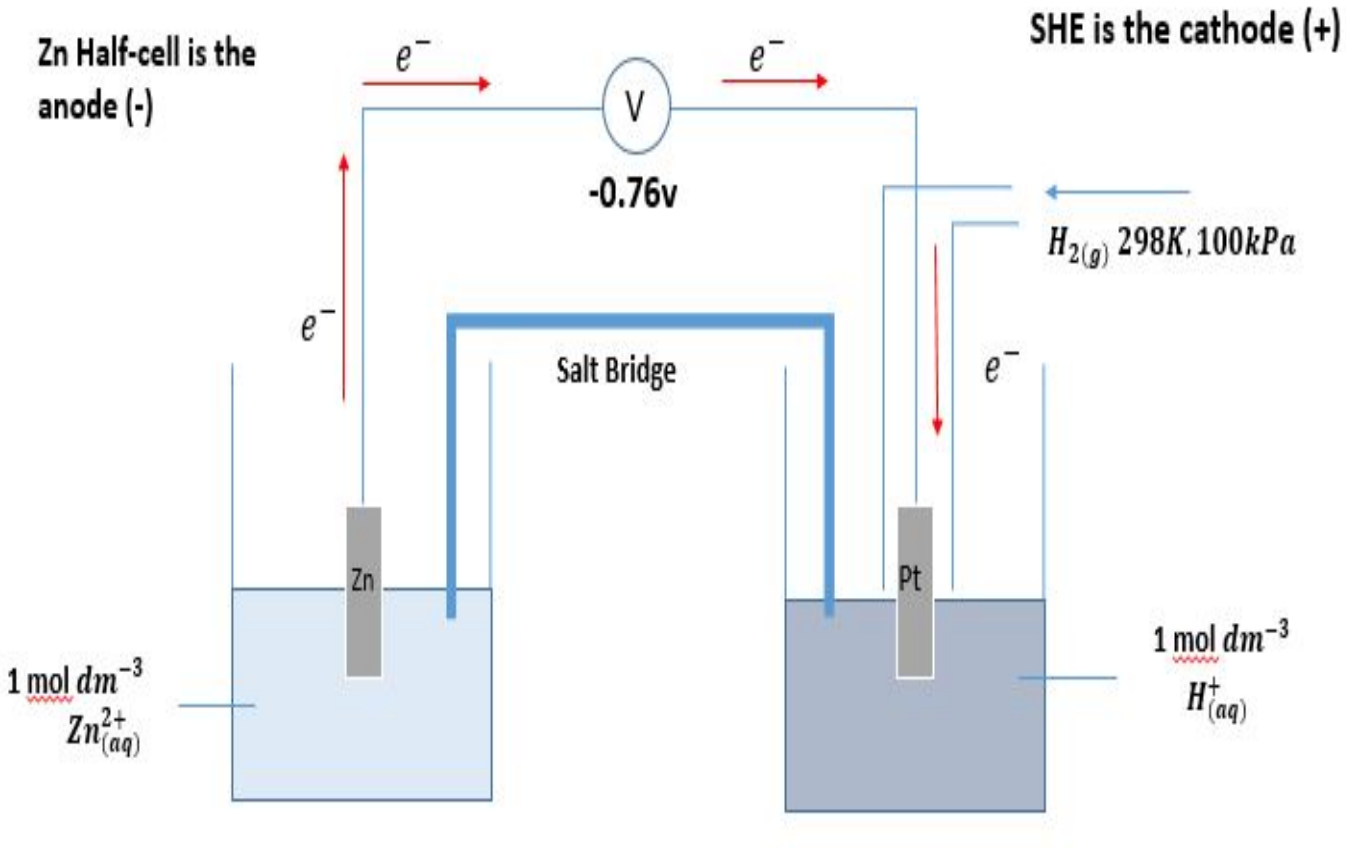

FIGURE 2.3: Schematic representation of Standard Electrode Potential [3]

As portrayed, the figure 2.3 shows a voltmeter V, at the center, a Zinc half-cell on the left which is connected by a wire and salt bridge to a standard hydrogen electrode on the right. Electrons would typically flow from the zinc half-cell to the standard hydrogen electrode because zinc is higher than hydrogen in the activity series. Oxidation reaction occurs at the anode, and is given as:

$$\mathrm{Zn(s)} \longrightarrow \mathrm{Zn^{2+}(aq)} + 2\,\mathrm{e^-} \tag{2.1}$$

Reduction occurs at the cathode:

$$2\,\mathrm{H^+(aq)} + 2\,\mathrm{e^-} \longrightarrow \mathrm{H_2(g)} \tag{2.2}$$

Combining both reactions, we can obtain the overall cell reaction as:

$$\mathrm{Zn(s)} + 2\,\mathrm{H^+(aq)} \longrightarrow \mathrm{Zn^{2+}(aq)} + \mathrm{H_2(g)} \tag{2.3}$$

The value which shows the standard electrode potential of the Zinc half-cell is -0.76V. For half-reactions at equilibrium, the relationship between potential E, and the standard electrode potential can be expressed by the Nernst equation [35].

2.2.1.1 Electrode Potential and Nernst Equation

A reaction mixture composition can be calculated from Gibb's energy. To demonstrate this, let's consider a simple zero order reaction:

$$\mathrm{A} \longleftrightarrow \mathrm{B} \tag{2.4}$$

Let's assume that an infinitesimal amount dξ of A is converted into B, the change in quantity of A & B present is:

$$dn_A = -d\xi \tag{2.5}$$

$$dn_B = +d\xi \tag{2.6}$$

The reaction would have a Gibbs free energy specified as:

$$\Delta G_r = \left(\frac{\partial G}{\partial \xi}\right)_{P,T} = \mu_B - \mu_A \tag{2.7}$$

Where: ξ = Extent of reaction and μ = Chemical potential or the specie's Gibbs free energy.

Forward and reverse reaction is spontaneous because μ varies with composition. This would imply that taking the derivative of (2.7) would result in the opposite effect, i.e:

$$\Delta G_r = 0 \tag{2.8}$$

This happens when $\mu_B = \mu_A$ and the natural consequence is that we can tell what the reaction mixture contains at equilibrium. To further buttress this point, let's consider a more open equation in (2.9)

$$\mathrm{aA} + \mathrm{bB} \longleftrightarrow \mathrm{cC} + \mathrm{dD} \tag{2.9}$$

If the reaction at (2.9) proceeds just by a small amount, dξ, the number of products and reactants is also expected to increase by:

$$\begin{aligned} dn_A &= -ad\xi \\ dn_B &= -bd\xi \\ dn_C &= +cd\xi \\ dn_D &= +dd\xi \end{aligned} \tag{2.10}$$

We can easily replicate the sets of equations above (2.10) with a general expression given as:

$$dn_J = -v_J d\xi \tag{2.11}$$

Where v_J = Stoichiometric number of J in chemical equilibrium

Gibbs energy would naturally be expected to change by an infinitesimal amount, at constant temperature and pressure, this results in:

$$dG = \mu_C dn_C + \mu_D dn_D + \mu_A dn_A + \mu_B dn_B = (c\mu_C + d\mu_D - a\mu_A - b\mu_B)d\xi \tag{2.12}$$

The common expression of (2.12) is:

$$dG = \Big(\sum_j v_J \mu_J\Big) d\xi \tag{2.13}$$

This leads to:

$$\Delta G_r = \left(\frac{\partial G}{\partial \xi}\right)_{P,T} = c\mu_C + d\mu_D - a\mu_A - b\mu_B \tag{2.14}$$

Moving forward, it is evident that the chemical potential of species J connects with its activity by a_J

$$\mu_J = \mu_J^0 + RT\ln(a_J) \tag{2.15}$$

A similar expression can be placed into equation (2.13) for each species, and inserting into (2.16) gives rise to

$$\Delta G_r = c\mu_C^0 + d\mu_D^0 - a\mu_A^0 - b\mu_B^0 + RT\ln\left(\frac{a_C^c a_D^d}{a_B^a a_B^b}\right) = +RT\ln(Q) \tag{2.16}$$

Where Q = reaction quotient. At equilibrium, $\Delta G_r = 0$, then

$$K = \left(\frac{a_C^c a_D^d}{a_B^a a_B^b}\right) \tag{2.17}$$

Where K is the thermodynamic equilibrium constant. Furthermore, from (1.10)

$$\Delta G_r^0 = -RT\ln(K) \tag{2.18}$$

This equation gives the equilibrium composition and constant of reactions when combined with the appropriate thermodynamic data table.

2.2.1.2 Nernst Equation

An electrochemical cell in a spontaneous process, at constant temperature and pressure can produce maximum work given by

$$\Delta G = W_{e,max} \tag{2.19}$$

As this process improves with time by $d\xi$, the maximum non-expansion work is given as:

$$dW_e = \Delta G_r d\xi \tag{2.20}$$

An infinitesimal change, $-vFd\xi$ because of movement of a particle from anode to cathode does work equal to:

$$dW_e = -vFEd\xi \tag{2.21}$$

Equating (2.20) and (2.21) yields

$$\Delta G_r = -vFE \tag{2.22}$$

Equation (2.22) is useful because it creates a link between electrical measurements and thermodynamic properties.

From equation (2.16), we can easily decipher that there is a relationship between Gibbs energy and the reaction mixture, and if we divide through with $-vF$, we can obtain (2.23) as:

$$E = -\frac{\Delta G_r^0}{vF} - \frac{RT}{vF}\ln(Q) \tag{2.23}$$

If we use E^0 to represent first term on the right for simplification, we get:

$$E^0 = -\frac{\Delta G_r^0}{vF} \tag{2.24}$$

Equation (2.24) is the standard cell potential (E^0). Inserting E^0 into equation (2.23) gives the Nernst equation as follows:

$$E = E^0 - \frac{RT}{vF}\ln(Q) \tag{2.25}$$

Generally, molecules tend to move from a region of high concentration to that of lower concentration, i.e, downwards of their concentration gradient. To hinder this movement, an opposing force (electrical potential) has to be applied. If this is done successfully, there would be no net movement across the cell, and an equilibrum position would have been established. This process is what the Nernst equation entails. The electrical potential refers to the potential in mili-volts where there is no net movement of charged particles for a given concentration gradient. It allows us to decipher the cell potential under non-standard states.

2.2.1.3 Peukert's Equation

Several matrices affect the longevity and performance of a battery. For example, the behaviour of batteries when current is applied to it [7]. In general, current addition is inversely proportional to voltage and capacity decrease. This relation is captured by the Peukert's equation [7].

$$I^n * t = C \tag{2.26}$$

Where: I = current (Amperes)
t = time (hours)
C = capacity rating
But C value is controlled by rate, so a correction of this deficit led to a modification of the Peukert's law [7]

$$t = \frac{H}{(\frac{IH}{C})^n} \tag{2.27}$$

Where H = Hours for rated capacity

2.3 Supercapacitors and Batteries

The advent of electrochemical energy has kick-started the consideration of supercapacitors and batteries as effective candidates to replace fossil fuel energy production/consumption. Batteries store chemical energy and deliver it later as electricity. They can either be primary cells, secondary cells or fuel cells [6, 17].

Volta initially used the word 'battery' to describe a set-up consisting of stacked metals in contact with a wet cloth as electrolyte. Recently, the same word now describes a single electrochemical

cell [28]. Varied materials make up a battery; these are 3 electrodes: the cathode, anode and electrolyte, current collectors, separators, etc. A schematic of a modern battery with its usual components is shown in figure 2.4. .

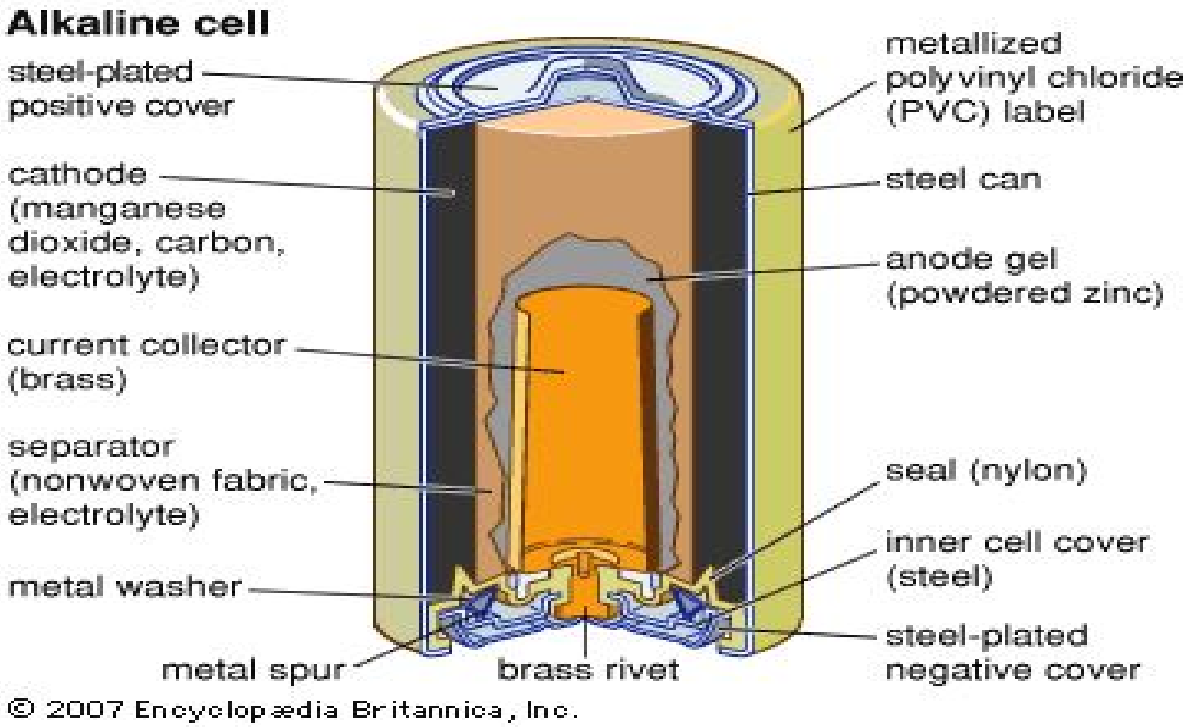

FIGURE 2.4: Schematic of a modern battery [4]

Batteries consist of a positive anode and a negative cathode in contact with an electrolyte. Electrical energy is generated from stored chemical energy via REDOX reactions at the electrodes. Both the anode and cathode are linked to each other via an electrical conductor conceiving an electric current; the electrolyte on the other hand is responsible for conduction of positive ions [4]. The movement route of electrons from one electrode to the other is outside the circuit, and a system balance is achieved by the transit of ions across the electrolyte [4, 28].

The specific materials adopted as choice for electrode materials determine the characteristics and performance of the battery [4, 28]. These materials are selected such that the anode contributes the electrons, while the cathode just receives it. A material either contributes or receives electrons based on its standard electrode potential, and the variation in value between the electrode potentials of both electrodes gives the gross voltage of the cell [4]. A chemical reaction occurs between the anode and the electrolyte. This reaction leads to loss of electrons, and positive ions called cations are produced as a result. This reaction is called oxidation. On the other hand, the electrons and cations are involved in a similar but opposite reaction at the cathode. This reaction leads to the formation of cations, and is known as a reduction reaction. The summation of these processes is termed Oxidation-reduction/REDOX reaction [28]. Figure 2.5 shows these reactions in the charge and discharge states.

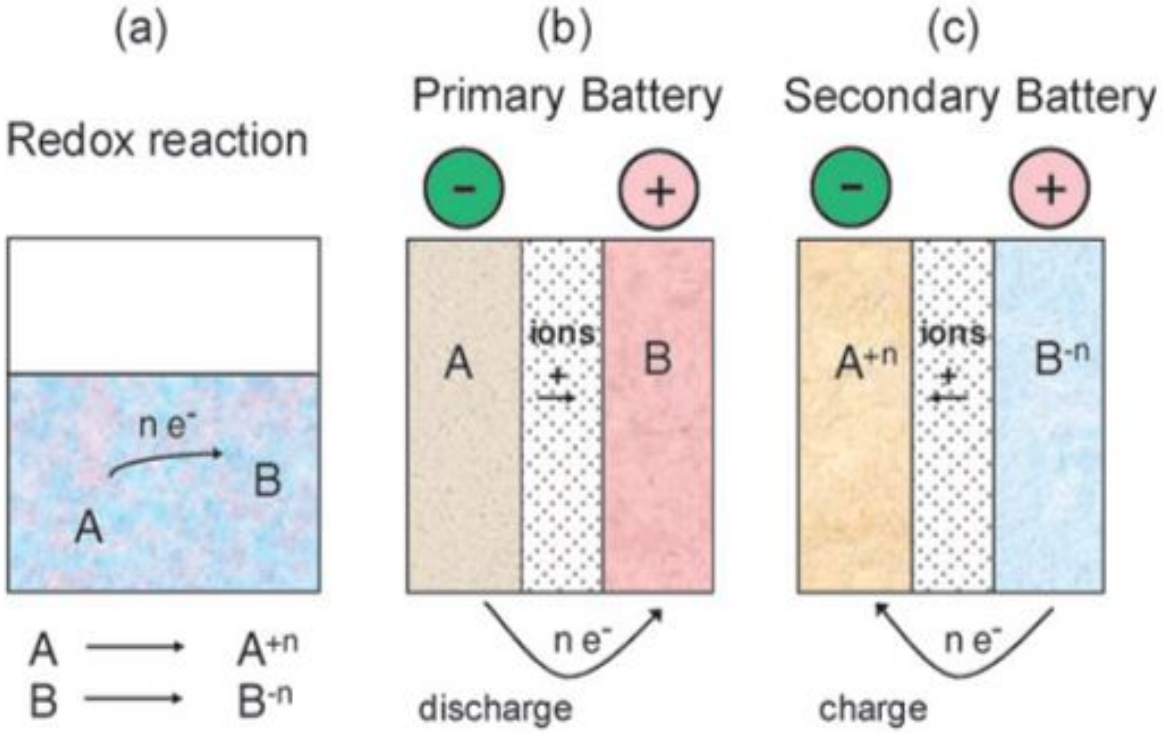

FIGURE 2.5: Diagrams showing (a) Oxidation-reduction reaction (b) Discharging primary battery (c) Charging secondary battery

.

These reactions go on until the materials are either used-up or corroded, during which the batteries would be disposed. A lot of batteries are disposed as waste every year because of this. Typical REDOX reactions for a non-rechargeable dry Leclanche cell battery is shown in Table 2.1 below:

TABLE 2.1: Typical Properties of a Simple Primary Cell [17]

Property	Primary Cell
Anode	Zinc
Cathode	Graphite
Electrolyte	Zinc
Oxidation Reaction	$Zn(s) \longrightarrow Zn^{2+}(aq) + 2e^-$
Reduction Reaction	$2MnO_2 + H_2O(l) + 2e^- \longrightarrow Mn_2O_3(s) + 2OH^-(s)$
Overall Cell Reaction	$NH_4^+(aq) + OH^-(aq) \longrightarrow NH_3(g) + H_2O(s)$
Electrolyte Medium	Acidic

Table 2.1 describes a regular voltaic cell consisting of a zinc anode, carbon cathode and a paste-mix of manganese (IV) oxide, zinc chloride, ammonium chloride and soot. The Leclanche cell's major setbacks are formation of NH_3 on the electrodes and acidic dissolution of zinc over time [17]. Figure 2.6 shows a section of a Leclanche cell with the necessary components.

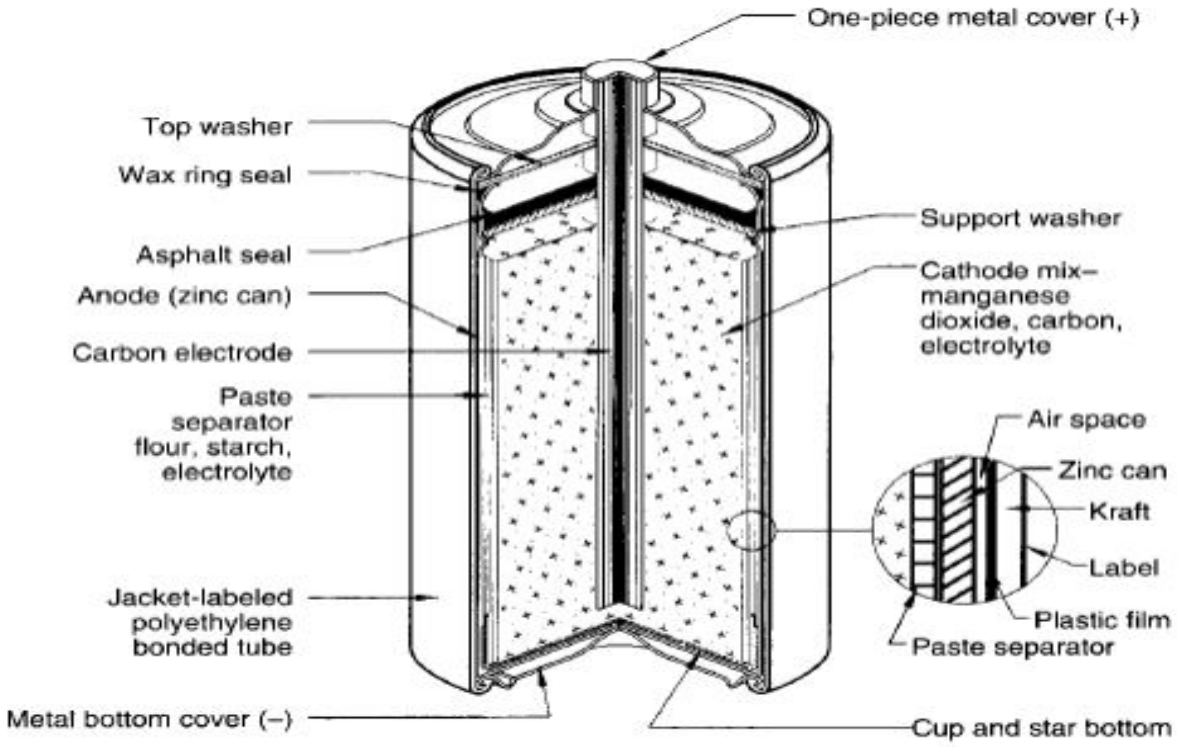

FIGURE 2.6: Simple diagram of a Leclanche cell [5]

.

common name	nominal voltage	anode	cathode	electrolyte
primary				
Leclanché (carbon–zinc)	1.5	zinc foil	MnO_2 (natural)	aq $ZnCl_2$–NH_4Cl
zinc chloride (carbon–zinc)	1.5	zinc foil	electrolytic MnO_2	aq $ZnCl_2$
alkaline	1.5	zinc powder	electrolytic MnO_2	aq KOH
zinc–air	1.2	zinc powder	carbon (air)	aq KOH
silver–zinc	1.6	zinc powder	Ag_2O	aq KOH
lithium–manganese dioxide	3.0	lithium foil	treated MnO_2	$LiCF_3SO_3$ or $LiClO_4$[a]
lithium–carbon monofluoride	3.0	lithium foil	CFx	$LiCF_3SO_3$ or $LiClO_4$[a]
lithium–iron sulfide	1.6	lithium foil	FeS_2	$LiCF_3SO_3$ and/or $LiClO_4$[a]
rechargeable				
lead acid	2.0	lead	PbO_2	aq H_2SO_4
nickel–cadmium	1.2	cadmium	NiOOH	aq KOH
nickel–metal hydride	1.2	MH	NiOOH	aq KOH
lithium ion	4.0	Li(C)	$LiCoO_2$	$LiPF_6$ in nonaqueous solvents[a]
specialty				
nickel–hydrogen	1.2	H_2 (Pt)	NiOOH	aq KOH
lithium–iodine	2.7	Li	I_2	LiI
lithium–silver–vanadium oxide	3.2	Li	$Ag_2V_4O_{11}$	LiAsF[a]
lithium–sulfur dioxide	2.8	Li	SO_2 (C)	SO_2–LiBr
lithium–thionyl chloride	3.6	Li	$SOCl_2$ (C)	$SOCl_2$–$LiAlCl_4$
lithium–iron sulfide (thermal)	1.6	Li	FeS_2	LiCl–LiBr–LiF
magnesium–silver chloride	1.6	Mg	AgCl	seawater

[a] In nonaqueous solvents. Exact composition depends on the manufacturer, usually propylene carbonate–dimethyl ether for primary lithium batteries and ethylene carbonate with linear organic carbonates such as dimethyl carbonate, diethyl carbonate, and ethylmethyl carbonate for lithium ion cells.

FIGURE 2.7: Different combinations for commercial battery systems, Showing primary, secondary, and specialty batteries [6]

.

If these chemical reactions can be re-initiated every time by the application of external current, these batteries can be recharged. Rechargeable batteries are also known as secondary batteries. The best batteries are made based on the choice of materials for the respective electrodes [28]. Different combinations of materials have been adopted to obtain the best results for secondary batteries [22, 28]. Some of which are displayed in Figure 2.7. The rating of these combined materials is based on the amount of energy storage capability, voltage, safety, cost, etc [28]

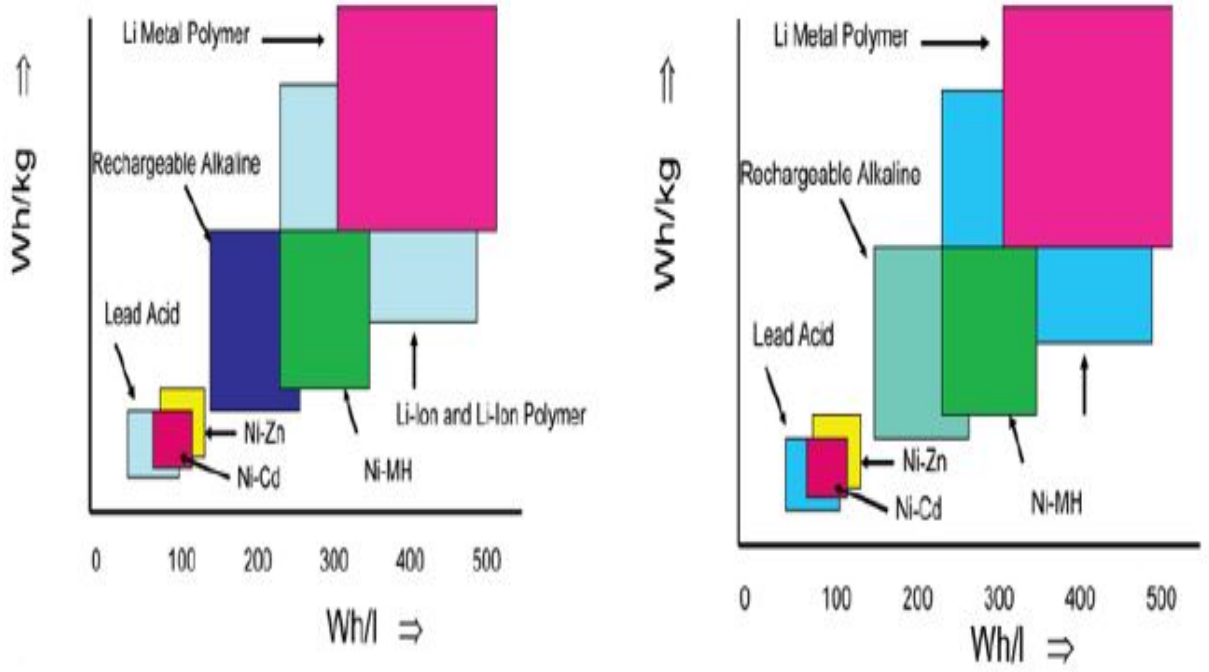

FIGURE 2.8: Energy storage capability of some Primary battery systems (left) and Secondary battery systems (right) [6]

.

Based on Figure 2.8, it can be observed that lithium compounds exhibit the best performance. This amongst other factors have been attributed to the location of lithium on the periodic table, its ease of ionization, and great electro positivity. Also, lithium being the lightest metal and third smallest element can contain a positive charge in a very little region [4, 20].

The lithium ion battery is always synthesised in such a way as to have the lithium ion as cation, and carbon as anode. The electrolyte is usually a synergy of various lithium salts[21]. The nominal voltage of these lithium systems ranges from 1.6V to 3.6V [6].

Even though lithium batteries have exhibited high energy density compared to other electrochemical counterparts, they are well below the energy density of other energy storage methods like fuel and food. This is because these sources store energy in chemical bonds as opposed to storage during REDOX reaction in batteries [6]. Generally, secondary cells convert stored chemical energy into electrical energy by a reversible chemical reaction. They are thus referred to as rechargeable cells [17, 18].

TABLE 2.2: Typical Properties of a Simple Secondary Cell [18]

Property	Primary Cell
Anode	Lead Oxide
Cathode	Metallic Lead
Electrolyte	Sulphuric acid
Oxidation Reaction	$PbSO_4 + 2OH^- \longrightarrow PbO_2 + H_2SO_4 + 2e^-$
Reduction Reaction	$PbSO_4 + 2H^+ + 2e^- \longrightarrow Pb + H_2SO_4$
Overall Cell Reaction	$2PbSO_4 + 2H_2O \longrightarrow PbO_2 + 2H_2SO_4 + Pb$
Electrolyte Medium	Acidic

Table 2.2 shows the typical properties of a lead acid accumulator secondary cell. The Anode is lead oxide, cathode is metallic lead, and the electrolyte is sulphuric acid. The charging process would form PbO_2 at the anode while metallic lead would be liberated at the cathode. The maximum cell voltage is about 30% higher than that of the Dry Leclanche cell.

Secondary cells typically have lesser storage capacity than their primary counterparts. The construction of secondary cells often involves a trade-off between reaction reversibility and longevity as against storage capacity. In batteries, the electrodes serve as a means of conveying charges, and they partake in the REDOX reaction. Also, the energy storage and conversion space is same as opposed to fuel cells where energy storage and conversion are separately cited. Lead batteries can be employed in diverse scenarios, from heavy equipment to energy storage for UPS devices [6].

2.3.1 Recent Developments

Ever since the discovery of lithium ion batteries, the electrochemical space has enjoyed unrivalled progressive attempts to consolidate upon the efficiency of this technology. A respectable number of erudite scholars have come up with anode enhancement proposals, and suggestions to ameliorate the safety and power density challenges faced by lithium batteries [19]. The anode used for lithium ion batteries is typically graphite, while the positive electrode is usually an oxide of lithium, and the electrolyte, a lithium salt with organic solvent.

Different authors have researched a lot on material synthesis for lithium ion battery cathode [38], anode [19, 20, 22, 39–41], using nanomaterials [21, 42, 43], and composites [44–49].

Tian [19] synthesized layered Sodium titanate nanoparticles using hydrothermal and solid-state sintering procedures which lasted for 2-24 hours. This product had a hierarchical structure

which is assumed responsible for the exhibited electrochemical and longevity performance of the battery. In another related scenario, the same author in collaboration with other scholars produced TiO_2 to upgrade the specific and rate capacities of lithium ion batteries. He discovered that a proper hierarchical structure could enhance the application and performance of spinel lithium titanate as anode material for lithium ion batteries [50].

Composite materials were also synthesized by some other authors [20, 21]. Wang [20] applied heat treatment and adsorption to produce macropore acrylic type resins. He was able to achieve an in-situ formed Co_3O_4/C which exhibited a homogenous dispersion within carbon network. The resulting sample exhibited high capacity performance, better than that of its individual constituents. CheVVnpei also synthesized composite oxide nanotubes $Co_3O_4-CeO_4$ using an electrospinning technique with an annealing procedure. The resulting sample he made was utilized both for carbon (II) oxide oxidation and as anode for lithium ion batteries. The rate capability was commendable for the latter application [21]. Xiaofeng synthesized a 3D porous $LiFePO_4$ with nitrogen doped carbon tubes using a freeze-drying technique. The structure of the prepared sample makes for increased conductivity and high performance ratings [43]. Hongyan prepared Li_2MoO_3 for use as anode in Lithium ion batteries. This was done using a ball milling and thermal reduction technique. The authors went further to decipher the reaction mechanism for this process, and checked the electrochemical performance of the prepared material [22]. Kobayashi prepared Li_2O doped with copper by utilizing reactions between Li_2O and CuO. The produced sample, as cathode material exhibited average charge capacity, and the author could detect a relationship between specific capacity and oxygen 2P and 3d orbital of transition metals [38]. Jaiswal made an analysis of lithium ion battery based-solution for off-grid electricity. He assayed the merits of lithium ion battery as potential candidates to replace lead-acid battery in Small renewable energy solutions such as solar home lighting system (SHLS) applications [51].

TABLE 2.3: Properties of Anode Materials [19–22]

Anode Material	Capacity ($mAhg^{-1}$)	Cycles	Current Density (mAg^{-1})	Energy Density	Columbic Efficiency %
$Na_2Ti_2O_5$	164.3	5000	1000		$\geq 99\%$
$Li_2Ti_5O_{12}$	110.8	5000			
Co_3O_4/C	928		200		
$Co_3O_4 - CeO_2$	1286.3	180	0.1		
Li_2MoO_3	835		100	97.6	

2.3.2 Limitations of the Present Batteries

2.3.2.1 Safety Issue

A unique battery with optimal performance would depend greatly on its electrode innate characteristics, and its interface between electrode and electrolyte tells the cycle and longevity. The integrity of this interface determines the safety of this system [52]. The lithium metal and liquid electrolyte connection in extreme conditions (mostly during trickle charging) can create a short circuit in the system due to the formation of dendrites. This can lead to explosion hazards. The Samsung, Nokia and iPhone devices are some examples of gadgets that have been involved in this mishap [52, 53].

2.3.2.2 Cycle Life

The life cycle of a rechargeable battery refers to the number of charge/recharge routines before the battery drops in performance. Rao discussed that a replacement of the Lithium metal with an alloy of aluminium could close out the explosion issue. This worked but then the aluminium electrodes could only withstand a certain degree of operational volume change [54, 55]. These batteries therefore had a limited cycle life and voltage. This was a trade-off of voltage and cycle life against elimination of the dendrite formation [52, 54].

2.3.2.3 Energy and Power Density

Batteries of nowadays exhibit a high-energy density, but low power density. The Ragone plot Figure 2.9 displays the performance rating of diverse energy storage devices. It typically reveals downward curves. This means that, there is often a trade-off between power and energy [7]. Devices can only have very much of either power density or energy density.

In Figure 2.10, it is evident that an extra amount of acid is required to conduct ions in the charge and discharge states. Also, reflecting on the slight mass usage as opposed to the exigency of dormant constituents, one can decipher easily that the empirical value of specific energy is about one quarter of its theoretical approximation for secondary batteries [6].

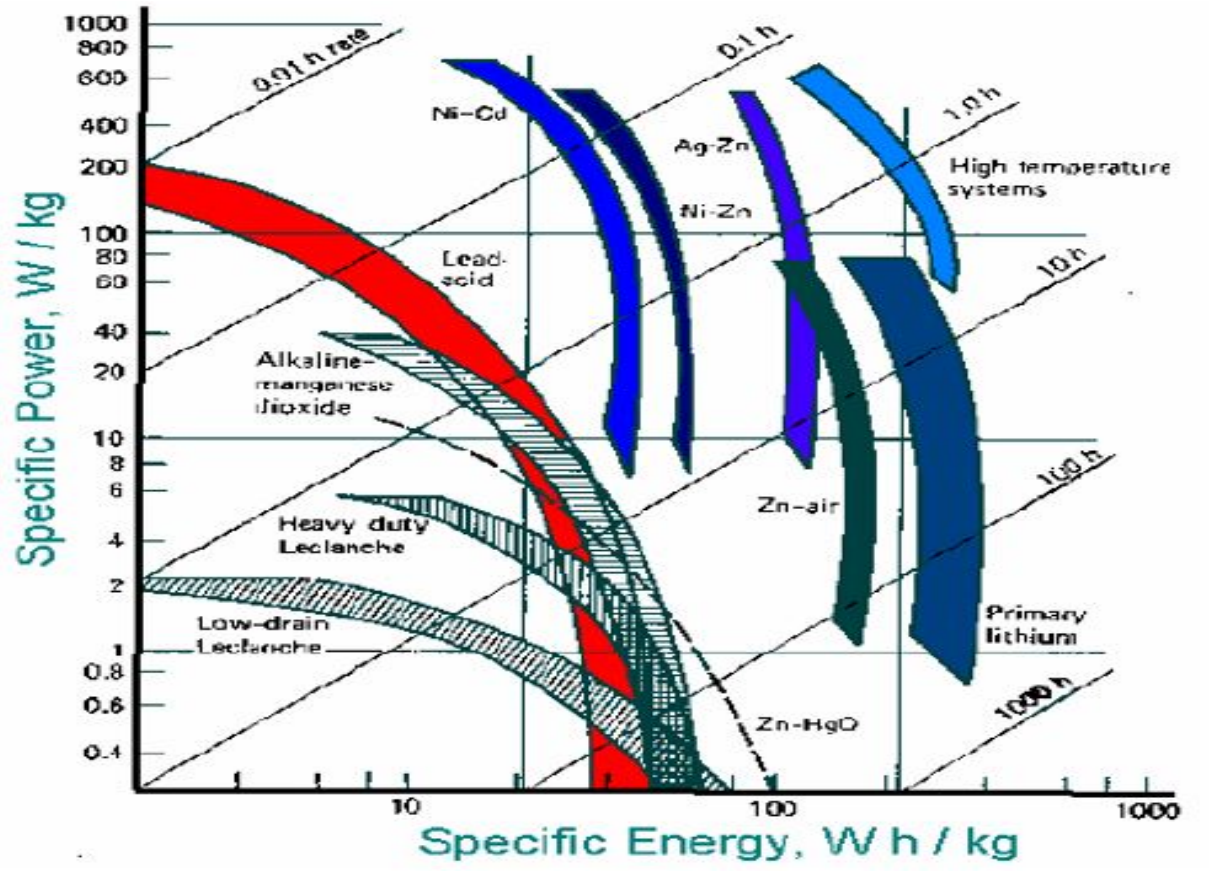

FIGURE 2.9: Ragone plot for some energy storing devices [7]

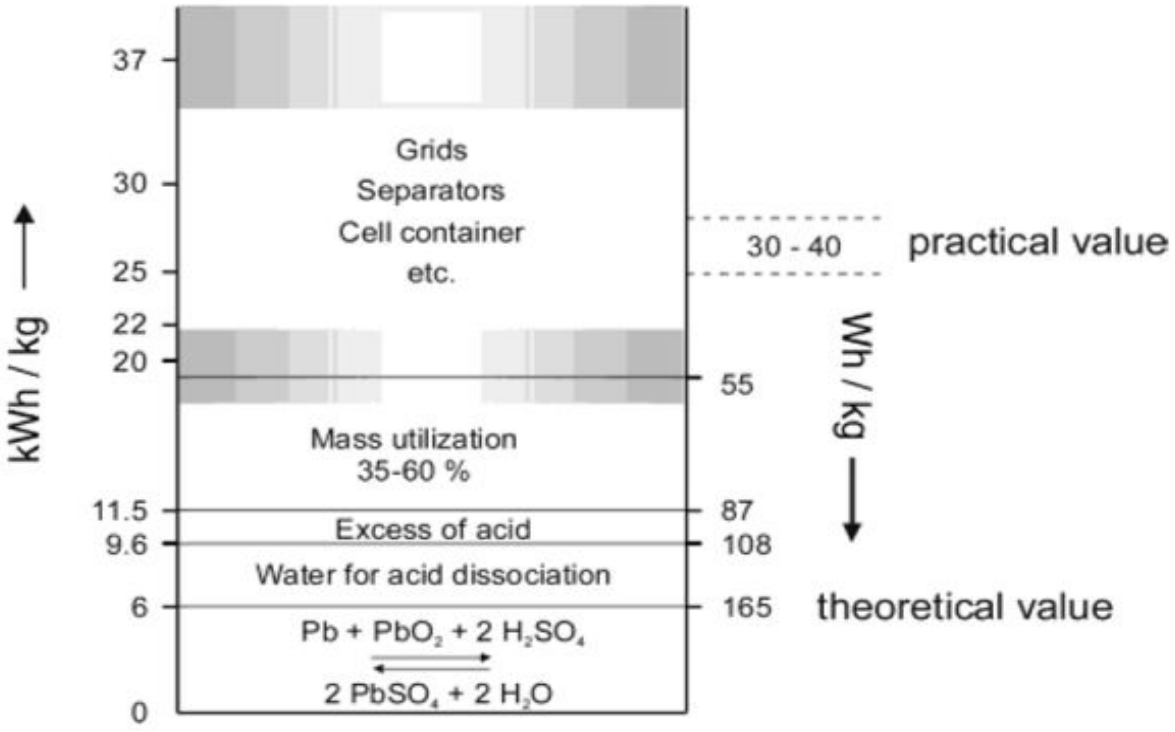

FIGURE 2.10: Component description of lead acid battery displaying the difference and source of difference between practical and theoretical energy density [6]

2.3.3 Supercapacitor

A second cliché of electrochemical storage devices is the supercapacitor. They stem from a branch of storage devices known as capacitors. A capacitor refers to a set-up of two conducting plates partitioned by an insulator material. An electric field is created between the plates when charged, and charge separation induces a voltage. Parallel plate capacitors, charge opposing plates set apart by a dielectric for voltage induction. Capacitors differ from batteries in terms of longevity, because they have their chemical reactions during operation, and also in mechanism of charge storage (they do this in a reversible physical process) [8, 56]. Figure 2.11 shows a parallel plate capactor with its electrodes and dielectric material.

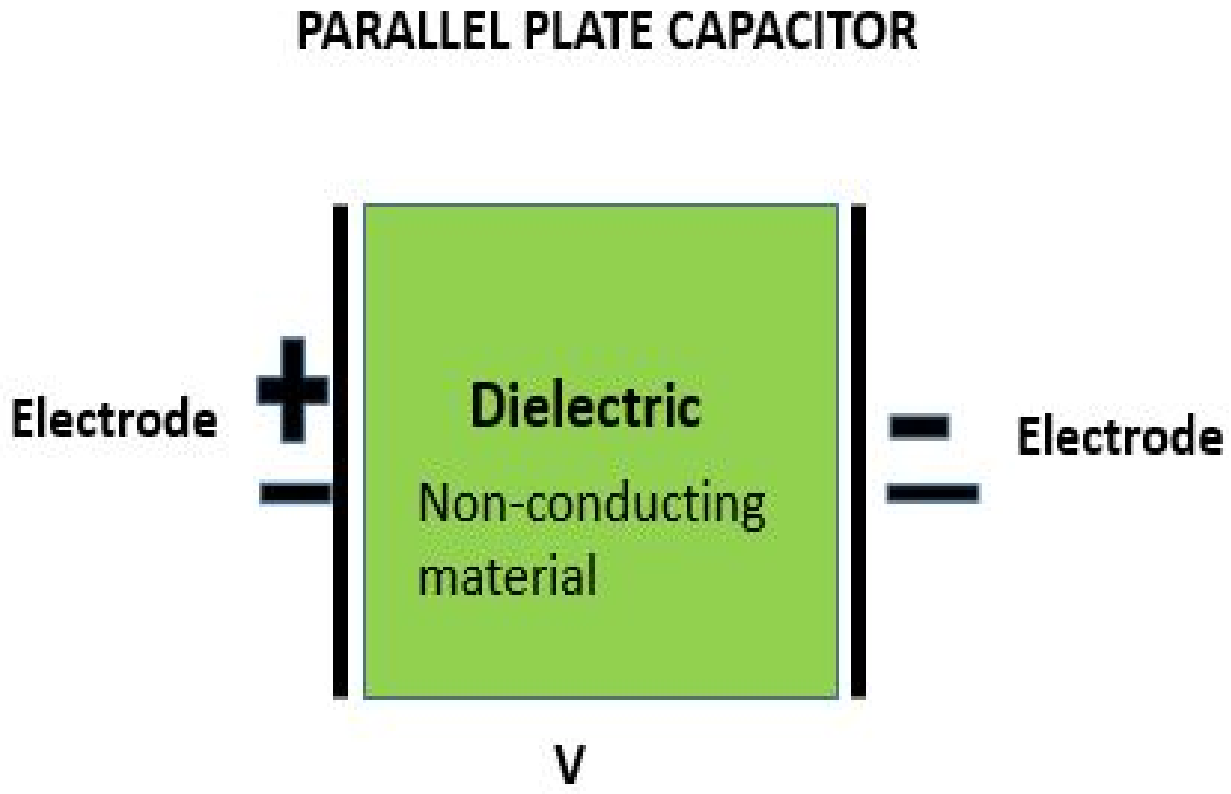

FIGURE 2.11: Parallel plate capacitor [8]

The capacitance of a capacitor measures the ability of a capacitor to store charge. The Farad is the unit of capacitance. This capacitance is dependent on several key factors, namely, the distance and area of the plates, and the permittivity of the dielectric material. This relationship can be expressed mathematically as:

$$C = \frac{\varepsilon_0 \varepsilon_r A}{d} \tag{2.28}$$

Where: ε_0 = Permittivity of free space; ε_r = Dielectric constant; A = Area of the plates; d = Separation distance.

Equation 2.28 demands that a reduction of the distance, or an increase of the permittivity of the material or more still, an increase of the area would increase the capacitance significantly. There has been attempts to reduce the distance, but there is a limit to the acceptable physical size. One way to do this, is to use an electrolyte.

Supercapacitors, also known as electrochemical capacitors are an advanced form of capacitors. They have an electrolyte between the plates instead of a dielectric material. The mechanism of operation also differs from that of batteries in that, the delivery of energy is not by REDOX reaction, but by the physical movement of ions. Figure 2.12 shows a simple schematic of a supercapacitor.

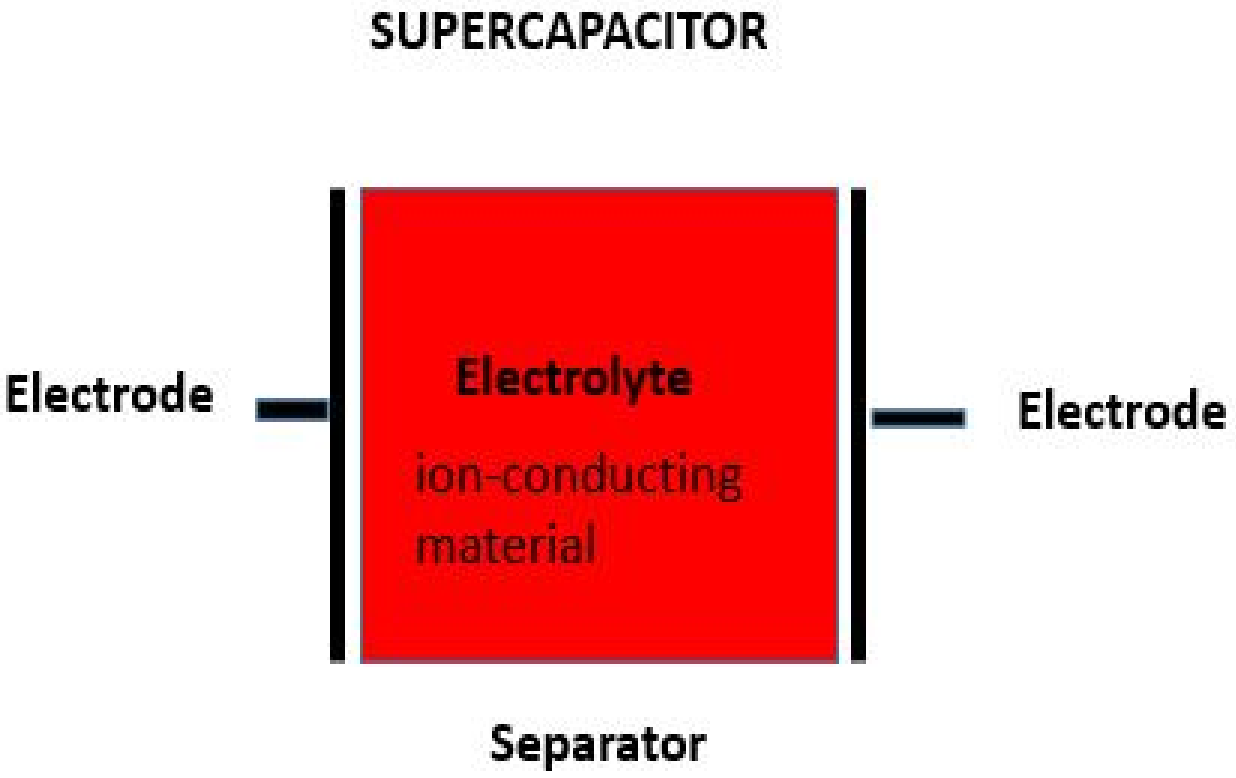

FIGURE 2.12: Simple supercapacitor schematic [8]

.

2.3.4 Capacitors Versus Supercapacitors

While the energy in inductors is stored in an electromagnetic field, a capacitor stores this energy in an electrostatic field. This occurs by taking out electrons from a metal plate, and placing them on the other (Figure 2.12). This separation of charge between plates creates a potential difference.

The storage of energy in supercapacitors can be achieved in either of two ways: Reversible faradic reactions (pseudocapacitors) or Electrical double layers. The material used as electrode

determines which storage technique is adopted [57]. Supercapacitors have carbon electrodes so they charge by the formation of electrical double layers (EDL). The double layer consists of two layers: The Helmholtz layer and the diffuse layer [8].

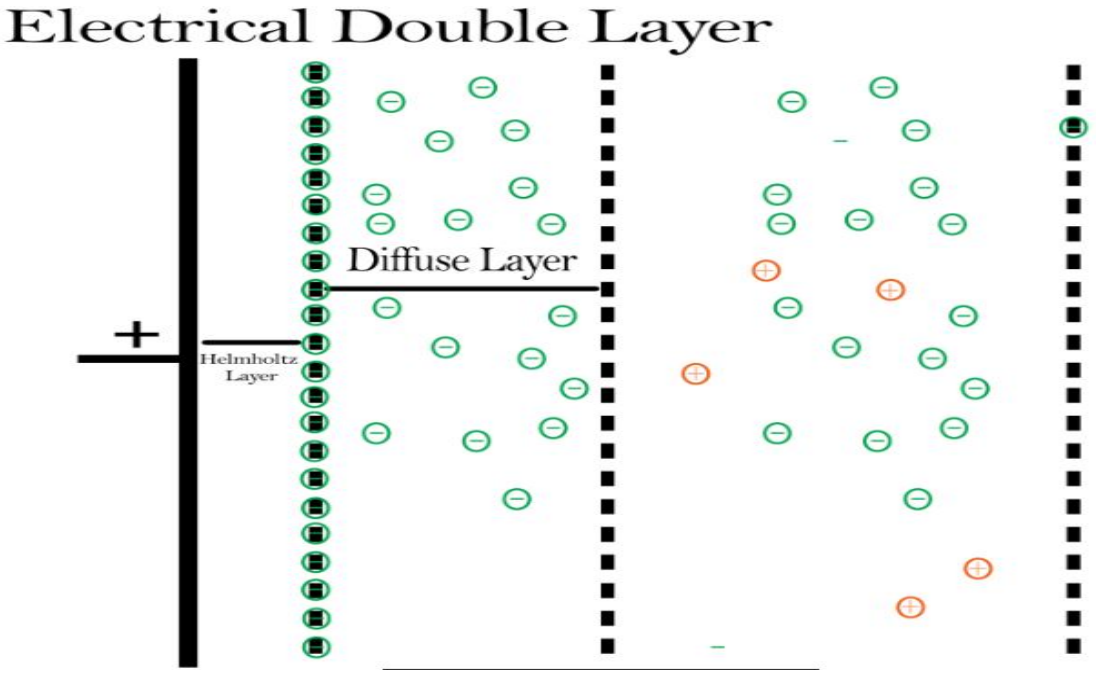

FIGURE 2.13: Supercapacitor showing the electrical double layers [8, 8]

.

The Helmholtz layer influences the capacitance, and consists of a dense ion layer and oppositely charged electrodes parted from each other by solvent molecules. The diffuse layer on the other hand refers to ions migrating into the Helmholtz layer boundary. These are all portrayed in Figure 2.13.

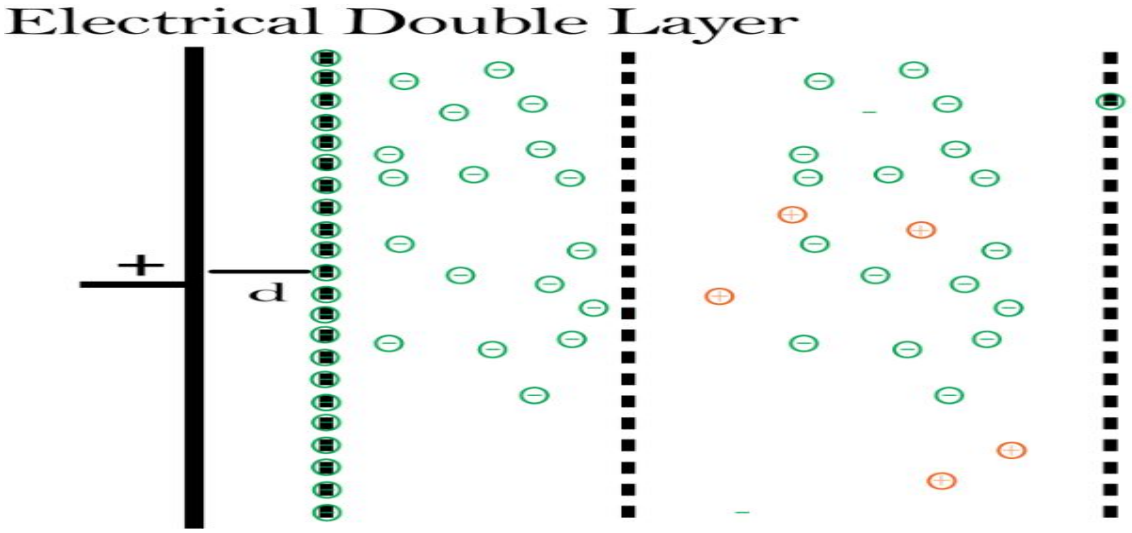

FIGURE 2.14: Supercapacitor showing 'd'[8]

.

The Helmholtz layer can be thought of as a parallel plate capacitor where d is the thickness of the solvent layer. This d (Figure 2.14) helps to explain why supercapacitor has higher capacitances than ordinary capacitors [8]. An equivalent circuit for supercapacitors can be represented as shown in Figure 2.15:

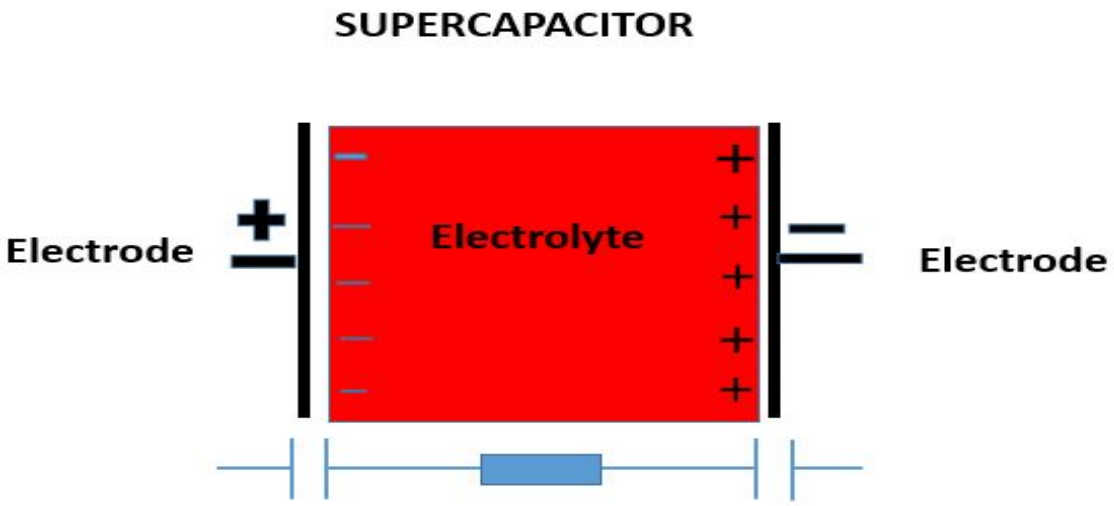

FIGURE 2.15: Equivalent circuit for a supercapacitor [8]

.

In Figure 2.15, we can observe two capacitors in series with a resistor. The capacitors represent the double layers, and it thus specifies the energy contained in the system. The resistors represent the internal resistance resulting from diffusion, and hence specifies the energy losses.

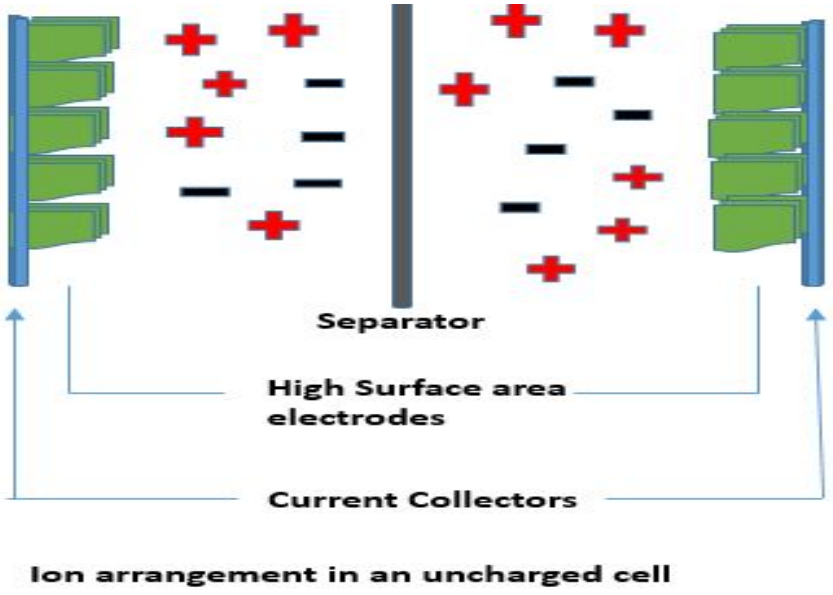

FIGURE 2.16: Ion arrangement in an uncharged cell

.

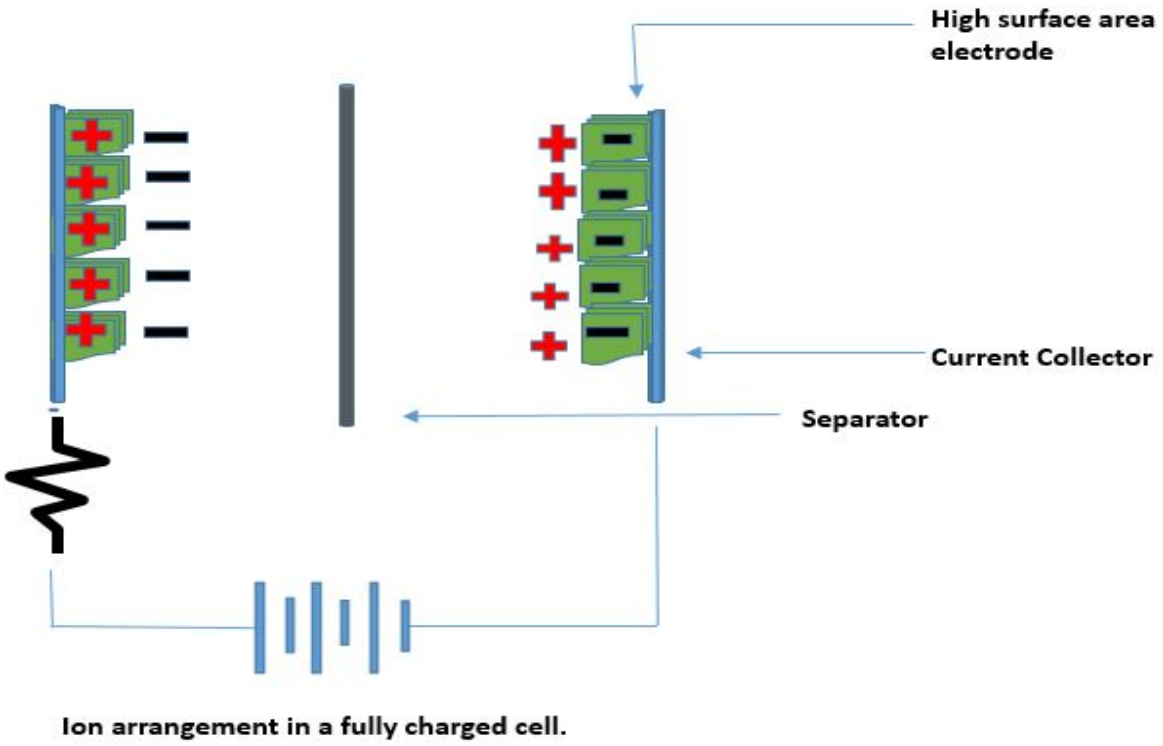

FIGURE 2.17: Ion arrangement in a fully charged cell

.

In an uncharged cell, the ions are in a dispersed state, as shown in Figure 2.16. During the charging process, they begin to move towards the respective corresponding oppositely charged electrode. After the charging process, the ions adopt a new orientation as shown in Figure 2.17.

Batteries typically have more energy density than supercapacitors. For example, a typical AA NiMh Battery can store up to 9000 Joules of energy. But a 500F, 2.7 Volts supercapacitor would store energy given by the relation:

$$Z = \frac{1}{2}CV^2 \tag{2.29}$$

Where Z = Energy stored by supercapacitor; C = capacitance of the supercapacitor; V = Voltage of the supercapacitor.

If we input the parameters into Equation (2.29), we find out that the supercapacitor can only store up to 1800 Joules of energy.

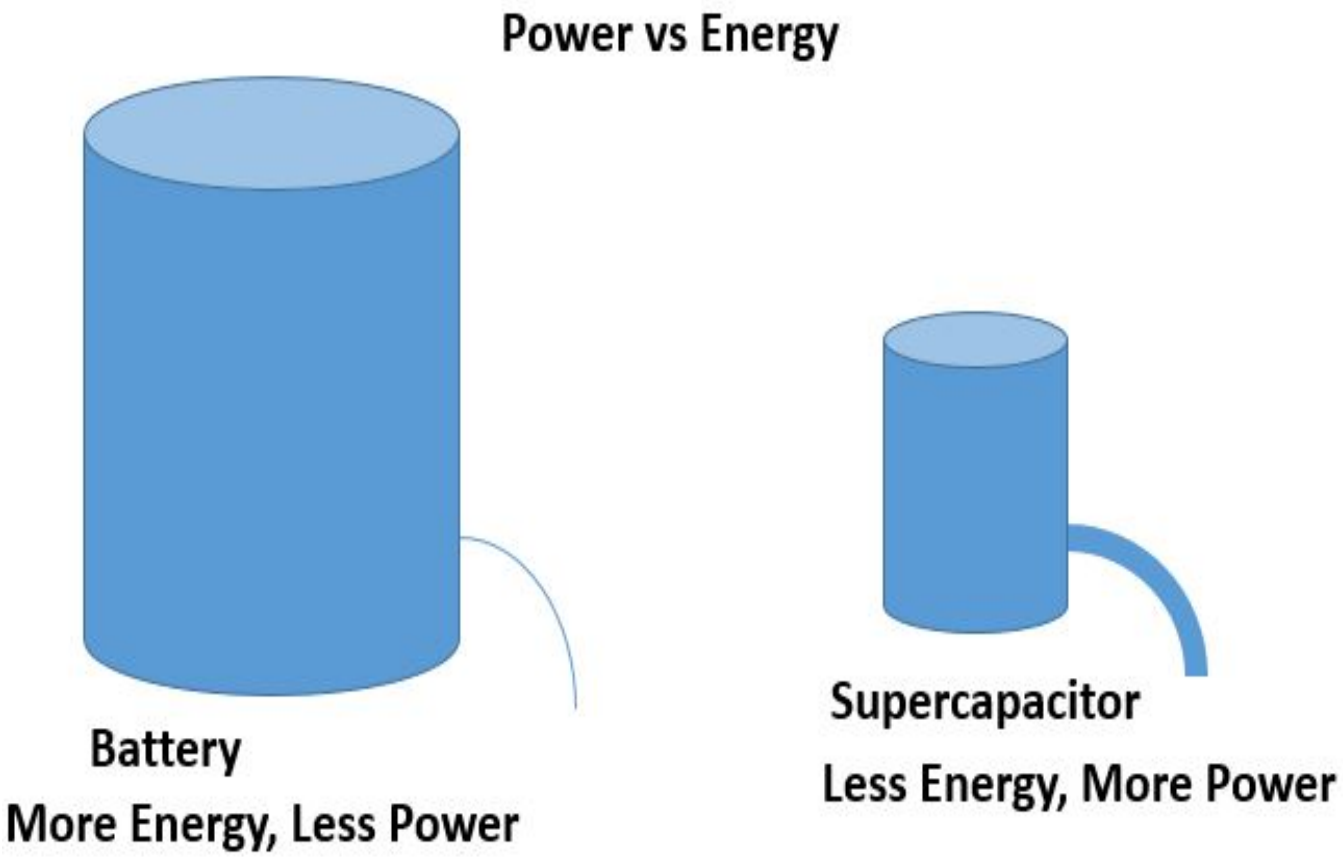

FIGURE 2.18: Simplified energy and power density differences between batteries and supercapacitors

.

Figure 2.18 shows that batteries can have higher energy density, but lower power density. Supercapacitors typically have a high power density, but low energy density.

TABLE 2.4: Battery and Supercapacitor Properties Comparison

Property	Battery	Supercapacitor
Energy Density	High	Low
Power Density	Low	High
Energy Generation	Redox Reaction	Movement of Ions
Cycle Life	Low	High
Self Discharge	Low	High

Table 2.4 shows the typical differences between batteries and supercapacitors.

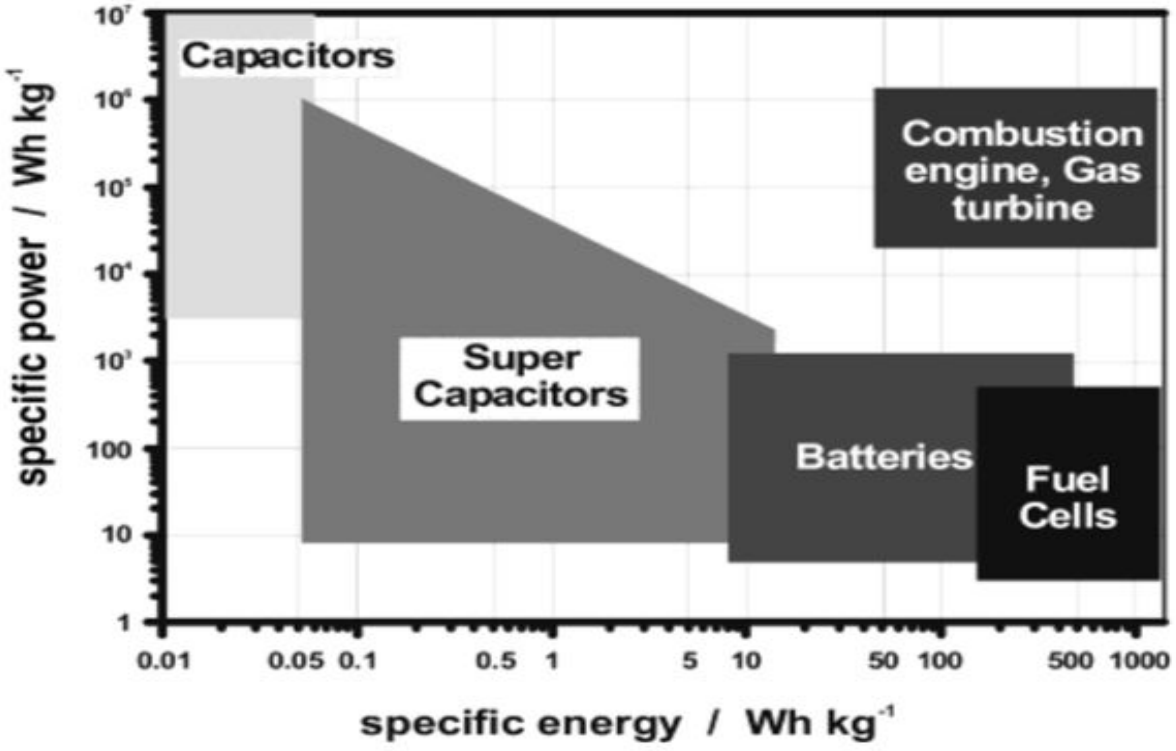

FIGURE 2.19: Simplified Ragone plot of the energy storage domains for the various electrochemical energy conversion systems compared to an internal combustion engine and turbines and conventional capacitors [6]

The Ragone plot on Figure 2.19 shows that supercapacitors have the least specific energy compared to other electrochemical energy conversion systems. However, they have significantly higher specific power, greater than other electrochemical conversion systems, only comparable to combustion engines and gas turbines.

2.3.5 Recent Developments in Supercapacitor Technology

The ultimate performance of supercapacitors richly depends on the materials used in its synthesis [56]. Because of this, a lot of authors have invested a lot of energy into the search for perfect materials. While some group of authors have used two-dimensional materials [57], others used three-dimensional materials [58–61], and some still used nanomaterials [62–70].

Liu discussed the rising of two-dimensional (2D) supercapacitor electrode materials, for example graphene, carbides and dichalcogenides. These materials had low weight and exhibited good mechanical flexibility but did not perform satisfactorily as electrodes. To mitigate this issue, he suggested reduction of packing density, synthesizing porous microstructures, and the study of interfacial reactions [57].

Yao reviewed three-dimensional (3D) porous graphene structures made from two-dimensional (2D) graphene sheets. He argued that this could better utilize the fine properties of graphene

[58]. Malik synthesized a three-dimensional (3D) polyaniline/carbon nanotube composite as electrode for supercapacitors. After testing, the array of CNT exhibited high conductivity and superior mechanical properties [59]. Dongdong prepared macropore-rich activated carbon assembled by carbon nanoparticles. He used a phenolic resin (PR) precursor for this purpose, and identified a hierarchical structure as responsible for the superior specific capacitance and capacitance retention [71].

Li incorporated ultra-fine CuO nanoparticles into a three-dimensional graphene network nanostructure. This was carried out in a bid to extend the energy density of graphene [63]. Luo aimed to upgrade the electrochemical properties of Co_3O_4 for supercapacitors. This led him to synthesize hierarchical Co_3O_4@$ZnWO_4$ core shell nanostructures on nickel foam [67].

Gopalsamy synthesized NS-GNR by thermal annealing. This compound was employed as electrode for supercapacitor, and exhibited high performance due to a porous structure and multiple active sites [68]. Deng prepared carbon nanotubes/holey graphene hybrid film as binder-free electrode for supercapacitors. He investigated the properties in a tri-electrode system using an acidic medium [70].

2.3.5.1 Activated Carbon

Activated carbon refers to carbonaceous materials that typically have large surface areas per unit volume. They are also composed of multiple diminutive pores through which they can adsorb materials. Activation carbon as the name implies is prepared primarily from carbon. This carbon can be obtained from diverse materials with high carbon composition such as plants, minerals, animals and some chemicals [26–28].

The usage of activated carbon dates to 1550BC in Egypt. However, the China record states that a heavy form of charcoal was employed in a female tomb [28]. Industrial production commenced from 1900-1901. It was thereby employed in World war I to make gas masks. China also kick-started the study of producing activated carbon, and its development [28].

Activated carbon is usually employed in supercapacitors because:

- High and easily adjustable surface area
- Exceptional electronic conductivity
- Chemical stability
- Low cost and availability

Characterization of Activated Carbons is done based on its activity and physical properties. Table 2.5 shows these properties.

TABLE 2.5: Properties of Activated Carbon [23, 24]

Anode Material	Capacity
Micropores < 10 nm	Iodine Number
Mesopores 10 to 100 nm	Surface Area
Macropores > 100 nm	Product density
	Ash Level
	Mesh Size
	Abrasion Resistance

- Granular Activated Carbon: Uneven in nature, created by grinding and sieving. Size ranges from 0.2mm to 5mm.
- Powdered Activated Carbon: Powdery in nature as the name implies; size range from 0.5 nm to 15 nm.
- Extruded Carbon: Cylindrical in nature, size range from 1mm to 5mm.

2.3.5.2 Preparation of Activated Carbon

Activated carbon can be classified according to raw materials/precursor into plants, animals, chemicals and minerals. Priority of choice is given based on cost, availability and purity [9, 72]. A lot of authors have worked on synthesizing activated carbon from these 4 categories. For Instance, there has been synthesis of activated carbon from plant materials such as gulf weed [73], waste tea [74], coffee shell [75], oil palm [76], wood [77, 78], corn cob [79], Rice husk [80], biomass [81, 82], and cellulose [83, 84]; animal materials such as cat tail[85], fish grill[86]; Chemicals such as ammonium polyphosphate [87], 1-ethyl-3-methylimidazolium tetrafluoroborate [88] and minerals [89].

The production of activated carbon can be achieved by the following processes:

1. PHYSICAL ACTIVATION: This is usually carried out by one or aggregating the following processes:
   - Carbonization
     The Carbonization stage involves thermal decomposition to remove all non-carbon material traces from the precursor. During carbonization, the precursor is thermally treated to temperatures below 600 °C in the absence of air. If this process is done in an inert surrounding, it would be referred to as pyrolysis. The products of this

reaction include char, tars and gases (2.30). In the course of pyrolysis, an initial porosity can be observed on the char portion, and a rigid carbon skeleton is formed [9, 90, 91]. The equation for this reaction is:

$$C_nH_{X-1}O_y \longrightarrow \text{Char} + \text{Gases} + \text{Tars} \tag{2.30}$$

Typically, char contains 75-80% carbon, about 15-17% oxygen and $< 3\%$ hydrogen. Gases are mainly CO, CO_2 and H_2O, and tar has phenols and high weight hydrocarbons [91, 92]

- Oxidation/Activation: The precursor is subjected to partial and controlled gasification in oxidizing atmospheres (oxygen, carbon (iv) oxide or steam environment). The temperature condition ranges from 600 °C to 1200 °C [9, 72, 93]. Some advantages and disadvantages of physical activation are shown in 2.6.

TABLE 2.6: Advantages and Disadvantages of Physical Activation [9]

Advantages	Disadvantages
Doesn't require a washing step	Poor check on porosity
Non-corrosive process	Requires two steps
Less expensive	Higher activation temperatures (800 °C to 1000 °C)

2. CHEMICAL ACTIVATION: Chemical activation aims to create and enlarge the precursor's pore diameter. Here, both the carbonization and activation steps occur together It involves impregnation or physical mixing of precursor material with a chemical agent. This chemical agent can either be an acid H_3PO_4, base (NaOH, KOH) a salt $ZnCl_2$, or even carbonates (K_2CO_3, Na_2CO_3) [9, 72]. Some advantages and disadvantages of chemical activation are shown in Table 2.7.

TABLE 2.7: Advantages and Disadvantages of Chemical Activation [9]

Advantages	Disadvantages
Involves only one step	Requires washing step.
High surface area of produced activated carbon.	High-priced/Expensive process
Makes for better check on textural properties.	Sometimes require the use of corrosive chemicals
Lesser activation time and pyrolysis temperature	

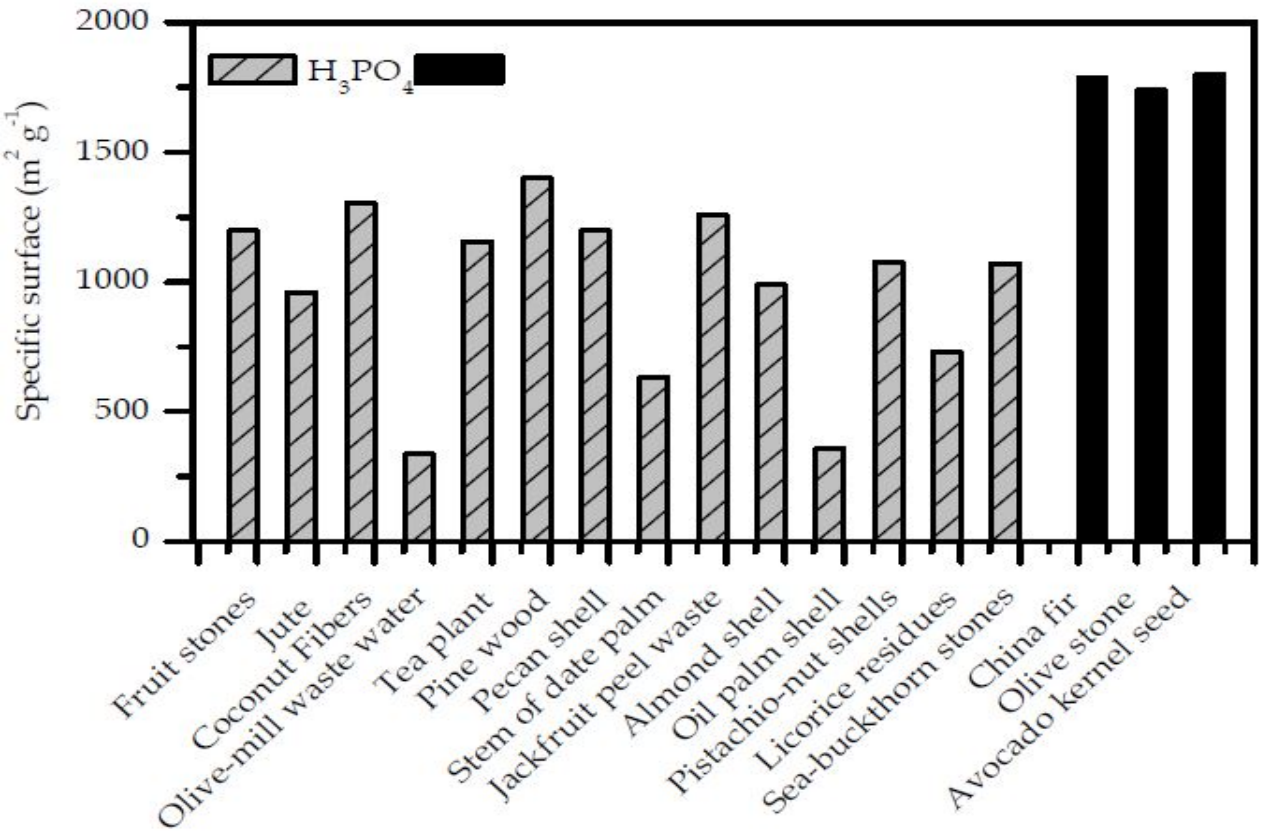

FIGURE 2.20: Surface areas of activated carbon produced from phosphoric acid [9]

.

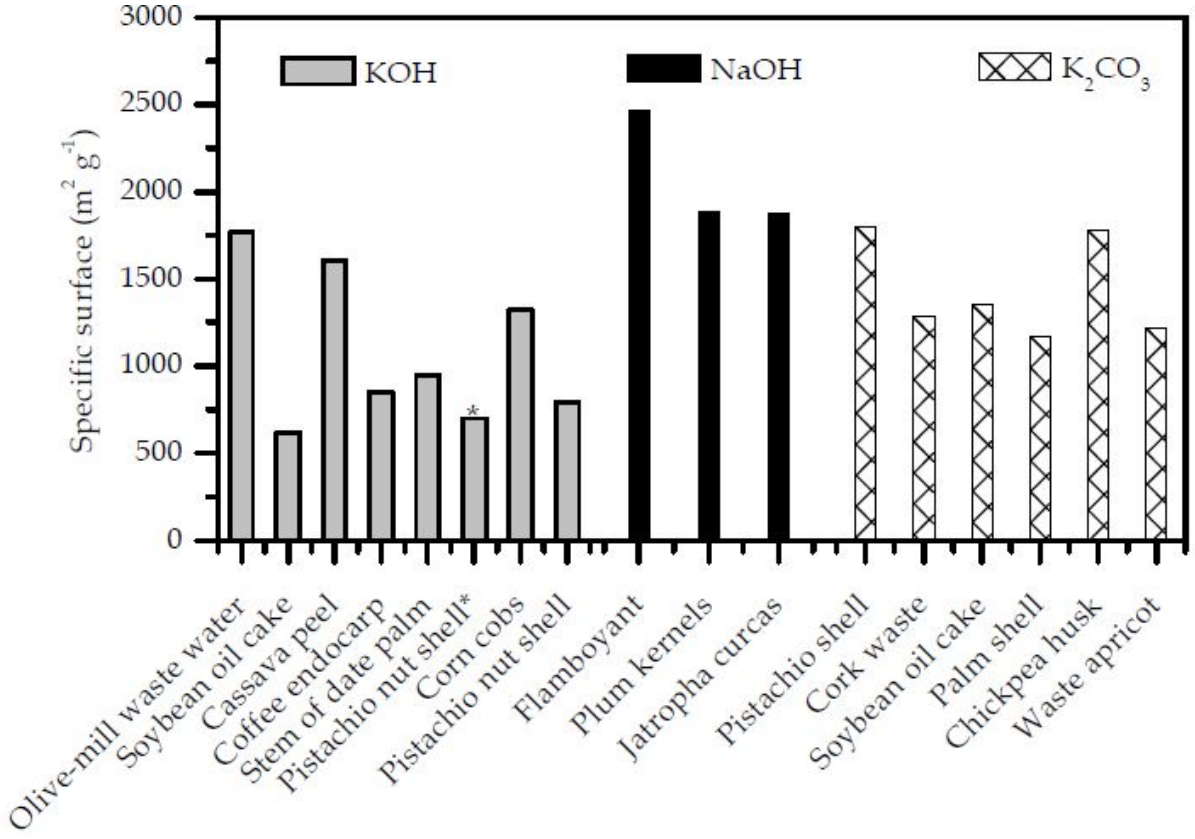

FIGURE 2.21: Surface areas of activated Carbon produced from potassium and sodium hydroxide and potassium carbonates [9]

.

Figures 2.20 and 2.21 shows the surface areas of activated carbon prepared from phosphoric acid and sodium and potassium carbonates respectively.

2.4 Material Characterization

Activated Carbon has successfully been used to remove contaminants from water [94, 95], metals [96], and other aqueous solution [97]. This process is possible based on the principle of adsorption.

Adsorption refers to the accumulation of molecules at the interface connecting two phases. It is different from absorption which entails that the molecules are drawn into the absorbing medium [25]. The differences between adsorption and absorption is displayed in Figure 2.22

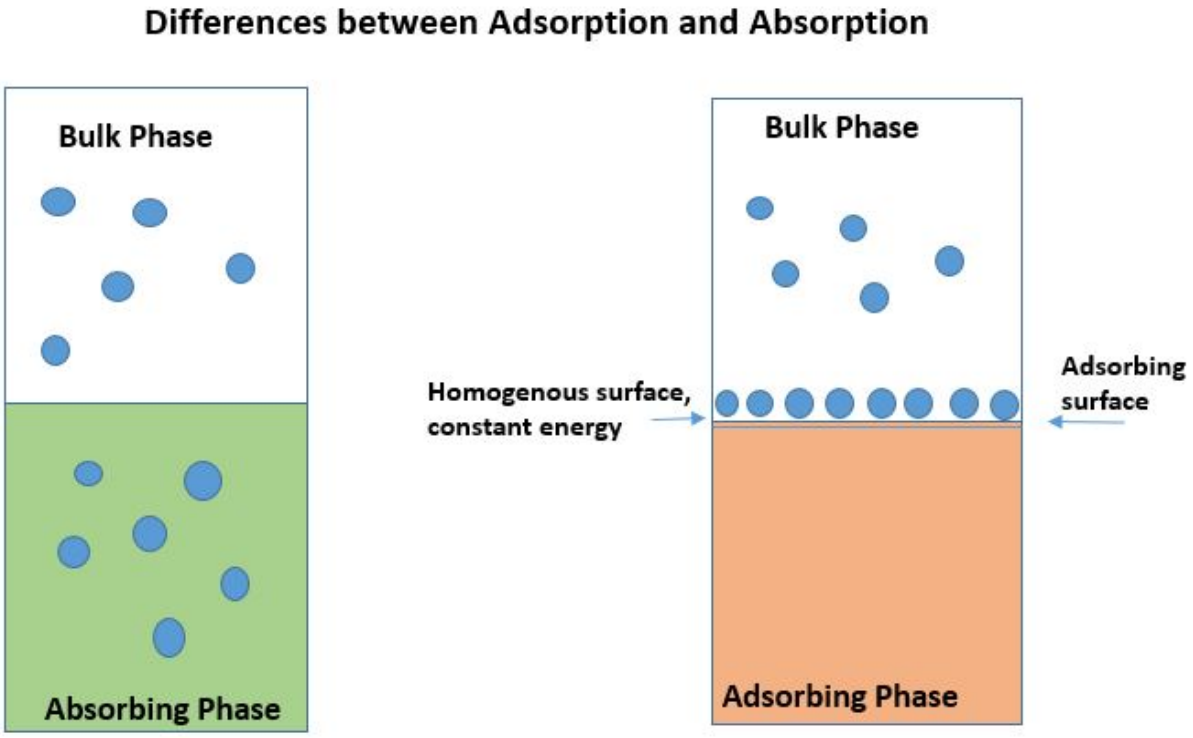

FIGURE 2.22: Difference between adsorption and absorption[10]

.

Some of the key qualities of activated carbon are its high surface area and pore volume [98]. Activated carbon has the ability to contain contaminants on its surface. A lot more contaminants can stick to this surface space because of its relatively large surface area.

In activated carbons, there also exists an internal surface area that contains forces which pulls in other molecules. These forces operate with same principle as gravitational forces. These molecules are then locked into the carbon pore framework by weak Van der Waal forces. The difference in pore concentration between the adsorbate (material being adsorbed) and activated carbon facilitates this process [23].

Molecules at interfaces have associated surface energy. They are able to attach themselves to these surfaces as a result of this surface energy. They can achieve this in two ways, these are: physical adsorption (physisorption) and chemical adsorption (chemisorption).

Physical adsorption (physisorption) occurs as a result of adsorbates being held to the surface of the adsorbent by weak intermolecular Van der Waal forces. These adsorbate molecules distribute themselves over the surface of the adsorbent [10].

For Chemical adsorption (Chemisorption), the attraction is orchestrated at the surface with the aid of chemical bonds. These bonds are tougher than the Van der Waal forces from physisorption. Some of these differences are outlined in Table 2.8.

TABLE 2.8: Differences between Physisorption and Chemisorption [25]

PHYSISORPTION	CHEMISORPTION
Molecules are free to move on surface	Molecules are fixed
Transfer of electrons doesn't exist, but adsorbate polarization is possible	Electron transfer exists, and creates bond formation
Monolayer or Multilayer	Monolayer
Only pronounced at low temperatures	Exists over a vast temperature range
Weak Van der Waal forces	Chemical bonds
Long range	Short range

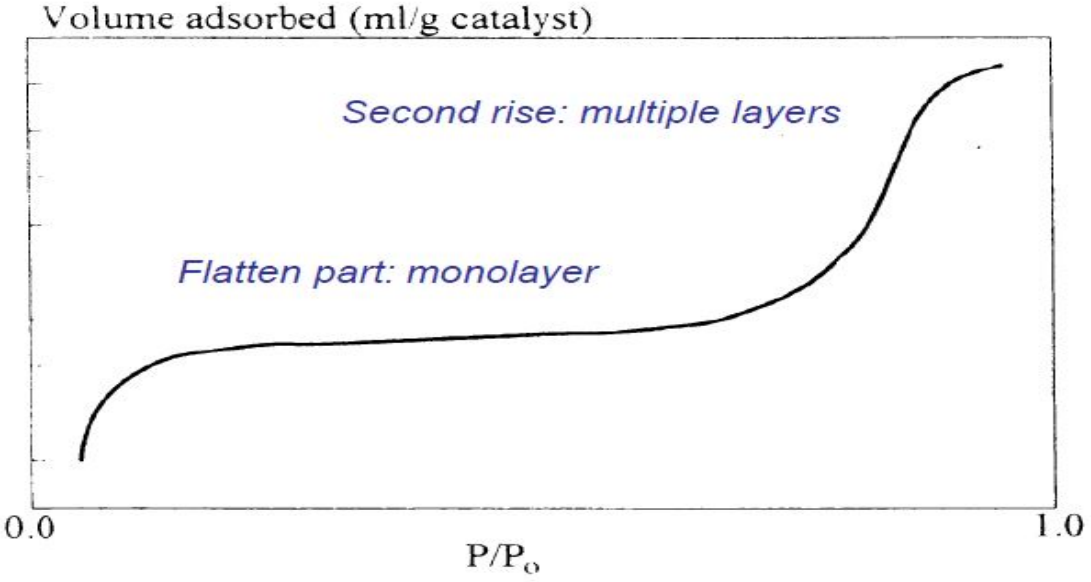

FIGURE 2.23: N_2 adsorption isotherm [11]

.

A nitrogen adsorption isotherm is displayed in 2.23. The following factors affect adsorption on surfaces.

- Temperature
- Pressure
- Surface area
- Activation of solid adsorbent
- Presence of other solutes
- pH

- Adsorbate solubility

2.4.1 Adsorption Isotherms

If the adsorbate and adsorbent are connected to each other, after a period of time an equilibrum position would be created. Isotherms enable us to study this process[10, 25]

2.4.1.1 Types of Isotherms

- Type I: For microporous solids (< 2 nm) langmuir isotherm
- Type II: For multilayer adsorption on non-porous or macroporous solids (> 50nm)
- Type III: For weak adsorption on non-porous or macroporous Solids
- Type IV: For mesoporous solids with hysteresis loop
- Type V: Same as in IV but with weak adsorbate-adsorbent synergy
- Type VI: For non-porous solids with near-uniform surface

2.4.1.2 Isotherm Models

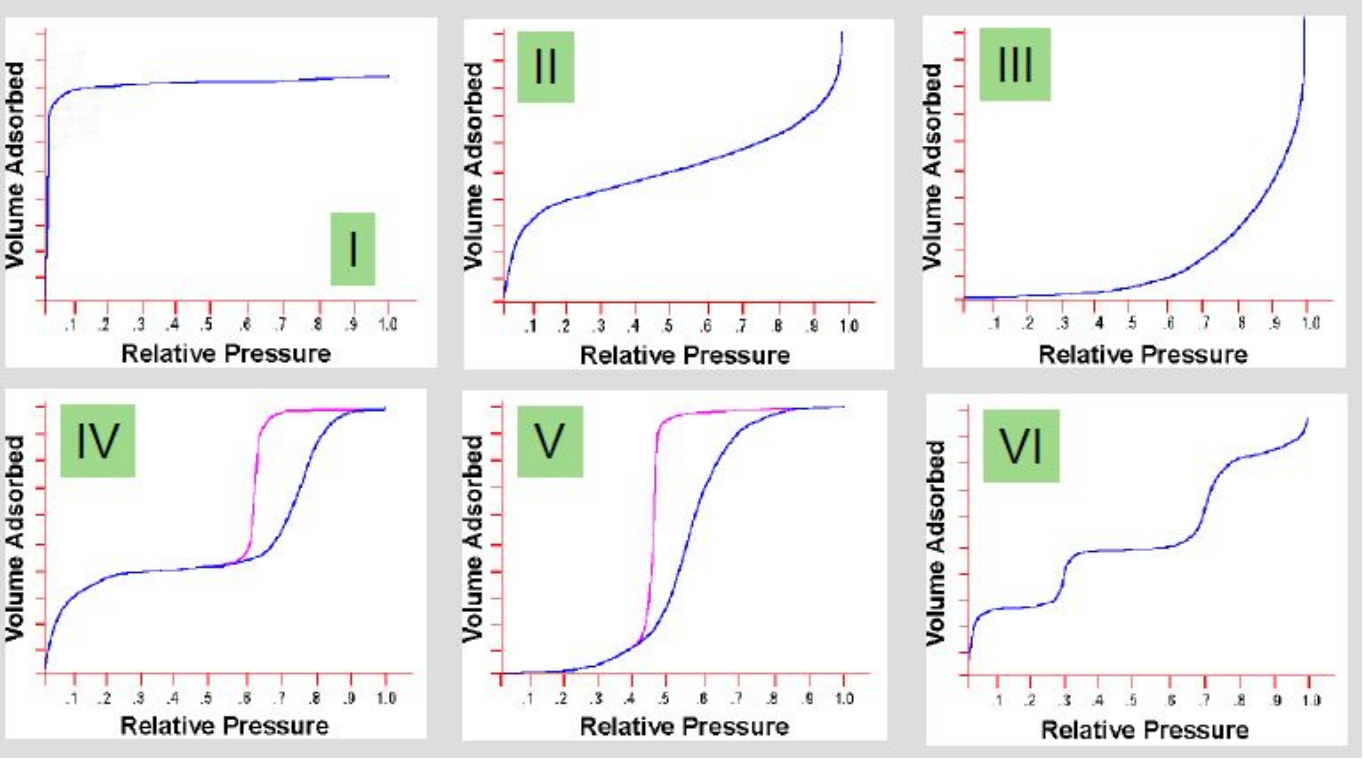

FIGURE 2.24: Adsorption Isotherms [12]

.

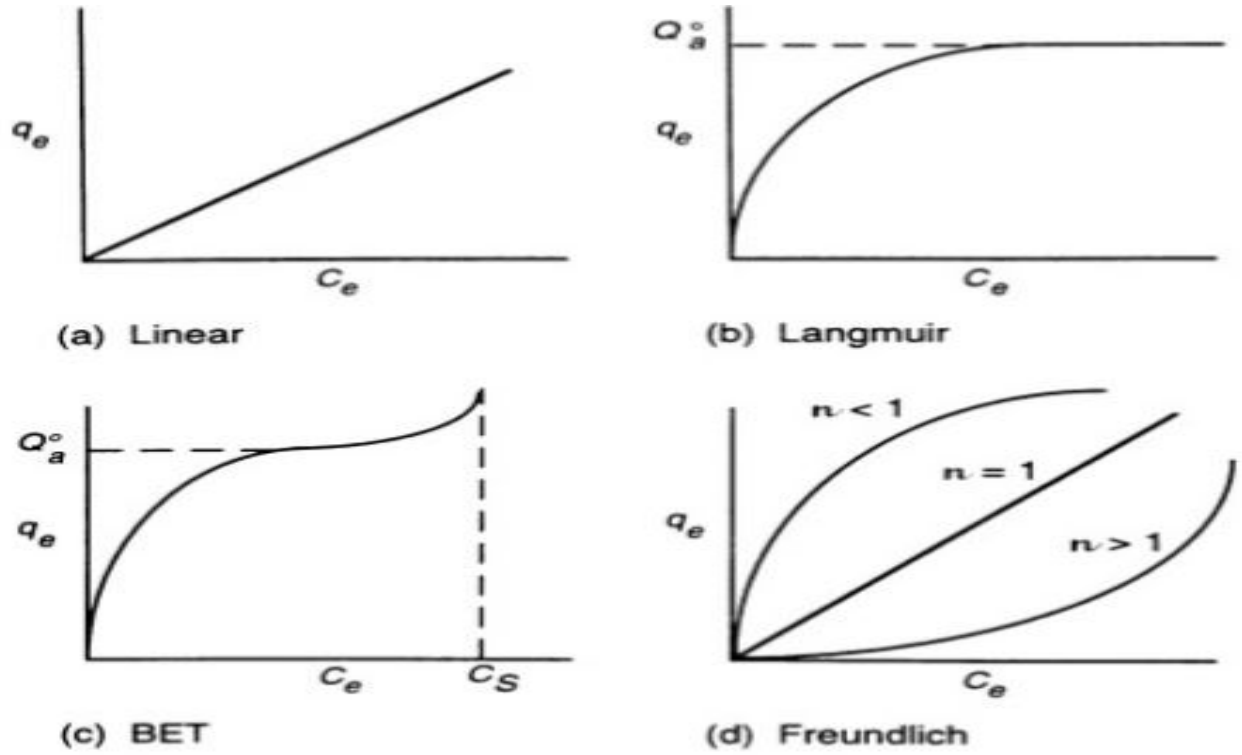

FIGURE 2.25: Basic Adsorption Theories [10]

.

Both adsorption isotherms and the basic adsorption theories are displayed in Figures 2.24 and 2.25 respectively. For the sake of this report, we shall discuss Langmuir (b) and BET (c) 2.25

Langmuir Theory: This theory assumes monolayer adsorption, so it could fit into chemisorptive situations. The equation was formulated based on the time lag between molecules hitting a surface and leaving the surface. Equation (2.31) was found in [99].

$$\frac{P}{V_a} = \frac{1}{V_m b} + \frac{P}{V_m} \tag{2.31}$$

Where:

- V_a = Gas adsorbed volume at pressure, P
- V_m = Gas volume required to form monolayer
- P = Adsorbate pressure
- b = Empirical constant

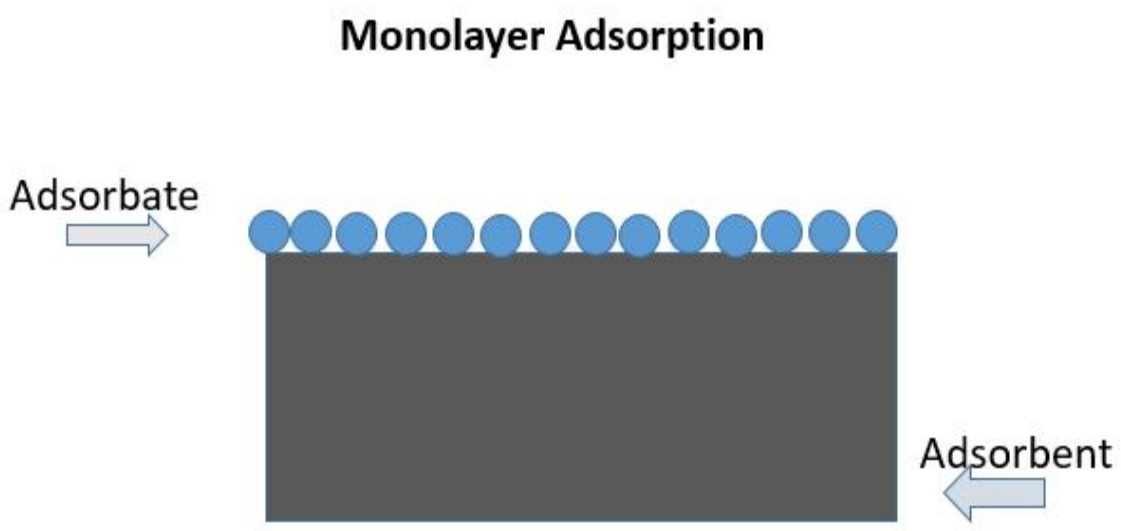

FIGURE 2.26: Schematic for Langmuir monolayer adsorption [11]

.

The assumptions of langmuir adsorption are:

- Identical adsorption sites – uniform surface
- Monolayer adsorption
- Adsorbed molecules do not interact amongst themselves [100].

BET Theory: The abbreviation 'BET' stems from the names of creators of this theory: Brunauer, Emmett and Teller [99]. This theory consolidates on the Langmuir theory, and assumes that the binding energy in multilayer adsorption is determined by forces active in gas condensation. If we then equate the evaporation rate from a layer to the condensation rate from same layer, and then repeat this process for infinite number of layers, we can obtain the BET equation (presented below):

$$\frac{P}{V(P_0 - P)} = \frac{1}{V_m c} + \frac{c-1}{V_m c P_0} \tag{2.32}$$

Where:

- P = N_2 partial pressure
- P_0 = Gas saturation pressure
- V = Adsorbed volume at P

- V_m = Adsorbed volume at monolayer coverage
- C = constant

The value of the constant, C (from 2.32) is defined in 2.33 and believed to be:

$$C \propto \frac{(q_1 - q_L)}{RT} \tag{2.33}$$

Where:

- q_1 = Heat of adsorption of first layer
- q_L = Adsorptive heat of liquefaction
- R = Gas Constant
- T = Absolute temperature

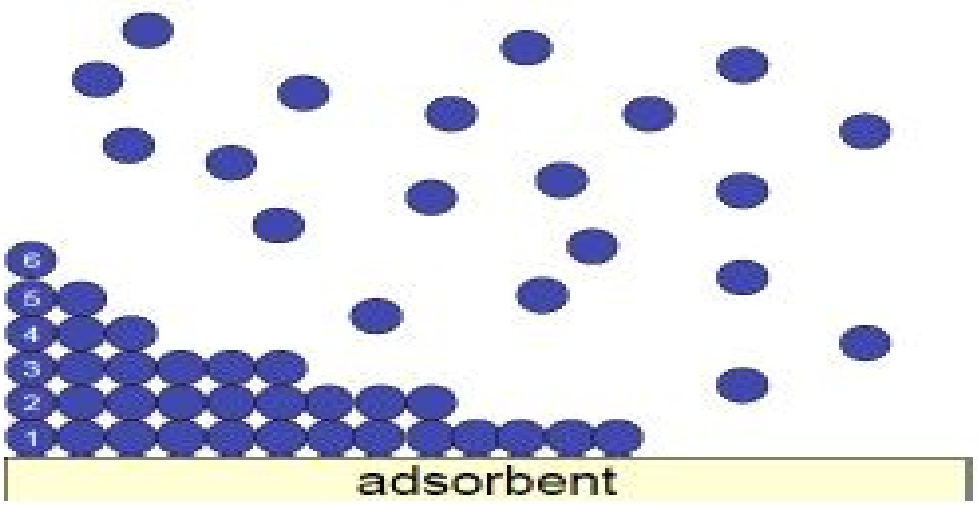

FIGURE 2.27: BET theory assumes Multilayer adsorption [11]

Figures 2.26 and 2.27 show monolayer and multilayer assumptions respectively.

The main assumptions of BET theory are:

- Binding energy in multilayer adsorption is determined by forces active in gas condensation
- No interaction between each adsorption layer
- The adsorption of gas molecules on a solid occurs in infinite layers.
- Each layer can be described by the Langmuir theory [100].

2.4.2 Applications of Adsorption and Activated Carbon

The applications of adsorption and activated carbon is presented in Table 2.9

TABLE 2.9: Applications of Adsorption and Activated Carbon

ADSORPTION	ACTIVATED CARBON
Gas Masks	As adsorbents
Purification	Remediation Purposes
Vitamin Preparation	Water and gas Purification
Heterogenous Catalysis	Medical Usage: to treat poison and ovedose,ingestion
Solid-liquid Chromatography	Mercury Scrubbing
Bacterial Filtration	Alcoholic Beverage purification

2.4.3 Scanning Electron Microscope

The Scanning electron microscope in Figure 2.28 provides details about the size and morphology of the particle, on a micrometer scale, but it doesn't give any molecular level details[11].

FIGURE 2.28: Scanning Electron Microscope [11]

Information that can be derived from SEM are: [11]

- Sample morphology
- Sample composition
- Sample crystal structure
- Sample topography

Precautions Taken

- Ensured proper documentation of all activities.
- Ensured that the proper personal protective equipment was used when working in the laboratory.
- Ensured that procedures were properly understood before embarking on any process.
- Ensured proper handling of fragile equipment in the laboratory.

Chapter 3

Experimental

In this chapter, the experimental work will be discussed alongside the proposed methodology to achieve the desired research objective.

3.1 Precursors for activated carbon and chemicals

Used local newspapers were picked up from around the vicinity, and this was used as the precursor for this process.

Different newspapers have their individual constituents, and this is often referred to as 'classified information' within the organization. Averagely, a newsprint paper is composed of both organic ($> 95\%$) and inorganic ($< 5\%$) part. The organic component could contain cellulose, lignin and it's variables (70-100%) while the inorganic component could have calcium carbonate, clay, titanium oxide, etc (0-30%) [101].

3.2 Experimental Set-up

3.2.0.1 Physical Activation

Waste paper was collected from around the premises. It was dusted and cut into sizes small enough to fit into the ceramic sample boat typically. 10g waste paper was put into the ceramic boat and placed into the high temperature furnace for carbonization. The furnace is typically connected to ammonia gas bottles via 6mm diameter flexible pipes. Initially, the Carbonization process begins by first saturating the furnace with ammonia gas for 20 minutes. After this, carbonization was conducted at 1000 °C , but the burn off was approximately 100%. Subsequently, the temperature interval was set within the range 600 °C to 900 °C. Physical

activation process proceeded with NH_3 gas at 600 °C and 700 °C for 1 hour. The heating rate was 10 °C/min in the high temperature furnace (see Figure 3.1). Sample was taken out after 60 minutes. AC6001A and AC7001A was prepared by this means. Table 4.1 contains details of the preparatory conditions.

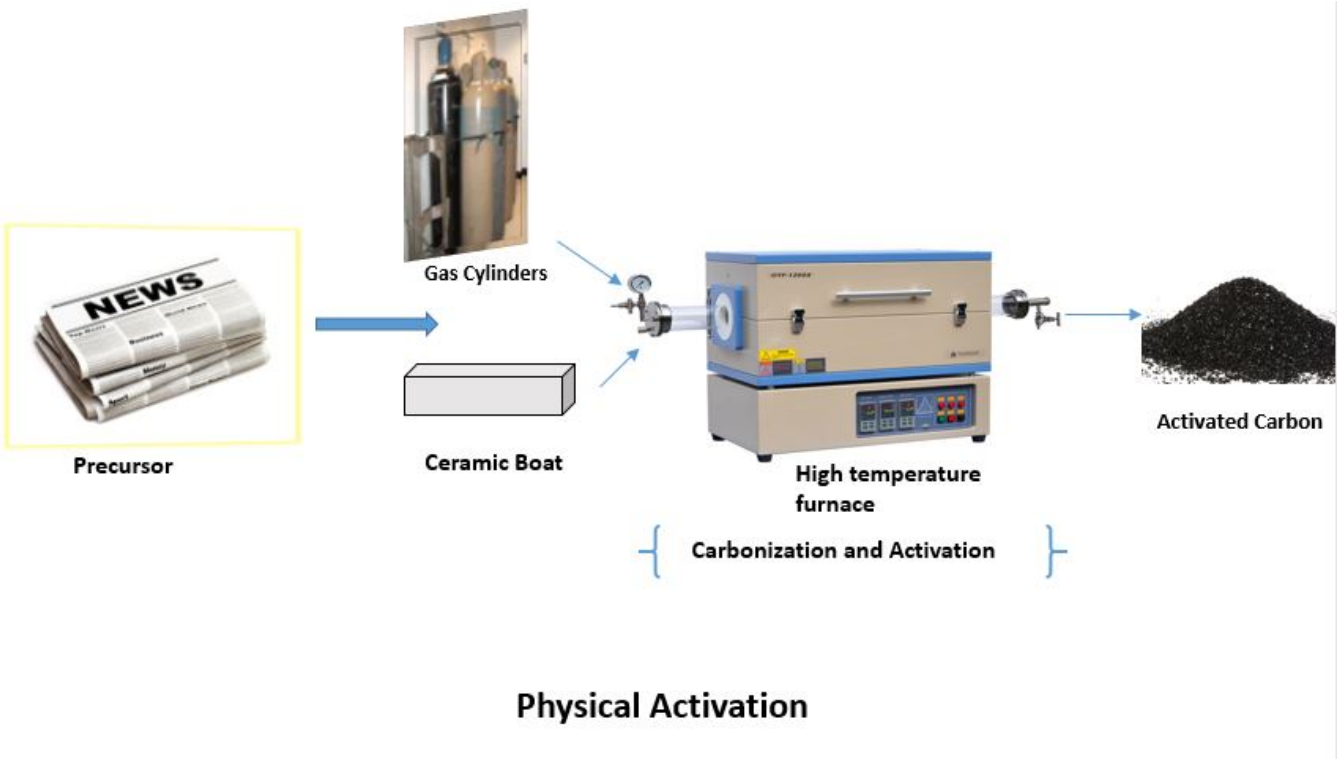

FIGURE 3.1: Experimental set-up for Physical Activation [13–16]

3.2.0.2 Chemical Activation

We switched to chemical activation since the results obtained from physical activation was not so great. 2.4g of precursor was impregnated with H_3PO_4 (as chemical agent) in the ratio of 1:1. A portion of this was inserted into the furnace and was activated with NH_3 at 800 °C and 900 °C for 1 hour. Heating rate was 10 °C/min.

After 1 hour, samples were removed and washed with 60ml 0.1M hydrochloric acid at 80 °C and stirring speed of 400rpm. The samples were washed with hydrochloric acid in order to remove any compounds of phosphorus that may be formed. The samples were then rinsed and drained (by filtration) and then dried overnight at 120 °C.

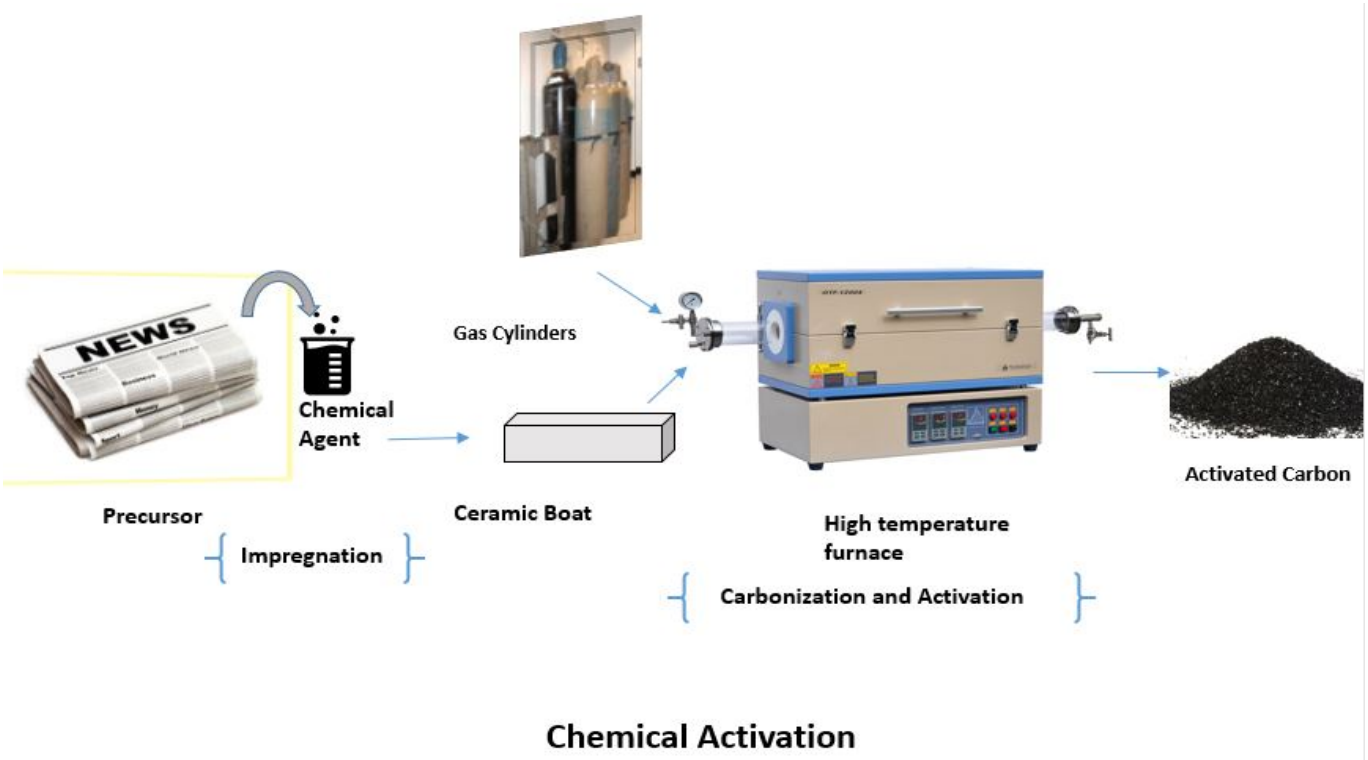

FIGURE 3.2: Experimental set-up for Chemical Activation [13–16]

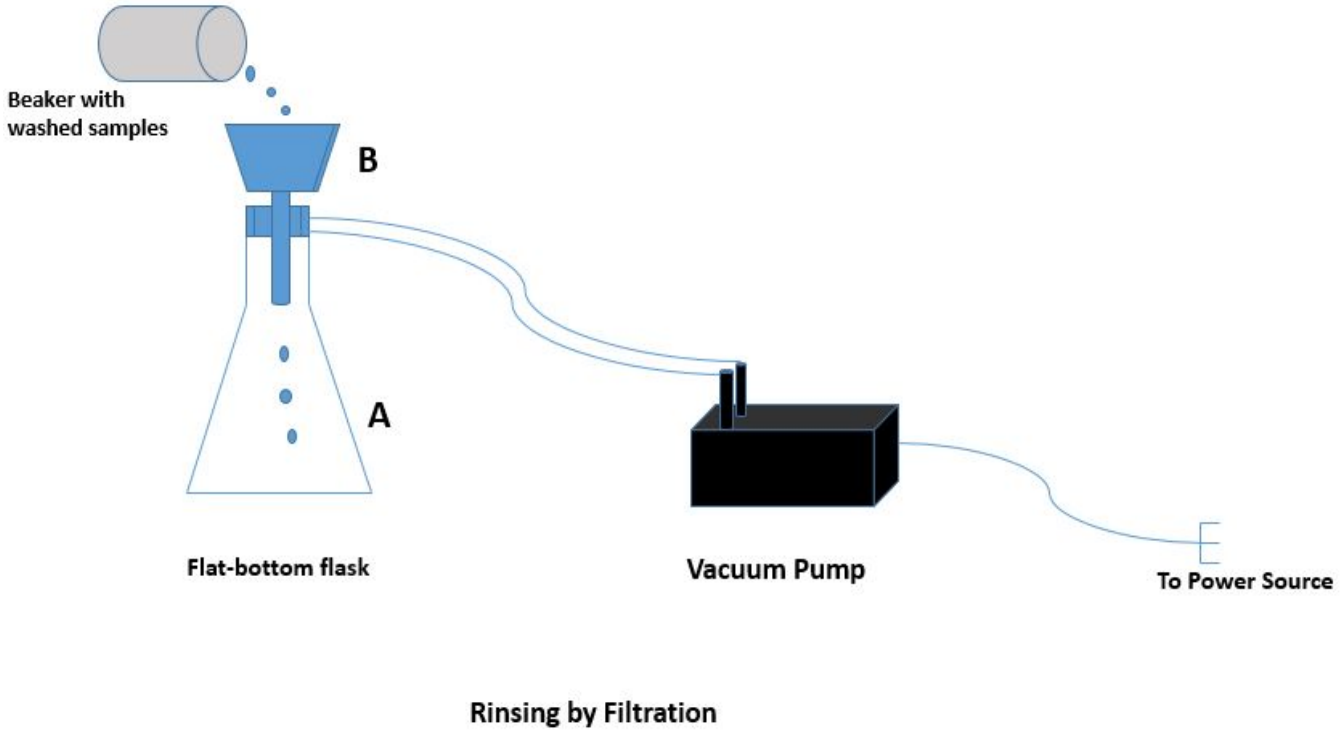

FIGURE 3.3: Rinsing by filtration

.

In Figure 3.3, the washed samples in the beaker are introduced into B section. Section B represents atmospheric condition. The vacuum pump creates vacuum condition in the A section. A

pressure drop is generated by pressure differences in the two sections, and this creates a suction effect to push down fluids down from B to A.
Samples AC8001A and AC9001A were prepared in this way.Table 4.2 contains details of the preparatory conditions.

The same process was repeated using potassium hydroxide as chemical agent. The potassium hydroxide pellets were weighed and mixed with the precursor to obtain a homogeneous mixture. This was then impregnated with water. The mixing with potassium hydroxide was done at different ratios of 1:1, 2:1, 4:1, and 1:2, also in both 1 and 2 step activation. The preparatory gas was changed from ammonia to nitrogen, and activation temperature range was between 600 °C to 850 °C. The activation time was 60 minutes (1-step) to 120 minutes (2-step). Heating rate was 10 °C/min in a horizontal furnace. Samples AC6001B, AC7001B, AC8501B, AC8502B, AC8502Bi, AC8502Ci, AC8502Ei, AC8504A, AC8504Ai were prepared by this method. Table 4.4 contains details of the preparatory conditions. Heating rate was 10 °C/min in a horizontal furnace.

Sample preparation was done by degassing with the Micromeritics Smartprep 065 unit at 120 °C for 6 hours. This unit applies mass action to alter chemical stability. The adsorbed molecule is kept at vacuum pressure and surface concentration. When heat is applied, the rate at which the adsorbed molecules shift to the inert environment is increased.

This (degassing) process detaches impurities from the surface and pores of the samples. The samples are then transferred to the TriStar II Plus Surface Area and Porosity Analyzer. Specific measurement points are selected, and the amount of gas adsorbed at -196 °C is evaluated. The amount of gas contained on the sample surface tallies with the total surface area of the samples. By calculating the volume of gas analogous to a surface monolayer, the BET surface area is dretermined [102, 103].

3.2.0.3 Scanning electron microscopy and EDX

The samples were first milled into powder and then placed on a sample mount with a sticky conducting tape. This tape has two functions: firstly, it keeps the powdery samples in place, so that it doesn't adhere to the SEM's (Zeiss Supra 35VP) sensitive optics column. Secondly, it ensures electrical connectivity of samples to the mount holder to prevent electron beams from charging and misconstruing the images. The samples were then placed in a vacuum chamber to ensure further stability of samples to the mount holder.

After these, the samples were then registered into the SEM's software database. This software then requests commands to acquire loading of image and sample. The toolbar command is used to select various magnification and focus points, and the "scan marker" creates a line section for area of interest.

The next step involves stage control. The joystick is used for this purpose. The SEM keyboard makes it easier to find and position the SEM images by turning the contrast knob [104].

An acceleration voltage of 15 kV, aperture of 30um and a working distance of 8.6 mm to 10.7 ml was adopted for the various samples. The different magnifications can be found in Figures 4.16, 4.17, and 4.18.

3.2.0.4 Supercapacitor Assembling and testing

The prepared carbon powder was milled with 8 wt % Polytetrafluoroethylene (PTFE) in an aqueous solution (Sigma–Aldrich) and a small amount of water. The carbon–PTFE mixtures were used to fabricate supercapacitor electrodes by pressing the mixtures over a nickel foam disk (Alfa Aesar) at 6 MPa for 2 min. The mass loading (2 mg cm^{-2}) of the active material was measured accurately for each electrode. The electrodes were dried in a vacuum oven at 120 °C for 12 h before assembly. Electrochemical tests in this study were conducted in a two-electrode cell configuration using split cells. The assembly of the cell components was performed in a glovebox filled with argon. Two electrodes with the same loading were separated by a 25 micron thin microporous monolayer membrane (Celgard 3501) separator. 15 ml of neat EMIMBF4 (Sigma–Aldrich) electrolyte was added to each side of the separator. The prepared supercapacitors were stabilized at room temperature overnight before performing the performance tests. Charge and discharge tests and cycling stability tests were performed on a MTIS 8-channel battery analyzer. The gravimetric capacitance of a single electrode was calculated from the galvanostatic discharge curve according to $C_{sp,electrode} = 4\,\mathrm{l/mV}$, where I is the constant discharge current, m is the total mass of both active materials on the electrodes, V is the voltage change during the discharge process (excluding the voltage drop at the beginning of the discharge), and t is the duration of the discharge process.

3.2.1 Materials Involved

- Potassium hydroxide pellets from Yara paraxair AS
- Ammonia gas from Yara paraxair AS
- Nitrogen gas from Yara paraxair AS
- 0.1 Mole Concentration of Hydrochloric acid from Fischer scientific

Chapter 4

Results and Discussion

4.1 Gas Phase Adsorption Analysis

Materials are able to adsorb other substances as a result of surface energy, as depicted in Figure 2.22. Activated carbon is a well known adsorbent. This is because it can be used to adsorb various substances. The adsorbate refers to the material being adsorbed. In this case, the adsorbate is nitrogen gas at -196 °C. The activated carbon is first degassed at vacuum conditions, and the nitrogen is made to fill the adsorption sites of the activated carbon at different pressures. This is covered in Chapter 3.

The inherent qualities of the produced activated carbon would decide its application. These qualities are controlled by the preparatory process and conditions. The produced activated carbon samples were characterized by nitrogen gas adsorption, and the result analysis are presented herein.

4.1.1 Physical Activation

Samples AC6001A and AC7001A were prepared using the physical activation method. The preparatory conditions and test results are summarized in Tables 4.1 and 4.2

Table 4.1: Physical Activated Carbon Preparatory Conditions

Sample Name	Preparatory gas	Activation time	Washing Condition (temp, rpm)	Washing duration (time)	Drying Condition (temp, time)
AC6001A	Ammonia	60 minutes	60 °C , 400	120 minutes	120 °C, Overnight
AC7001A	Ammonia	60 minutes	60 °C , 400	120 minutes	120 °C, Overnight

TABLE 4.2: Properties of Physically Activated Carbons

Sample Name	Specific Area (m^2/g)	Micro-surface Volume (m^2/g)	Meso-surface Volume (m^2/g)	Micro-pore Volume (cm^3/g)	Meso-pore Volume (cm^3/g)	Total-pore Volume (cm^3/g)
AC6001A	50.0805	38.25	11.8305	0.016446	0	0.016446
AC7001A	480.1255	387.6541	92.4714	0.174069	0	0.174069

Adsorption Isotherms and Pore Size Distribution

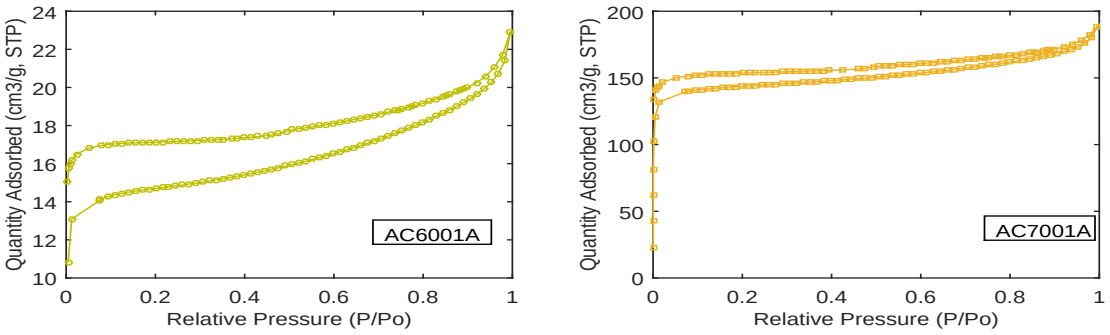

FIGURE 4.1: Adsorption Isotherm for AC6001A and AC7001A

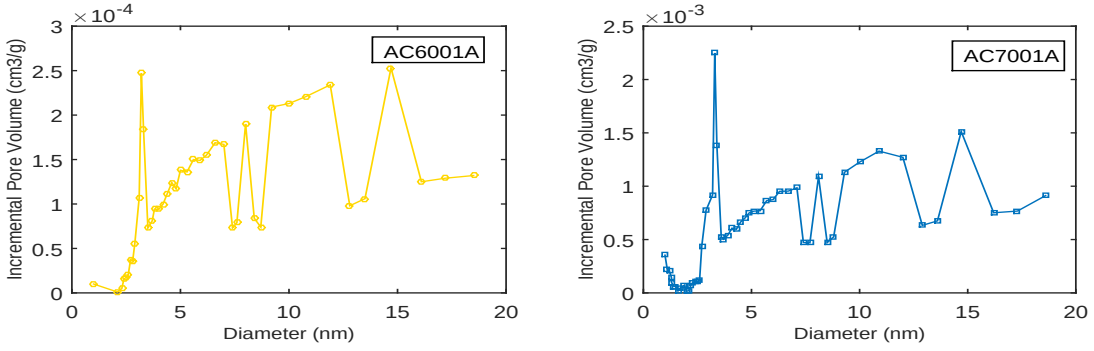

FIGURE 4.2: Pore size distribution for AC6001A and AC7001A

Samples AC6001A and AC7001A were prepared using the physical activation process. Matching the charts above with the six basic adsorption isotherm types shows a close resemblance with type 2 and type 1B Isotherms respectively. Sample AC7001A was ascertained to be microporous, but AC6001A was mesoporous.

Both Samples depict the existence of micropores, as seen in Figure 4.1. These micropores cease in the mid-section, as small mesopores are noticed, before an extension to capillary condensation. Usually, adsorption may advance into single layer, multilayer or capillary condensation. The latter involves multilayer formation in a vapour phase in porous media [100].

The pore size distribution plots are displayed on Figure 4.2. They potray an array of micro and mesoporous materials with a multimodal distribution structure. It depicts a worm-like framework, which can be verified from the SEM images. The average pore diameter of AC6001A and AC7001A are 2.75nm and 2.35nm. These sets of information can be found in Tables 4.1, 4.2 and Figures 4.1, 4.2.

Figure 4.3 displays the effect of temperature on the surface area and pore volume of the prepared samples. There is an increase in both the surface area and the pore volume of the physically activated carbons. However, when the temperature was increased to 1000 °C, all samples were burnt.

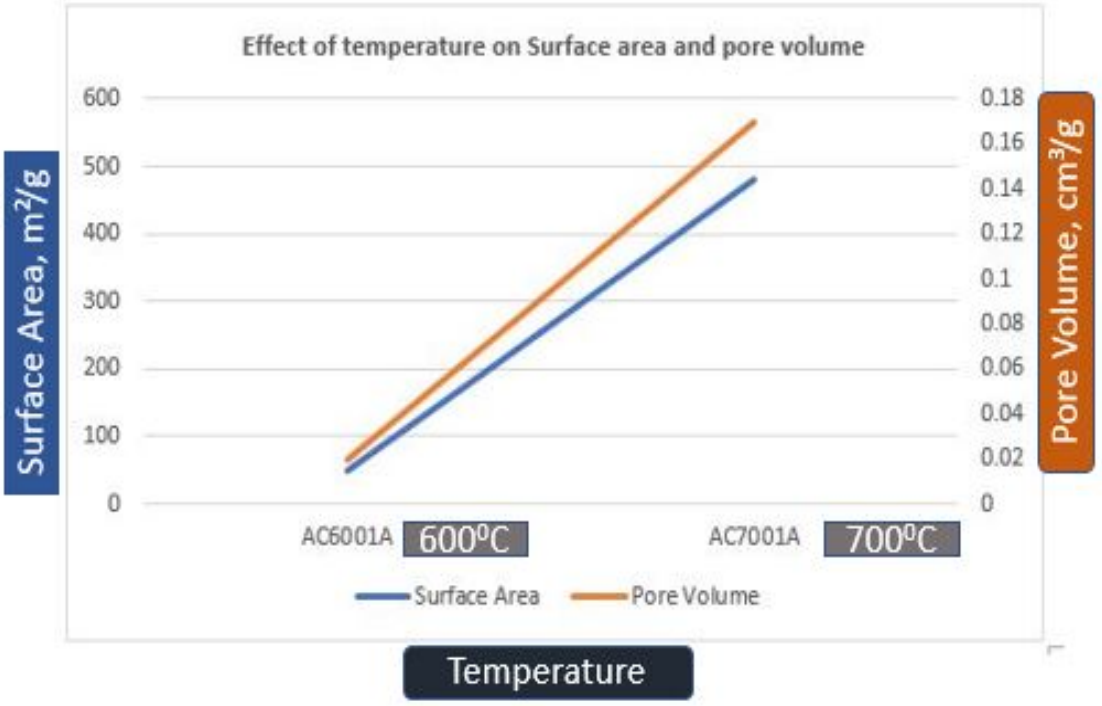

FIGURE 4.3: Effect of temperature on Surface Area and Pore Volume

4.1.2 Physical+Chemical Activation

Samples AC6001B and AC7001B were prepared using the physical activation method, and then Chemical Activation. The preparatory conditions and test results are summarized in table 4.3

TABLE 4.3: Physical+Chemical Activation conditions

Sample	Activation Conditions	Preparatory Conditions (Ratio of KOH to Precursor/step)	Specific Surface Area (m^2/g)	Total Pore Volume (cm3/g)
AC6001B	Nitrogen gas, 850 deg C	4:1 / 1 Step	247.5905	0.136333
AC7001B	Nitrogen gas, 850 deg C	4:1 / 1 Step	416.2009	0.263080

In order to enhance the properties of prepared activated carbons, some samples were further subjected to chemical activation after the physical activation stage. Samples AC6001B and AC7001B were activated using this method. Figures 4.4 and 4.5 shows plots of the properties of these samples.

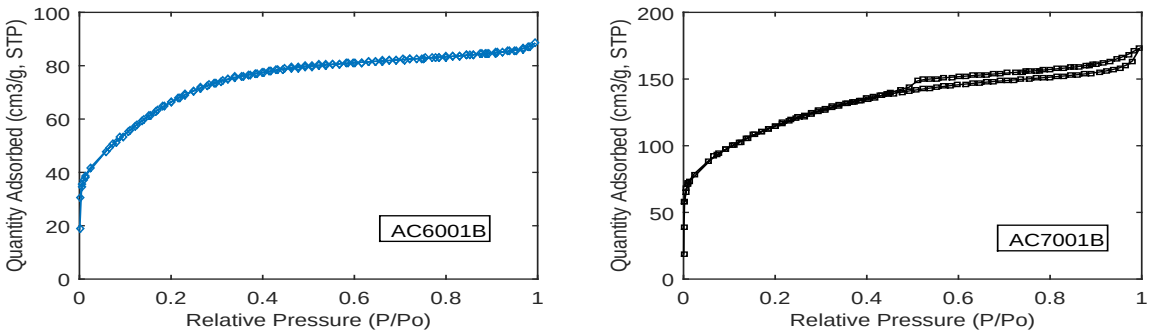

FIGURE 4.4: Adsorption Isotherm for AC6001B and AC7001B

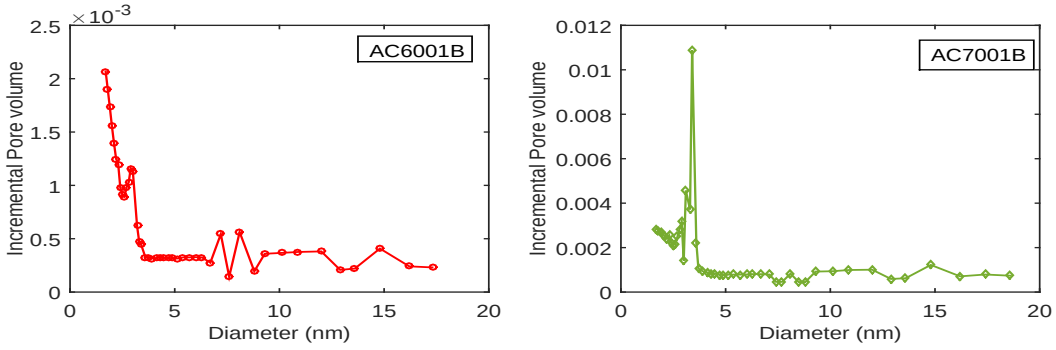

FIGURE 4.5: Pore size distribution for AC6001B and AC7001B

Figure 4.4 shows the nitrogen adsorption isotherms for samples AC6001B and AC7001B. Samples AC6001B and AC7001B fall into the type 1A IUPAC Isotherm class. It is relatively microporous with low mesoporosity details.

The pore size distribution data on figure 4.5 shows a rather predominant unimodal size distribution, which is quite regular. The average diameter range for AC6001B is 1.7-17.3 nm, while that of AC7001B is 1.7 nm -18.6 nm .

Figure 4.6 portrays the effect of temperature on samples prepared by combination of physical and chemical activation. It can be observed that, an increase in temperature causes both the surface area and pore volume to increase. There is an enlargement from microporosity to mesoporosity with temperature increase. The surface area of the first sample (AC6001B) increased almost 5 times, but the second sample (AC7001B) was almost relatively unchanged.

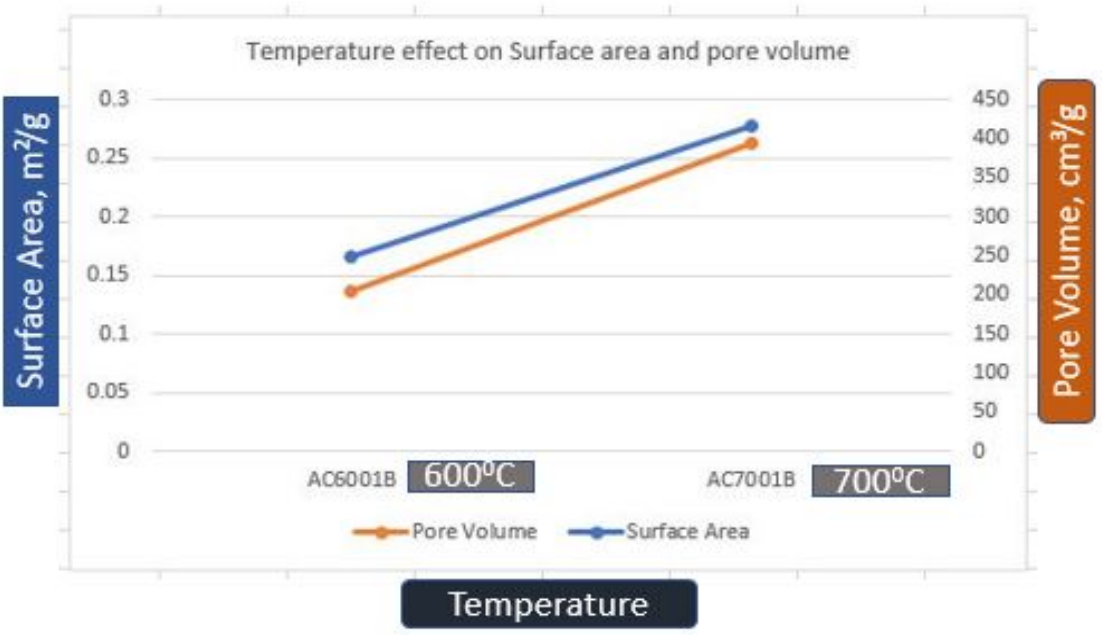

FIGURE 4.6: Effect of temperature on Surface Area and Pore Volume

4.1.3 Chemical Activation

Samples AC8001A, AC9001A, AC8502B, AC8502Bi, AC8502Ci, AC8502Di, AC8504A, and AC8504Ai were prepared using the chemical activation process. The details of preparation are shown in Table 4.4.

TABLE 4.4: Chemical Activation Conditions

Sample	Activation Conditions	Preparatory Conditions (Ratio of KOH to Precursor/step)	Specific Surface Area (m^2/g)	Total Pore Volume (cm3/g)
AC8001A	Ammonia gas, 800 °C	H3PO4 / 1 Step	559.8376	0.197037
AC9001A	Ammonia gas, 900 °C	H3PO4 / 1 Step	105.8379	0
AC8502Di	Nitrogen gas, 850 °C	KOH / 2:1/ 2 Step	1 014.0997	0.537820
AC8502B	Nitrogen gas, 850 °C	KOH / 1:1/ 1 Step	804.9325	0.419662
AC8502Bi	Nitrogen gas, 850 °C	KOH / 1:1/ 2 Step	729.5798	0.385334
AC8504Ai	Nitrogen gas, 850 °C	KOH / 4:1/ 2 Step	518.8807	0.328885
AC8504A	Nitrogen gas, 850 °C	KOH / 4:1/ 1 Step	381.0096	0.283106
AC8502Ci	Nitrogen gas, 850 °C	KOH / 1:2/ 2 Step	54.2841	0.189000

Adsorption Isotherms: Amongst the chemically activated samples, AC8501B and AC8502Di are type 1A, AC9001A, AC8504A, AC8504Ai are type 2, AC8001A; type 1B and both AC8502Ci and AC8502Bi belong to types 3 and 5, and they are initiated by conditions that are not so significant in pore and surface analysis [99]. The samples largely display mesoporosity as a result of the adopted BJH model that focuses on mesoporous pore size distribution.The discrepancy of pore details could be attributed to the pre-carbonization conditions. These conditions affect the pore development in a positive or adverse manner. Some samples activated with potassium hydroxide seem to have well developed microporosity and also mesoporous content. Samples AC8502B, AC8502Bi, and AC8502Di show this (4.4). This multi/hierarchical pore structure is necessary for enhanced performance as supercapacitor electrode materials [71, 105]. The activation by phosphoric acid focuses on microporosity development with little mesoporosity details. This is seen in samples AC8001A and AC9001A with pore sizes 2.3 nm and 2.1 nm respectively. The adsorption isotherm plots can be found in figures 4.7, 4.8, 4.9, and 4.10.

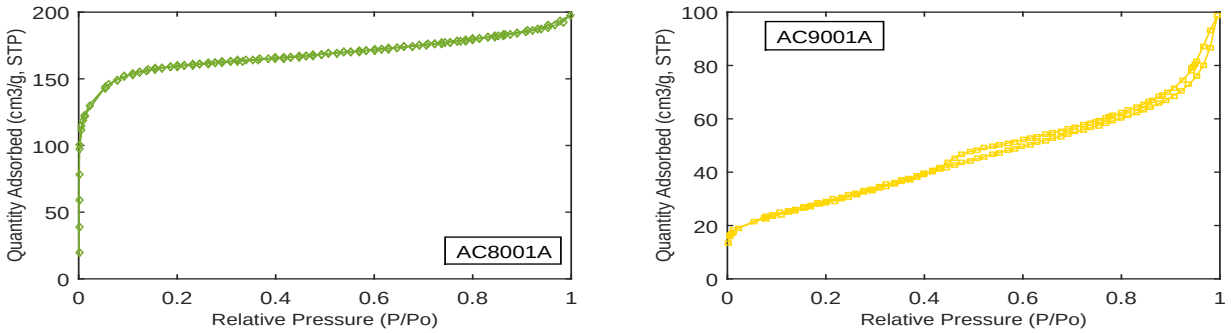

FIGURE 4.7: Adsorption Isotherm for AC8001A and AC9001A

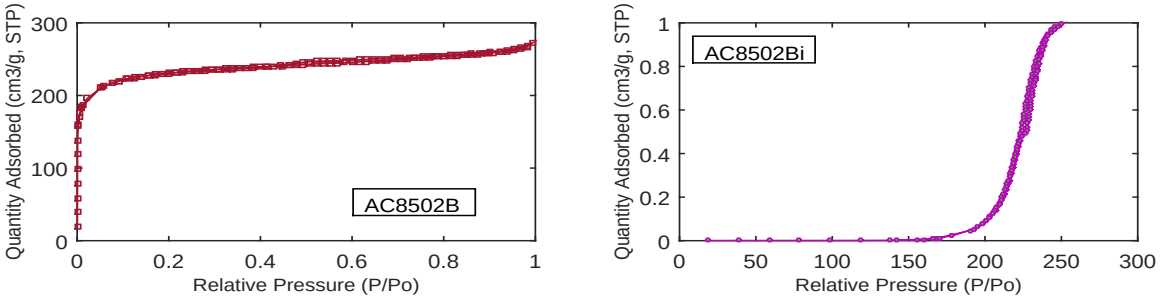

FIGURE 4.8: Adsorption Isotherm for AC8502B and AC8502Bi

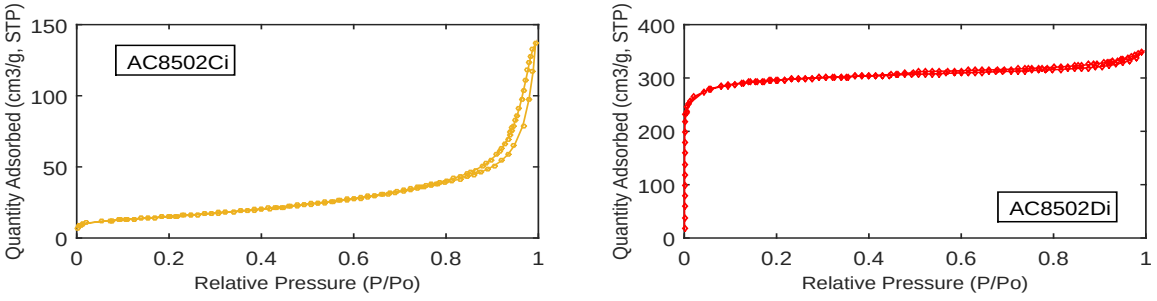

FIGURE 4.9: Adsorption Isotherm for AC8502Ci and AC8502Di

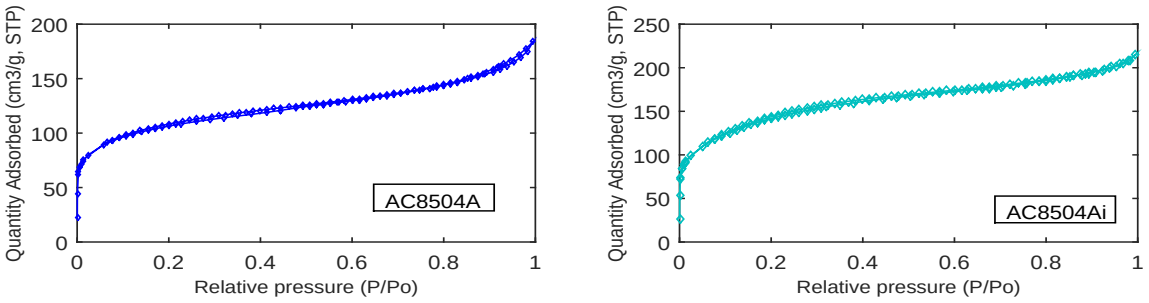

FIGURE 4.10: Adsorption Isotherm for AC8504A and AC8504Ai

The pore size distribution of the chemically activated samples (Figures 4.11, 4.12, 4.13 and 4.14) display some specific details about this group. There is a general skewing to the right side, which is expected. Sample AC8001A has peak values of incremental pore volume at about 15 nm; this peak was however experienced earlier in sample AC9001A at about 3 nm average diameter. Sample AC8001A is microporous while AC9001A is a type 4 non-porous adsorbent.

Samples AC8502B and AC8502Bi both display a unimodal narrow pore size distribution in the 3-5 nm average diameter range [100]. These samples were similar in the structure of their pore size distribution and also had high surface areas and pore volumes. They are both mesoporous and have similar coefficient of variation values of 0.7887 and 0.7808 respectively.

Sample AC8502Ci has a multimodal structured pore size distribution with values skewing upwards to the right. Sample AC8502Di on the other hand, had a regular mesopore-structure pore size distribution, with peaks around 2-4 nm of average diameter. It also exhibited very high surface areas of over 1000 m^2/g and maximum pore size range of 12.9 nm. The coefficient of variation for this sample was 0.68 which was lower than 0.73 for AC8502Ci.

Sample AC8504A has an irregular structured pore size distribution. This was a bit similar to that displayed by samples AC8001A and AC8502Ci. All three samples exhibited low surface areas. The coefficient of variation for AC8504A was 0.321, which was the lowest of them all. Sample AC8504Ai had the most irregular pore size distribution structure, with no peak values dipping downwards. The coefficient of variation for the incremental pore volume values was slightly higher than that of AC8504A. The disrupted pore size distribution structure is believed to have been caused by the high concentration of KOH. The surface areas for both samples were not as high as expected.

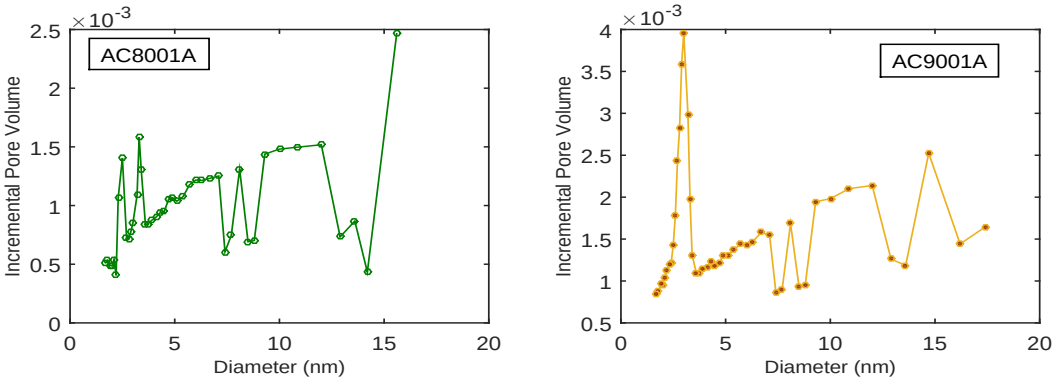

FIGURE 4.11: Pore size distribution for AC8001A and AC9001A

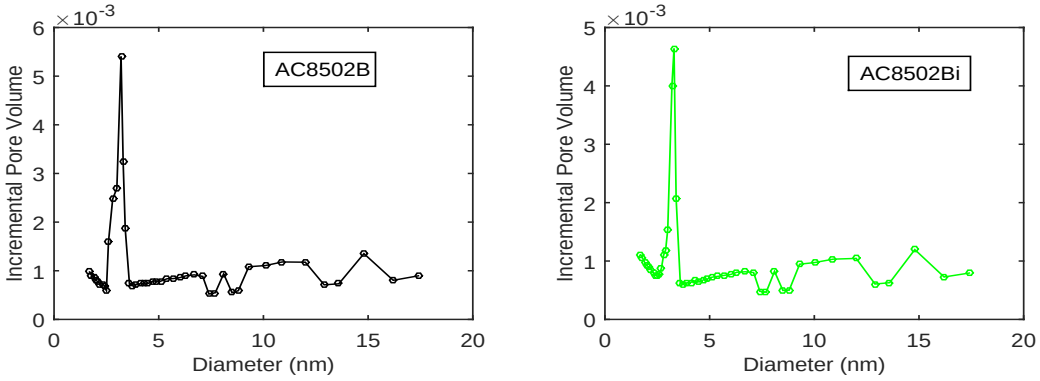

FIGURE 4.12: Pore size distribution for AC8502B and AC8502Bi

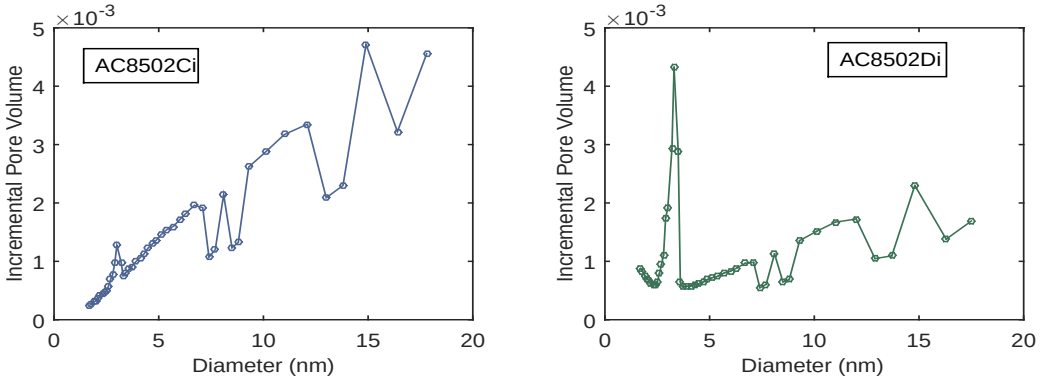

FIGURE 4.13: Pore size distribution for AC8502Ci and AC8502Di

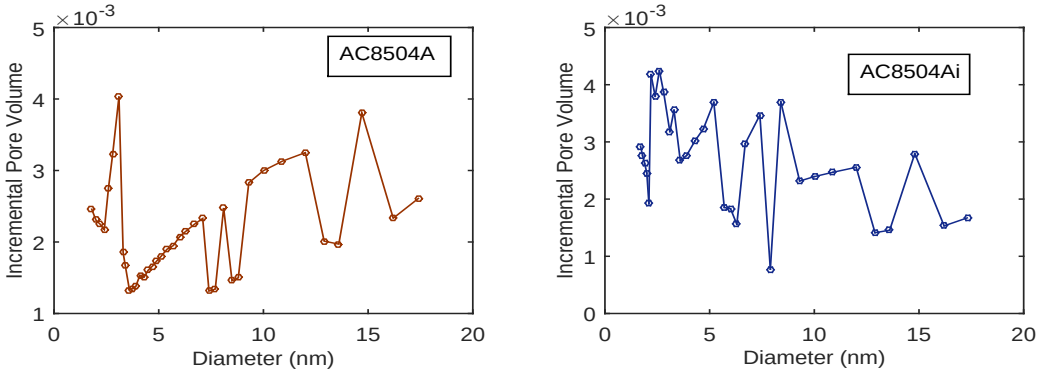

FIGURE 4.14: Pore size distribution for AC8504A and AC8504Ai

Effect of temperature and number of steps on surface area and pore volume

In Figure 4.15, the vertical left axis represents the specific surface area of the sample, while the vertical right axis represents the pore volume. The horizontal axis identifies the sample,impregnation ratio and number of steps, these parameters are also described in table 4.4. The number of steps is closely related to the amount of time the precursor spends in the reactor. Typically, a 1-Step process lasts for about 60 minutes, while a 2-Step process takes about two housr for activation. The two step activated samples had both the highest and lowest surface areas and pore volume. The highest surface area was exhibited by sample AC8502Di at 850 deg C, while the lowest was observed in sample AC8502Ci. This low surface area resulted from insufficient precursor to react with KOH. This inhibits the creation of pore spaces and shrinks the surface area.

The samples activated chemically in 1-step also exhibited fairly high surface areas at the right temperature. Mean values of the 2-step activated samples was higher and the coefficient of variation was 0.637 for 1-Step and 0.6984 for the 2-Step. This step superiority can only be significant at the right temperature. Generally, high temperatures are necessary to attain high pore structures. However, when the temperature becomes too high, the pore structure is blighted and distended [106].

FIGURE 4.15: Effect of Temperature and Number of steps on Surface area and Pore volume

As a result of these, it was discovered that the optimal temperature range to obtain best surface area was between 800 deg C to 900 deg C. A surface area greater than 1000 m^2/g was obtained from this temperature range.

Effect of impregnation ratio (KOH:precursor) on surface area and pore volume The effect of impregnation ratio on surface area and pore volume can be likened to that of The law of diminishing returns. There is a significant increase in surface area when the ratio is equivalent (1:1). The surface area increases further when the ratio is set to 2:1. However, a doubling of the ratio from that point (2:1) creates a reverse effect; a reduction in surface area. This decrease is almost 50 percent from the original value. This is as a result of rupturing of the created surface area by excess potassium hydroxide.

4.2 Scanning Electron Microscopy Characterization

The scanning electron microscopy technique is used to obtain the morphology and crystallographic structure of substances. This procedure is extremely useful because it allows a direct visual observation of the physical appearance of the sample. This gives an even better perception of the sample.

Some samples were selected for the SEM process, but only four of them was presented for convenience. These four represent samples with the highest and least surface areas and pore volumes. Samples AC8502B, AC8502Di, AC8504A and AC6001A were employed for this purpose.

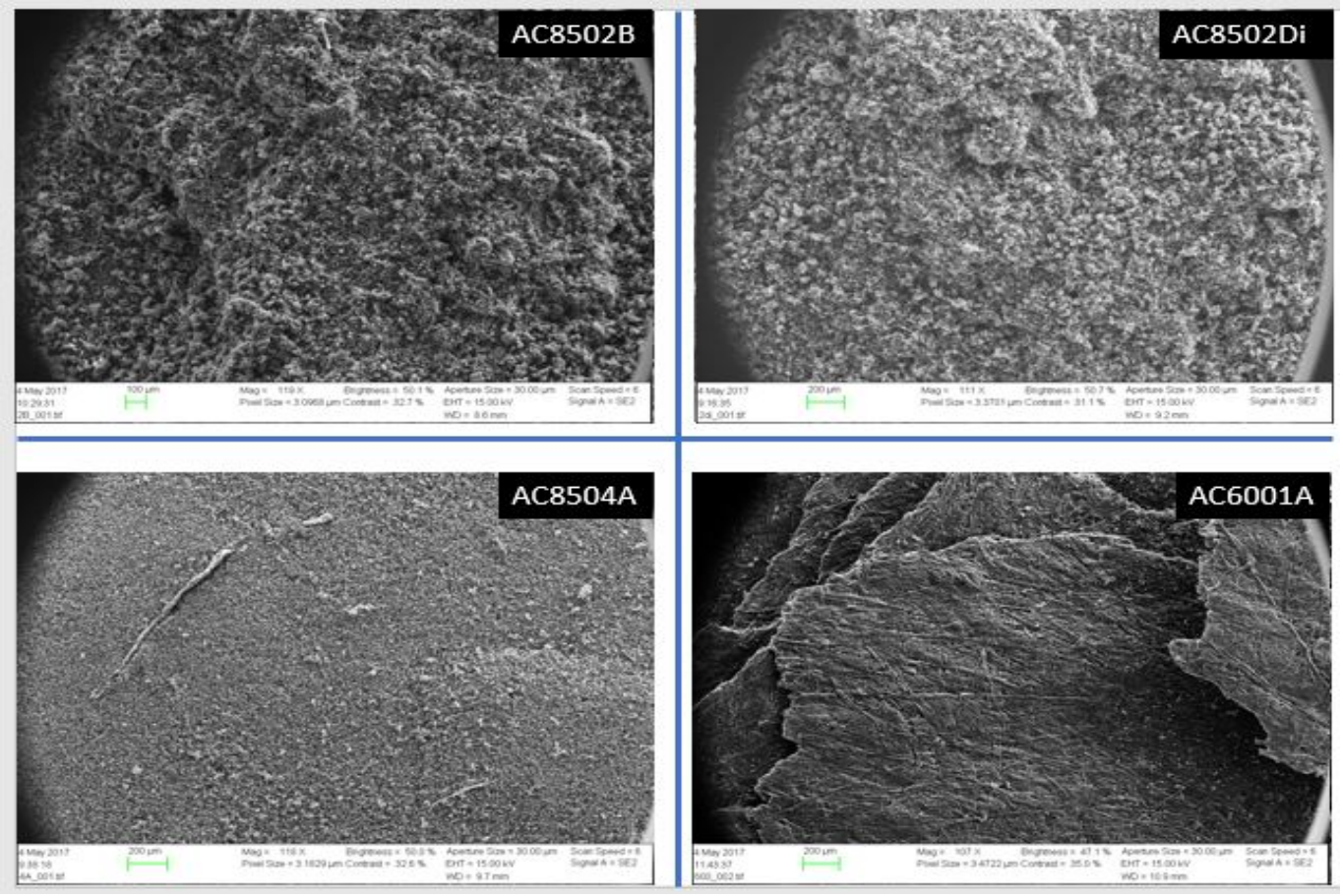

FIGURE 4.16: SEM images with magnification of approximately 120 times

Figure 4.16 shows images with magnification of approximately 120 times. Samples AC8502B and AC8502Di show a large surface area with pores. These pores are not so visible on this magnification, but the surface area can clearly de identified. Sample AC8504A has a tight-looking surface morphology with almost invisible pores. An unidentified worm-like structure can also be seen. Sample AC6001A had a dry-looking surface morphology, with no pores at first sight of this magnification.

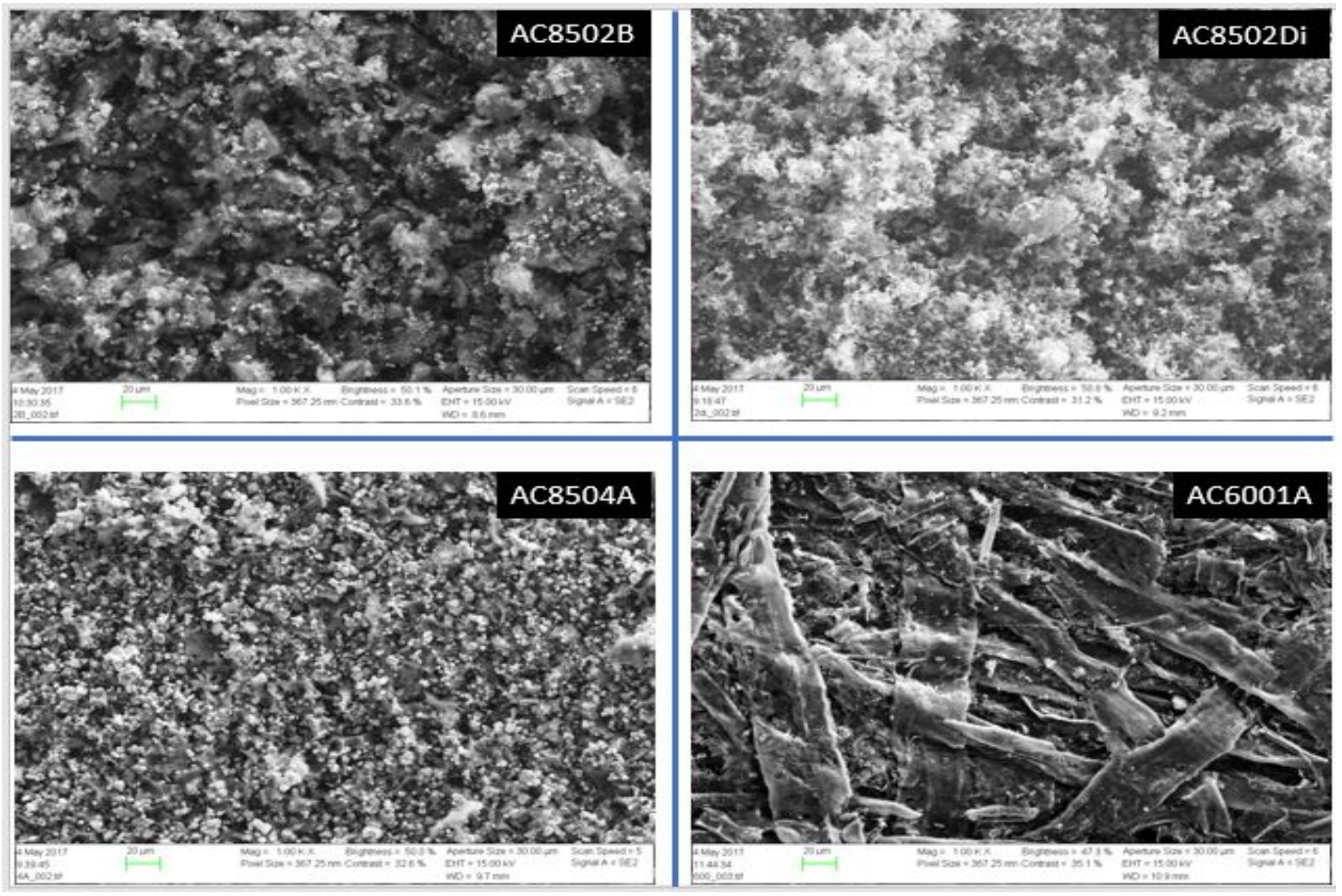

FIGURE 4.17: SEM images with magnification of approximately 1000 times

Figure 4.17 above shows images with magnification of 1000 times. Samples AC8502B and AC8502Di show similar surface morphology. They both possess loose exterior structure with pores, and many active sites can be envisaged from this appearance.

Sample AC8504A displayed a clasped facial morphology with almost no sight of pore structure, while sample AC6001A had cross layers of fibre-framework stacked upon each other.

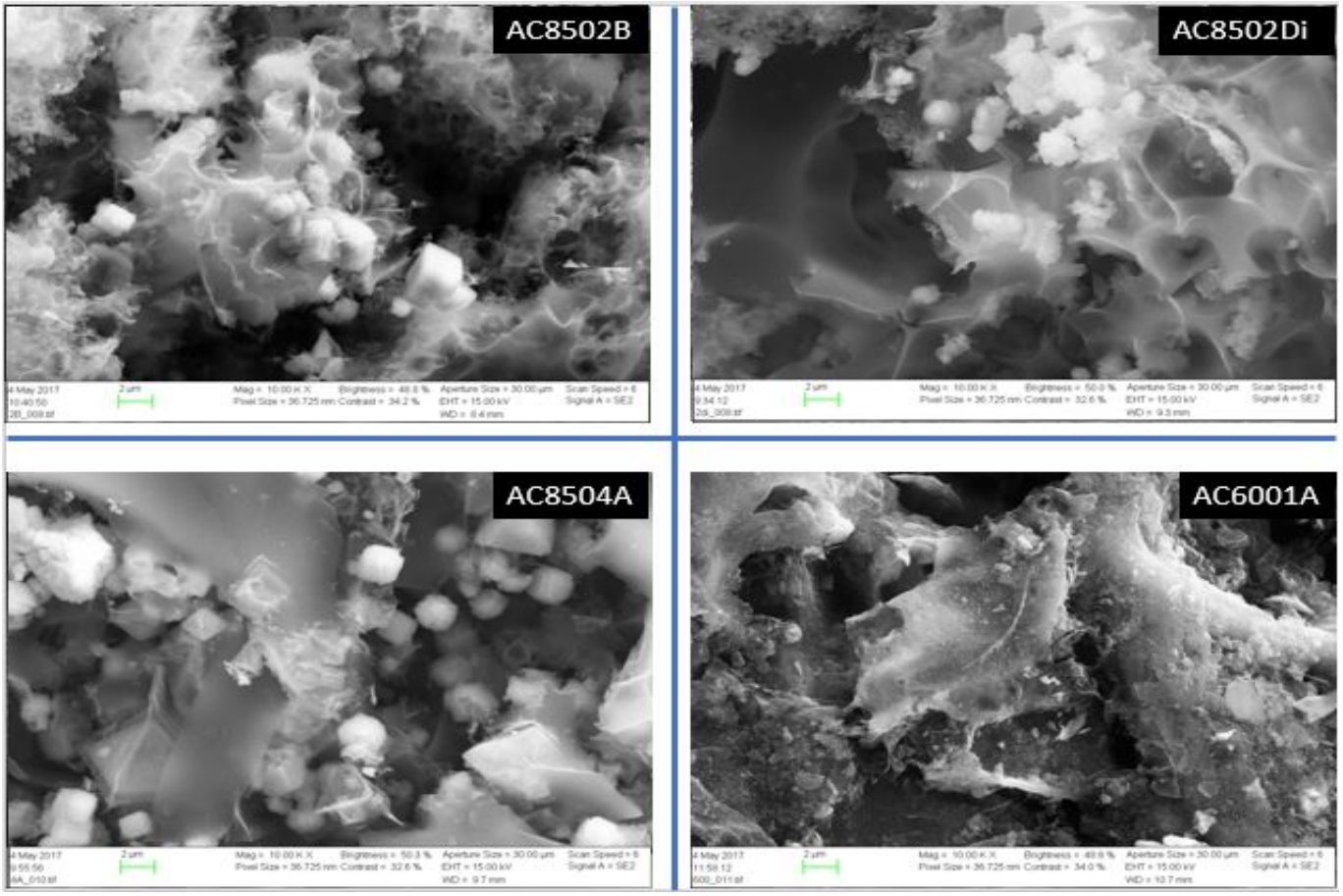

FIGURE 4.18: SEM images with magnification of approximately 10000 times

Figure 4.18 shows SEM images with magnification of 10000 times the original size. Sample AC8504A shows a lot of cube-shaped crystals with closed voids. Both samples AC8502B and AC8502Di had fewer of same crystals with open voids; but sample AC6001A exhibited a totally different morphology on this magnification, with a non-connected packed void structure.

4.2.1 Energy-dispersive X-ray Spectroscopy

This process is used to identify individual elements in a sample. It is usually achieved by directing beams of electrons onto a sample to jet off X-rays, which are collected by a detector to create voltage signals. This procedure is effective in the identification of sample constituents because every element has an exclusive atomic structure.

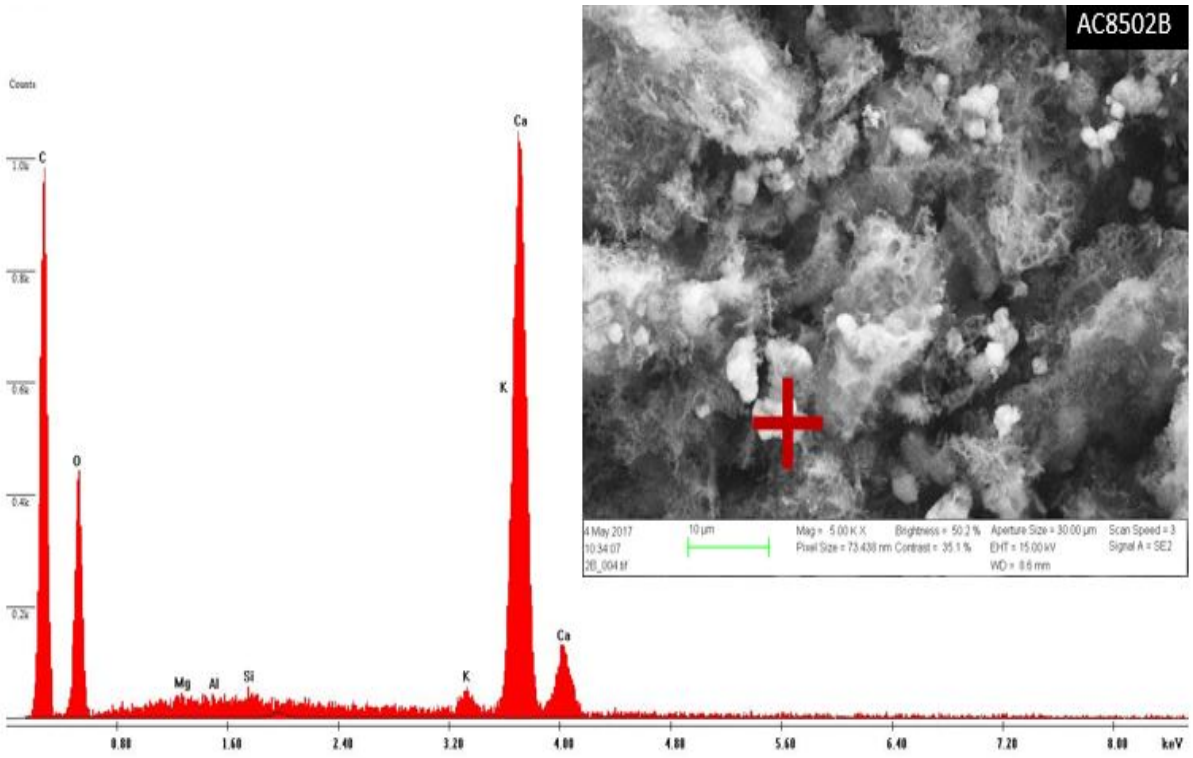

FIGURE 4.19: Energy-dispersive X-ray Spectroscopy for AC8502B

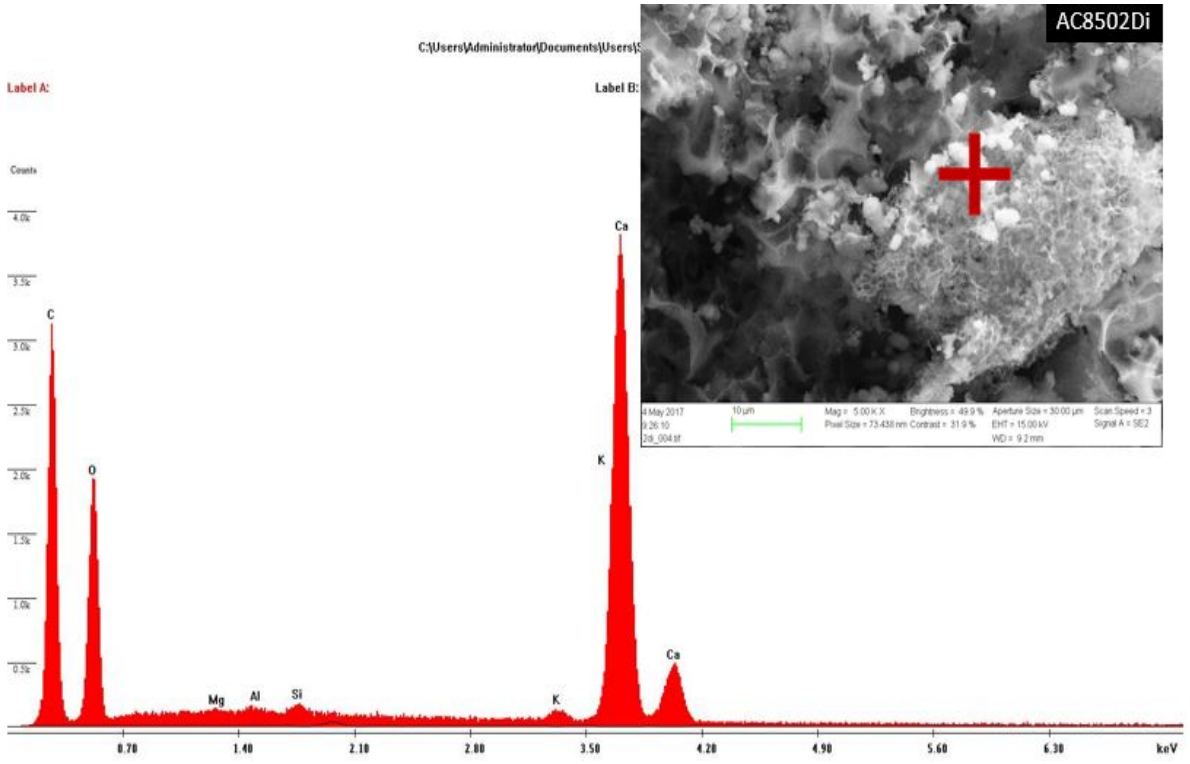

FIGURE 4.20: Energy-dispersive X-ray Spectroscopy for AC8502Di

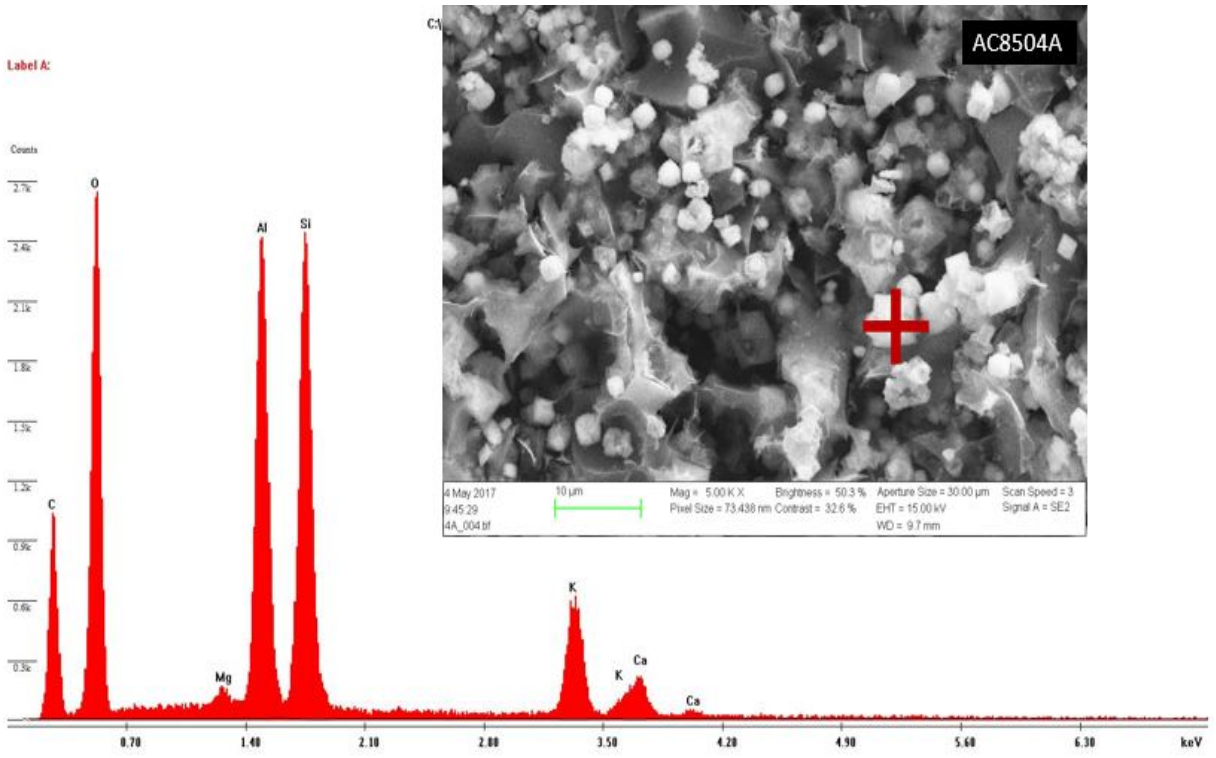

FIGURE 4.21: Energy-dispersive X-ray Spectroscopy for AC8504A

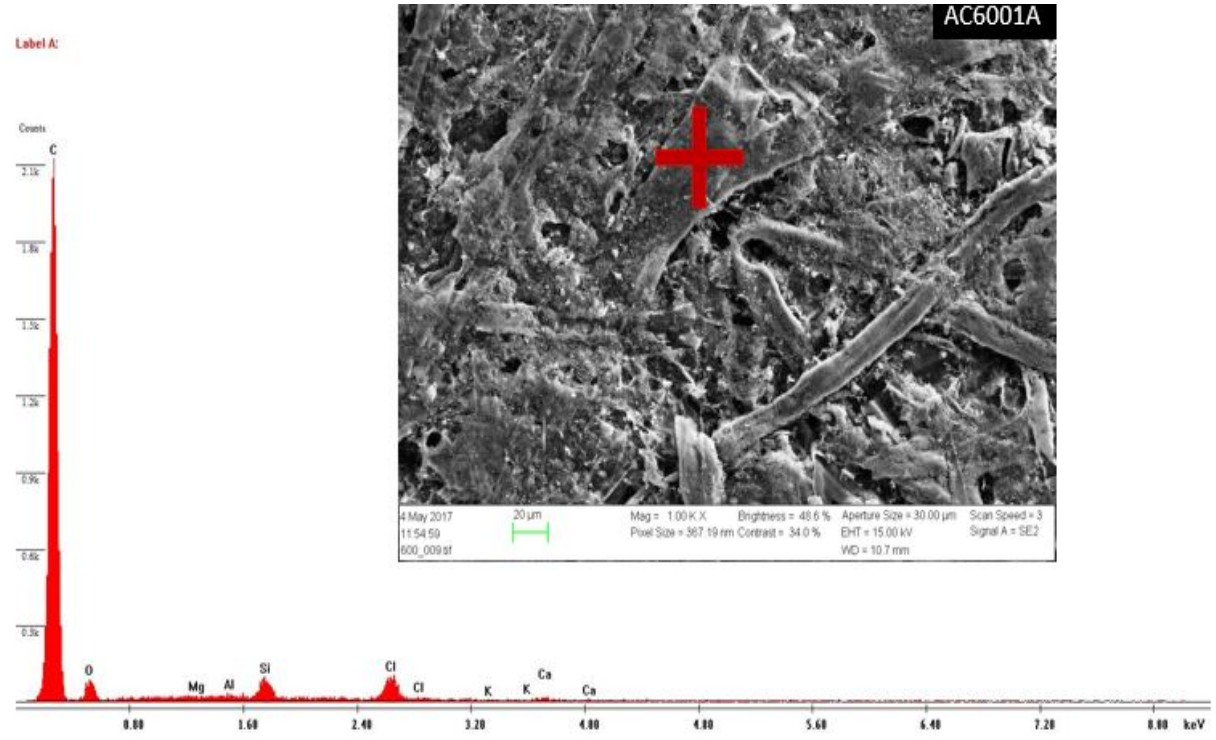

FIGURE 4.22: Energy-dispersive X-ray Spectroscopy for AC6001A

The Figures 4.19, 4.20, 4.21 and 4.22 show the Energy dispersive X-ray Spectroscopy charts for the four selected samples: AC8502B, AC8502Di, AC8504A, and AC6001A. The marked

point is the reference section for the EDX analysis. The vertical axis tells how much of each element the particle contains, while the horizontal bottom part shows the energy spectrum. Samples AC8502B and AC8502Di had the highest peaks from calcium, carbon and oxygen, with negligible amounts of potassium, magnesium, aluminium and silicon in the spectrum.

On the other hand, sample AC6001A just had carbon as the dominant element, with traces of chlorine, oxygen, potassium, magnesium, aluminium, and silicon in the spectrum. This tells us that the presence of carbon is not sufficient to have a high surface area and pore morphology.

Sample AC8504A had a fair mix of various components, which includes aluminium and silicon. The presence of these elements explains the irregularity of this sample's pore size distribution. The table below gives a glimpse of the elements required for a high surface area, and also elements responsible for distorting the surface structure of the samples.

TABLE 4.5: Elements and their energy levels on EDX

Sample	Carbon (%)	Calcium (%)	Oxygen (%)	Alumi-nium (%)	Silicon (%)	Magne-sium (%)	Chlorine (%)	Pota-ssium (%)
AC6001A	91	Trace	Trace	Trace	Trace	Trace	Trace	Trace
AC8504A	24.8	2.96	26.7	23.75	23.78	Trace	Trace	Trace
AC8502B	44.78	47.76	7.46	Trace	Trace	Trace	Trace	Trace
AC8502Di	36	41.57	22.47	Trace	Trace	Trace	Trace	Trace

4.3 Electrochemical Performance Analysis

Samples AC6001A and AC7001A were further modified by chemical activation with ammonia gas at 600 °C and 700 °C, and then with KOH at 850 °C for 1 hour to improve their surface properties. The result was two new samples: P600850T and P700850T with BET surface areas of 519.414 m^2/g and 104.8132 m^2/g respectively. These samples were used as electrodes to produce a supercapacitor. The performance was measured against a reference state-of-the art activated carbon sample (YP80F), and the result is shown in 4.6

TABLE 4.6: Comparison of capacitive performance

Sample	Specific Capacitance (F/g)	Energy Density(Wh/Kg)
YP80F	106	24.84
P600850T	110	25.78
P700850T	114	26.7

The values used in the table were calculated by using Equations (4.1) and (4.2), which are for the power density and specific capacitance respectively. The Energy density was obtained using (2.29).

$$P = \frac{V^2}{4W_{TS}R} \tag{4.1}$$

Where:

- P = Power density
- W_{TS} = Total weight
- R = Cell resistance

$$C = \frac{4It}{m\Delta V} \tag{4.2}$$

Where:

- C = Specific Capacitance
- t = Time in seconds
- m = Mass of cell
- ΔV = Voltage change

Table 4.6 shows that the modified samples performed better electrochemically as compared with the reference sample. They had values about twice that of the reference sample. Supercapacitors are known for having high power densities. The power density of sample P700850T was over 6 times greater than that of the reference sample (Table 4.6). This is really significant as it means higher value from the prepared samples.

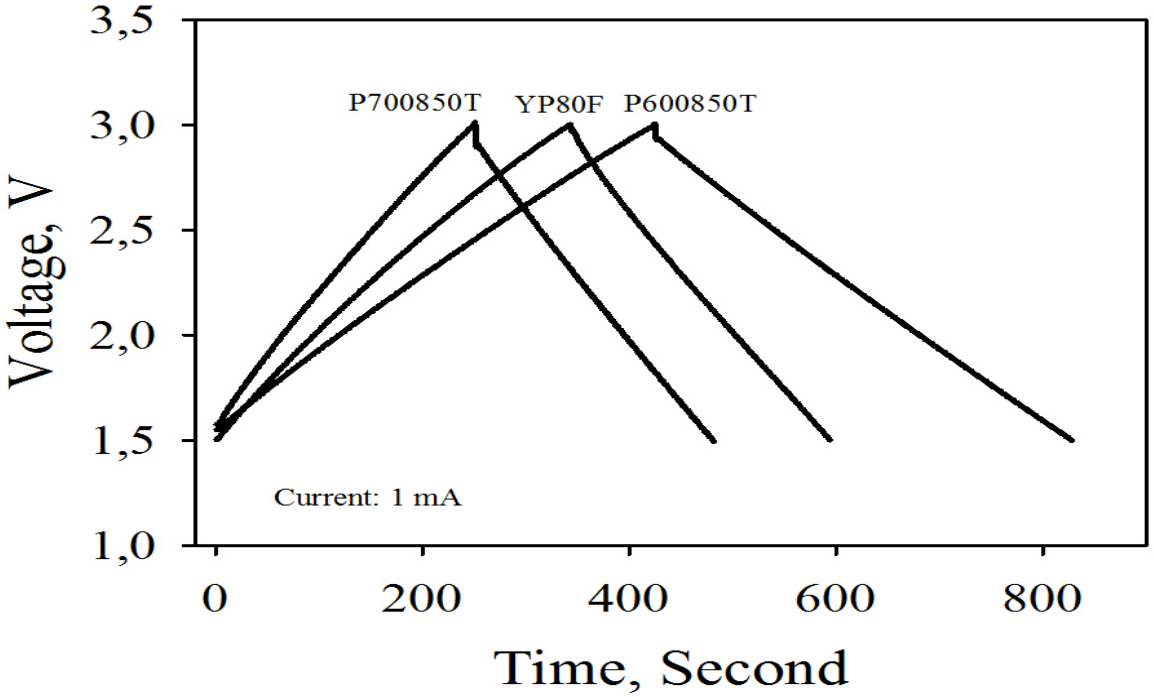

FIGURE 4.23: Constant current charge and discharge voltage profiles at 1 mA

.

Symmetrical supercapacitors were assembled by using P600850T, P700850T, and YP80F as electrode materials to evaluate the capacitive performances. The constant current charge and discharge voltage profiles between 1.5 and 3 V are presented in Figure 4.23. Accordingly, the specific capacitances are 110, 114, and 106 F/g for P600850T, P700850T, and YP80F, respectively. Therefore, activated carbons (P600850T, P700850T) produced in this project have higher specific capacitance compare to the state of the art commercial sample (YP80F). This indicates supercapacitors assembled with P600850T and P700850T as electrode materials have high specific energy compared to that with YP80F as electrode materials. The high specific capacitance of sample P600850T and P700850T can be ascribed to the high specific surface area and suitable pore size distribution, which ensures surface can be reached by the electrolyte and contribute to the capacitance.

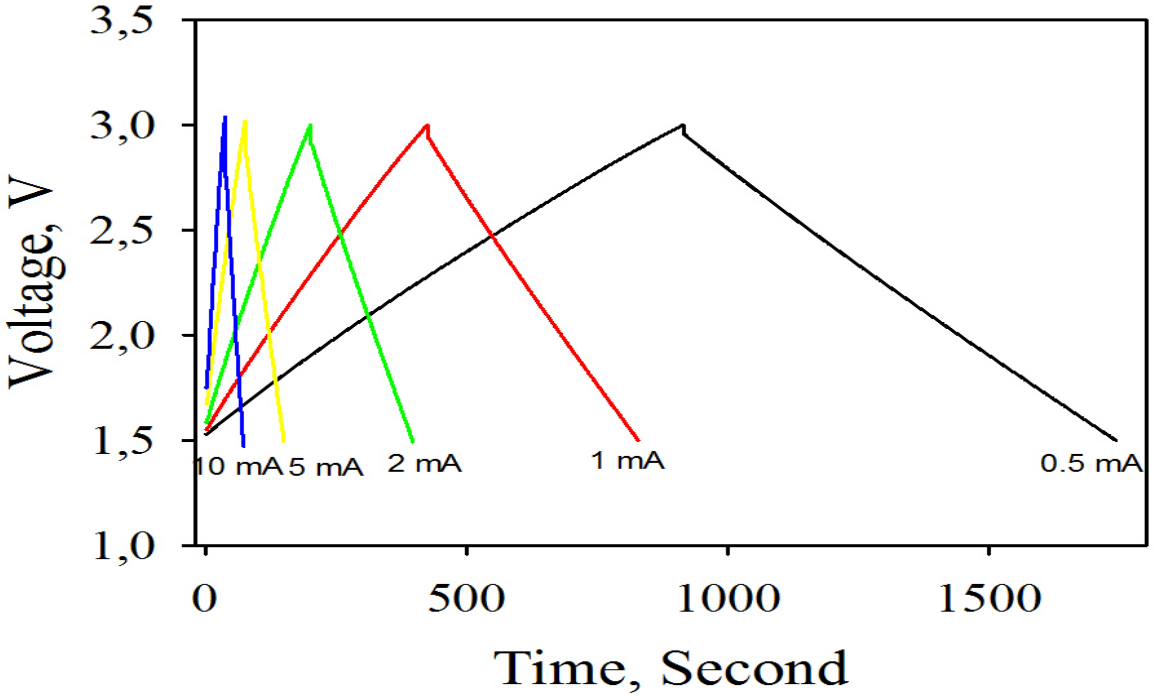

FIGURE 4.24: Charge and discharge voltage profiles of sample P600850T at different discharge current

.

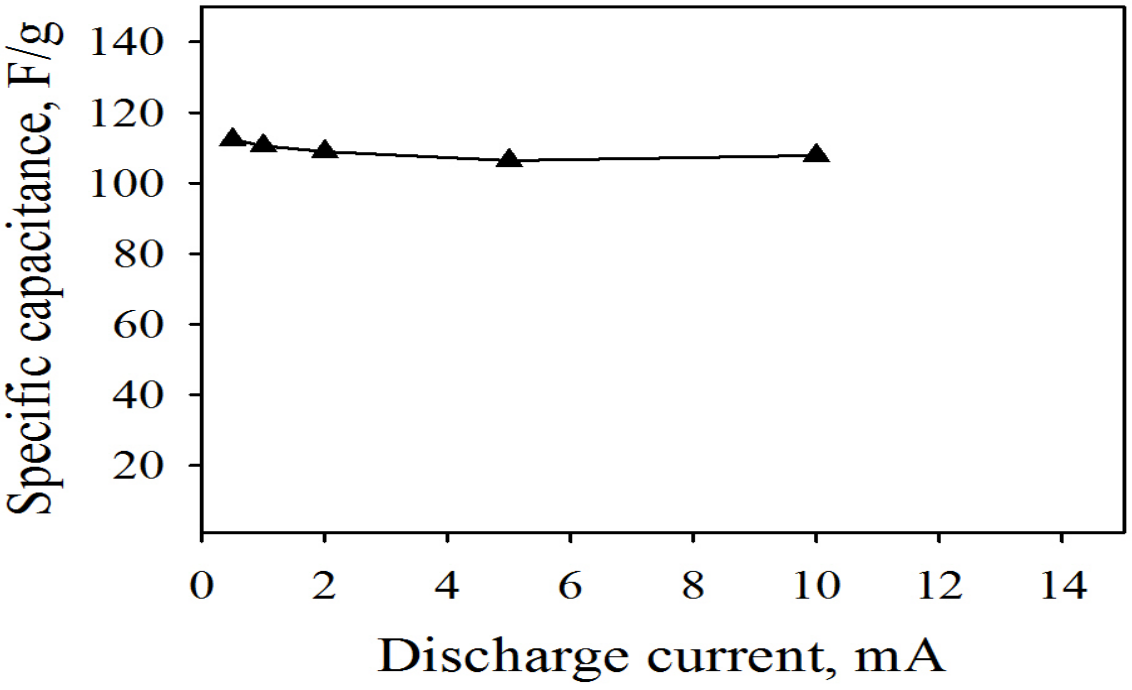

FIGURE 4.25: Rate capability of sample P600850T. The data is calculated according to 4.24

.

The rate capabilities were evaluated by cycling supercapacitors at different current. The constant current charge and discharge profiles of sample P600850T at different current are shown in Figure 4.24. The specific capacitances at different current are calculated and presented in Figure 4.25. According to Figure 4.25, the specific capacitances are 112, 110, 108, 106, and 107 at discharge currents of 0,5, 1, 2, 5, and 10 mA, respectively. Therefore, the specific capacitance decreases less than 4% when the discharge current increases 20 times. The confirms the good rate capability of sample P600850T. The charge and discharge time is only about 30 seconds, which means the fast response of this supercapacitor. The high rate capability of sample P600850T can be attribute to the favorable pore size distribution, which guarantees the fast electrolyte transfer in the activated carbon.

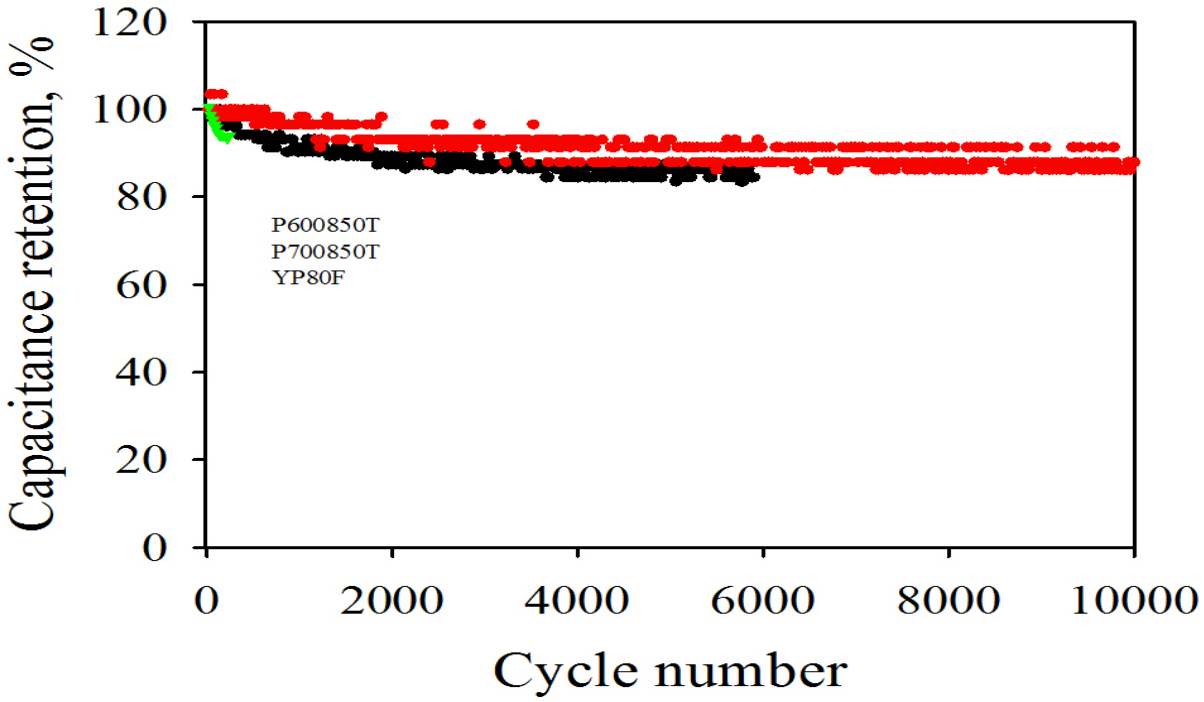

FIGURE 4.26: Cyclic stability of sample P600850T, P700850T, and YP80F

.

The stability of a supercapacitor determines its life time thus it is very important for practical application. Therefore, the cyclic stabilities of activated carbons were evaluated by cycling the supercapacitors at a charge and discharge current of 5 mA between 1,5 and 3 V at room temperature. According to Figure 4.26, all three samples suffer from mild capacitance loss at the very beginning. This can be attributed to the impurities presented in the supercapacitors. However, reference sample YP80F has a fast capacitance loss, while sample P600850T, P700850T are relatively stable. YP80F shows a capacitance loss of about 7% after only 250 cycles. P600850T shows a capacitance retention of over 85% after 6000 cycles. Moreover, P700850T shows a capacitance retention of about 90% after 10000 cycles. This indicates the high cyclic stability of activated carbon produced in this project. A few reasons can cause capacitance loss, such as the

active material loss electrical contact with current collector, impurity presence in the activated carbon, surface function group on the activated carbon surface, impurities in the electrolyte, and the water and oxygen left in the system. Electrolytes used in these three capacitors are same and the only difference is the electrode materials. Therefore, the low stability of YP80F is due to either impurity or surface functional group. P600850T and P700850T were washed carefully with hot hydrochloric acid to remove impurities. A post thermal treatment at 1000 °C for 2 hours under nitrogen will eliminate most of the surface functional group. These two step treatments ensures the high purity of P600850T and P700850T and thus the cyclic stability.

Chapter 5

Conclusion

5.1 Conclusion

A series of activated carbon was prepared from waste paper by physical activation, chemical activation, and a combination of both procedures. The chemical activation was done by alternating phosphoric acid and potassium hydroxide with ammonia and nitrogen as preparatory gases. Several modifications were made to optimise the quality of the final product; such as varying the temperature, impregnation ratio, activation steps and chemical agents.

The best sample had a surface area of 1014 m^2/g. This shows that activated carbon with high surface areas can be obtained from waste papers using KOH and adopting a temperature of 850 °C. This sample, in addition to others was studied under a Scanning Electron Microscope with an Energy-dispersive X-ray Spectroscopy analyzer. It was discovered that samples with high surface areas had similar dominant elements (carbon, calcium and oxygen) in their energy spectrum. Table 4.5 contains these details.

On the other hand, samples with low surface areas either had high energy levels of just carbon, or a fair mix of the three elements (carbon, calcium and oxygen) and peaks from aluminium and silicon.

The Samples were analysed using nitrogen physisorption to study the surface area and porosity. They were both microporous and mesoporous covering types 1A, 1B, 2, 3, 4 and 5 isotherm classes. The difference in sample characteristics could be traced to pre-carbonization conditions which is responsible for mesoporosity development, while the activation by KOH controls microporosity upgrowth.

Activated carbon has various applications, amongst which is the use as electrode for supercapacitors. Here, the surface area is extremely important as a larger surface space ensures that

more charge can be accomodated, and hence, higher specific capacitance. From the prepared samples, it is recommended that the best surface areas for the preparation of activated carbons from waste papers using KOH can be obtained by adopting a temperature of 850 °C for 120 minutes, with an impregnation ratio of either 1:1 or 2:1 (KOH:Precursor).

As electrodes for supercapacitors, the produced activated carbon sample exhibited higher performances than the reference state-of-the art sample from a recognized supplier (see Table 4.6). The cyclic stability of the prepared samples (P600850T, P700850T) were compared with that of the reference sample (YP80F), P700850T showed a capacitance retention of about 90% after 10000 cycles, while YP80F showed a capacitance loss of about 7% after only 250 cycles (see Figure 4.26). This rapid loss of capacity by the reference sample was attributed to the presence of impurities. This was avoided in the prepared samples by post treatment with hydrochloric acid. Hence, the higher cyclic stability (see Chapter 4). This shows a successful utilization of a waste material.

Chapter 6

Suggestions for further work

Asides from the fact that this thesis was successfully carried out, there is still some room for improvement.

On Material Characterization: The pore size distribution analysis was done by the BJH method which focuses on mesoporosity, based on the Kelvin equation. There are however, models [99] that have been designed to capture the microporosity details. some of these are presented below:

- MP Procedure
- Dubinin-Radushkevich method
- Dubinin-Astakhov analysis
- Horvath-Kawazoe equation
- Cylindrical pore model extensions of:
  - Saito and Foley
  - Cheng and Yang
- Cheng and Yang model with regard to nonlinearity

On Further Increase in Surface area: The application of zinc chloride as chemical agent can further improve the surface area of the activated carbon. There has been recorded cases of surface areas as high as 2000 m^2/g. Also, gasification with carbon IV oxide is another suggestion that could improve the surface area of the prepared samples [107].

The use of other kinds waste materials like sea weed blended with some of the chemical agents presented in this work could be a cost effective means of making activated carbon. This is because sea weed already contains some salts, and the presence of salts have recently been associated with high capacitance values, irreespective of the surface area [105].

Bibliography

[1] Parliament, 2006. URL www.parliament.uk.

[2] Wikipedia. Plug-in electric vehicles in norway., 2017. URL https://en.wikipedia.org/wiki/Plug-in_electric_vehicles_in_Norway.

[3] Jones. Standard electrode potential. Online, 2016. URL https://www.youtube.com/watch?v=TX96ib6JCVw. YouTube.

[4] APS. Lithium ion batteries: Delivering a charge. *American Physical Society*, 2017.

[5] Hassan Zehra. Fuel cells and batteries. June 2017. URL http://www.uobabylon.edu.iq/eprints/paper_4_22488_736.pdf.

[6] Martin Winter and Ralph J Brodd. What are batteries, fuel cells, and supercapacitors?, 2004.

[7] Craig A. Batteries and energy storage. Battery Workshop.

[8] Wheatcroft. What is a supercapacitor. *Energy Storage CDT*, 2016.

[9] et. al Virginia Hernández-Montoya. *Lignocellulosic Precursors Used in the Synthesis of Activated Carbon - Characterization Techniques and Applications*. Number 19-36. InTech, China, 2012. Chapter 2.

[10] Rajveer Bhaskar. Adsorption. LinkedIn Slideshare, 2014. URL https://www.slideshare.net/RajveerBhaskar/adsorption-final-34896946. Linkedin Corporation.

[11] Zhixin Yu. Catalyst characterization. November 2016.

[12] Ana María Valenzuela-Muñiz. Abc's of electrochemistry series materials characterization techniques: Surface area and pore size distribution. Lecture Presentation, February 2012.

[13] Hokosawa Micron Powder Systems. Activated carbon. Online Website, May 2017. URL https://www.hmicronpowder.com/industries/chemical/activated-carbon.

[14] University of Wisconsin-Madison. Building safety gas cylinders. University Website, March 2016. URL https://biochem.wisc.edu/intranet/building/safety/gas-cylinders. College of Agricultural and Life Sciences.

[15] Winnipeg Online News. Winnipeg news research centre. Website, June 2017. URL http://guides.wpl.winnipeg.ca/c.php?g=524622&p=3586977.

[16] 24" three zones split tube furnace with optional quartz tube & flange (60 - 130mm, 1200°c max.) - otf-1200x-iii-s-ul. Online website, 2017. URL http://www.mtixtl.com/tubefurnace-OTF-1200X-III-S-UL.aspx. Superstore for Material Researchers and Engineers.

[17] H Ralph, S William, F Geoffrey Herring, and D Madura Jeffrey. General chemistry: Principles and modern applications. *Prentice Hall*, page 606, 2007.

[18] Walter Benenson, John W Harris, Horst Stöcker, and Holger Lutz. *Handbook of physics*. Springer Science & Business Media, 2006.

[19] Qinghua Tian. Impressive lithium storage properties of layered sodium titanate with hierarchical nanostructures as anode materials for lithium-ion batteries. *Journal of Alloys and Compounds*, 2017.

[20] Shaofeng Wang, Yanping Zhu, Xiaomin Xu, Jaka Sunarso, and Zongping Shao. Adsorption-based synthesis of co 3 o 4/c composite anode for high performance lithium-ion batteries. *Energy*, 125:569–575, 2017.

[21] Chenpei Yuan, Heng-guo Wang, Jiaqi Liu, Qiong Wu, Qian Duan, and Yanhui Li. Facile synthesis of co 3 o 4-ceo 2 composite oxide nanotubes and their multifunctional applications for lithium ion batteries and co oxidation. *Journal of Colloid and Interface Science*, 494:274–281, 2017.

[22] Hongyan He, Dan Li, and Mingqi Li. Electrochemical performance and reaction mechanism of the li2moo3 anode synthesized by ball milling and thermal reduction for lithium-ion batteries. *Electrochimica Acta*, 224:1–8, 2017.

[23] J Sherbondy J, Mickler. What is activated carbon? Website, 2015. URL http://www.tigg.com/what-is-activated-carbon.html.

[24] HayCarb. Acivated carbon basics. Online Website, April 2017. URL http://www.haycarb.com/activated-carbon.

[25] Kamya Parashar. Adsorption presentation. Slideshare, April 2015. URL https://www.slideshare.net/Kamyaparashar/adsorption-presentation-44669901. Linked In.

[26] Bruno Scrosati. History of lithium batteries. *Journal of solid state electrochemistry*, 15 (7-8):1623–1630, 2011.

[27] Joost Mertens. Shocks and sparks: the voltaic pile as a demonstration device. *Isis*, 89 (2):300–311, 1998.

[28] MR Palacin. Recent advances in rechargeable battery materials: a chemist's perspective. *Chemical Society reviews*, 38(9):2565, 2009.

[29] Jung-Ki Park. *Principles and applications of lithium secondary batteries*. John Wiley & Sons, 2012.

[30] EIA. Outlook, annual energy and others. *Department of Energy*, 92010(9), 2010.

[31] BBC. Bbc news, 2006.

[32] BP. Bp statistical review of world energy. London, 2016. p. 1 -10.

[33] The Guardian. Guardian climate change, 2014. URL https://www.theguardian.com/environment/climate-change. p.1.

[34] Eurostat. Greenhouse gas emission statistics. Online, 2016. URL http://ec.europa.eu/eurostat/statistics-explained/index.php/Greenhouse_gas_emission_statistics. p.1.

[35] Christopher Brett, MA Oliveira Brett, Ana María Christopher MA Brett, and Ana Maria Oliveira Brett. *Electrochemistry: principles, methods, and applications*. Number 544.6 BRE. 1993.

[36] Bui Matthew and Wen Chung Chou. Electrochemistry basics. University of California Davis: California., 2016.

[37] CJ Miller and I Rubinstein. Physical electrochemistry: Principles, methods and applications. *Rubinstein, I., Ed*, pages 27–79, 1995.

[38] Hiroaki Kobayashi, Mitsuhiro Hibino, Tetsuya Makimoto, Yoshiyuki Ogasawara, Kazuya Yamaguchi, Tetsuichi Kudo, Shin-ichi Okuoka, Hironobu Ono, Koji Yonehara, Yasutaka Sumida, et al. Synthesis of cu-doped li 2 o and its cathode properties for lithium-ion batteries based on oxide/peroxide redox reactions. *Journal of Power Sources*, 340:365–372, 2017.

[39] Ali Eftekhari. Low voltage anode materials for lithium-ion batteries. *Energy Storage Materials*, 2017.

[40] Yu-Ping Wu, Elke Rahm, and Rudolf Holze. Carbon anode materials for lithium ion batteries. *Journal of Power Sources*, 114(2):228–236, 2003.

[41] A Magasinski, P Dixon, B Hertzberg, A Kvit, J_ Ayala, and G Yushin. High-performance lithium-ion anodes using a hierarchical bottom-up approach. *Nature materials*, 9(4):353–358, 2010.

[42] Subrahmanyam Goriparti, Ermanno Miele, Francesco De Angelis, Enzo Di Fabrizio, Remo Proietti Zaccaria, and Claudio Capiglia. Review on recent progress of nanostructured anode materials for li-ion batteries. *Journal of Power Sources*, 257:421–443, 2014.

[43] Xiaofeng Tu, Yingke Zhou, and Yijie Song. Freeze-drying synthesis of three-dimensional porous lifepo 4 modified with well-dispersed nitrogen-doped carbon nanotubes for high-performance lithium-ion batteries. *Applied Surface Science*, 400:329–338, 2017.

[44] Guangmin Zhou, Da-Wei Wang, Feng Li, Lili Zhang, Na Li, Zhong-Shuai Wu, Lei Wen, Gao Qing Lu, and Hui-Ming Cheng. Graphene-wrapped fe3o4 anode material with improved reversible capacity and cyclic stability for lithium ion batteries. *Chemistry of Materials*, 22(18):5306–5313, 2010.

[45] Gaelle Derrien, Jusef Hassoun, Stefania Panero, and Bruno Scrosati. Nanostructured sn–c composite as an advanced anode material in high-performance lithium-ion batteries. *Advanced Materials*, 19(17):2336–2340, 2007.

[46] Xianjun Zhu, Yanwu Zhu, Shanthi Murali, Meryl D Stoller, and Rodney S Ruoff. Nanostructured reduced graphene oxide/fe2o3 composite as a high-performance anode material for lithium ion batteries. *ACS nano*, 5(4):3333–3338, 2011.

[47] Hong Li, Xuejie Huang, Liquan Chen, Zhengang Wu, and Yong Liang. A high capacity nano si composite anode material for lithium rechargeable batteries. *Electrochemical and Solid-State Letters*, 2(11):547–549, 1999.

[48] Zhong-Shuai Wu, Wencai Ren, Lei Wen, Libo Gao, Jinping Zhao, Zongping Chen, Guangmin Zhou, Feng Li, and Hui-Ming Cheng. Graphene anchored with co3o4 nanoparticles as anode of lithium ion batteries with enhanced reversible capacity and cyclic performance. *ACS nano*, 4(6):3187–3194, 2010.

[49] Kun Chang, Weixiang Chen, Lin Ma, Hui Li, He Li, Feihe Huang, Zhude Xu, Qingbo Zhang, and Jim-Yang Lee. Graphene-like mos 2/amorphous carbon composites with high capacity and excellent stability as anode materials for lithium ion batteries. *Journal of Materials Chemistry*, 21(17):6251–6257, 2011.

[50] Qinghua Tian, Jizhang Chen, Zhengxi Zhang, and Li Yang. Fabrication of tio 2 in-situ decorated and hierarchical li 4 ti 5 o 12 for improved lithium storage. *Electrochimica Acta*, 231:670–676, 2017.

[51] Abhishek Jaiswal. Lithium-ion battery based renewable energy solution for off-grid electricity: A techno-economic analysis. *Renewable and Sustainable Energy Reviews*, 72: 922–934, 2017.

[52] J-M Tarascon and Michel Armand. Issues and challenges facing rechargeable lithium batteries. *Nature*, 414(6861):359–367, 2001.

[53] Sung Hollister. Here's why samsung note 7 phones are catching fire. Online, 2016. C-NET.

[54] BML Rao, RW Francis, and HA Christopher. Lithium-aluminum electrode. *Journal of The Electrochemical Society*, 124(10):1490–1492, 1977.

[55] Fo Lou. High performance lithium ion capacitor. *Graphene Power: Stavanger*, 2016.

[56] John R Miller and Patrice Simon. Fundamentals of electrochemical capacitor design and operation. *Electrochemical Society Interface*, 17(1):31–32, 2008.

[57] Yu Liu and Xinsheng Peng. Recent advances of supercapacitors based on two-dimensional materials. *Applied Materials Today*, 7:1–12, 2017.

[58] Xin Yao and Yanli Zhao. Three-dimensional porous graphene networks and hybrids for lithium-ion batteries and supercapacitors. *Chem*, 2(2):171–200, 2017.

[59] Rachit Malik, Lu Zhang, Colin McConnell, Michael Schott, Yu-Yun Hsieh, Ryan Noga, Noe T Alvarez, and Vesselin Shanov. Three-dimensional, free-standing polyaniline/carbon nanotube composite-based electrode for high-performance supercapacitors. *Carbon*, 116:579–590, 2017.

[60] Hongwei Che, Yamei Lv, Aifeng Liu, Jingbo Mu, Xiaoliang Zhang, and Yongmei Bai. Facile synthesis of three dimensional flower-like co 3 o 4@ mno 2 core-shell microspheres as high-performance electrode materials for supercapacitors. *Ceramics International*, 43 (8):6054–6062, 2017.

[61] Che-Hsien Lin, Chuen-Horng Tsai, Fan-Gang Tseng, I-Ching Chen, and Chien-Kuo Hsieh. Electrochemical pulse deposition of ni nanoparticles on the 3d graphene network to synthesize vertical cnfs as the full-carbon hybrid nanoarchitecture for supercapacitors. *Materials Letters*, 192:40–43, 2017.

[62] Baogang Quan, Yuena Meng, Lin Li, Zehan Yao, Zhe Liu, Kai Wang, Zhixiang Wei, Changzhi Gu, and Junjie Li. Vertical few-layer graphene/metalized si-nanocone arrays as 3d electrodes for solid-state supercapacitors with large areal capacitance and superior rate capability. *Applied Surface Science*, 404:238–245, 2017.

[63] Yanrong Li, Xue Wang, Qi Yang, Muhammad Sufyan Javed, Qipeng Liu, Weina Xu, Chenguo Hu, and Dapeng Wei. Ultra-fine cuo nanoparticles embedded in three-dimensional graphene network nano-structure for high-performance flexible supercapacitors. *Electrochimica Acta*, 234:63–70, 2017.

[64] Pang.et.al. One-pot synthesisof heterogenous co3o4-nanocube/co(oh)2-nanosheet hybrids for high-performance flexible asymmetric all-solid-state supercapacitors. *Nano Energy*, 2017.

[65] Dong Zhou, Huanlei Wang, Nan Mao, Yanran Chen, Ying Zhou, Taiping Yin, Hui Xie, Wei Liu, Shougang Chen, and Xin Wang. High energy supercapacitors based on interconnected porous carbon nanosheets with ionic liquid electrolyte. *Microporous and Mesoporous Materials*, 2017.

[66] Zhongchun Li, Lei Wu, Liangbiao Wang, Aijun Gu, and Quanfa Zhou. Nickel cobalt sulfide nanosheets uniformly anchored on porous graphitic carbon nitride for supercapacitors with high cycling performance. *Electrochimica Acta*, 231:617–625, 2017.

[67] Longjing Luo, Tianmo Liu, Shuo Zhang, Bin Ke, Le Yu, Shahid Hussain, and Liyang Lin. Hierarchical co 3 o 4@ znwo 4 core/shell nanostructures on nickel foam: synthesis and electrochemical performance for supercapacitors. *Ceramics International*, 2017.

[68] Karthikeyan Gopalsamy, Jayaraman Balamurugan, Tran Duy Thanh, Nam Hoon Kim, and Joong Hee Lee. Fabrication of nitrogen and sulfur co-doped graphene nanoribbons with porous architecture for high-performance supercapacitors. *Chemical Engineering Journal*, 312:180–190, 2017.

[69] Qin Yang, Ran Bi, Kam-chuen Yung, and Michael Pecht. Electrochemically reduced graphene oxides/nanostructured iron oxides as binder-free electrodes for supercapacitors. *Electrochimica Acta*, 231:125–134, 2017.

[70] Lingjuan Deng, Yuanzi Gu, Yihong Gao, Zhanying Ma, and Guang Fan. Carbon nanotubes/holey graphene hybrid film as binder-free electrode for flexible supercapacitors. *Journal of Colloid and Interface Science*, 494:355–362, 2017.

[71] Dongdong Zhang, Jianghong Zhao, Chong Feng, Rijie Zhao, Yahui Sun, Taotao Guan, Baixin Han, Nan Tang, Jianlong Wang, Kaixi Li, et al. Scalable synthesis of hierarchical macropore-rich activated carbon microspheres assembled by carbon nanoparticles for high rate performance supercapacitors. *Journal of Power Sources*, 342:363–370, 2017.

[72] New World Encyclopedia Contributors. Activated carbon. Encyclopedia, February 2016. URL http://www.newworldencyclopedia.org/entry/Activated_carbon#.

[73] Shijie Li, Kuihua Han, Jinxiao Li, Ming Li, and Chunmei Lu. Preparation and characterization of super activated carbon produced from gulfweed by koh activation. *Microporous and Mesoporous Materials*, 243:291–300, 2017.

[74] Yujiao Kan, Qinyan Yue, Dong Li, Yuwei Wu, and Baoyu Gao. Preparation and characterization of activated carbons from waste tea by h 3 po 4 activation in different atmospheres for oxytetracycline removal. *Journal of the Taiwan Institute of Chemical Engineers*, 71: 494–500, 2017.

[75] Guizhen Li, Jiaxiong Li, Wei Tan, Hai Jin, Huaixian Yang, Jinhui Peng, Colin J Barrow, Min Yang, Hongbin Wang, and Wenrong Yang. Preparation and characterization of the

hydrogen storage activated carbon from coffee shell by microwave irradiation and koh activation. *International Biodeterioration & Biodegradation*, 113:386–390, 2016.

[76] Nor Adilla Rashidi and Suzana Yusup. A review on recent technological advancement in the activated carbon production from oil palm wastes. *Chemical Engineering Journal*, 2016.

[77] Pascal S Thue, Matthew A Adebayo, Eder C Lima, Joseph M Sieliechi, Fernando M Machado, GL Dotto, Julio CP Vaghetti, and Silvio LP Dias. Preparation, characterization and application of microwave-assisted activated carbons from wood chips for removal of phenol from aqueous solution. *Journal of Molecular Liquids*, 223:1067–1080, 2016.

[78] Yuxiang Huang, Erni Ma, and Guangjie Zhao. Thermal and structure analysis on reaction mechanisms during the preparation of activated carbon fibers by koh activation from liquefied wood-based fibers. *Industrial Crops and Products*, 69:447–455, 2015.

[79] Chiung-Fen Chang, Ching-Yuan Chang, and Wen-Tien Tsai. Effects of burn-off and activation temperature on preparation of activated carbon from corn cob agrowaste by co2 and steam. *Journal of Colloid and Interface Science*, 232(1):45–49, 2000.

[80] Dechen Liu, Wenli Zhang, Haibo Lin, Yang Li, Haiyan Lu, and Yan Wang. A green technology for the preparation of high capacitance rice husk-based activated carbon. *Journal of Cleaner Production*, 112:1190–1198, 2016.

[81] Elisabeth Schröder, Klaus Thomauske, Christine Weber, Andreas Hornung, and Vander Tumiatti. Experiments on the generation of activated carbon from biomass. *Journal of analytical and applied pyrolysis*, 79(1):106–111, 2007.

[82] K Kadirvelu, P Senthilkumar, K Thamaraiselvi, and V Subburam. Activated carbon prepared from biomass as adsorbent: elimination of ni (ii) from aqueous solution. *Bioresource technology*, 81(1):87–90, 2002.

[83] Wei Luo, Bao Wang, Christopher G Heron, Marshall J Allen, Jeff Morre, Claudia S Maier, William F Stickle, and Xiulei Ji. Pyrolysis of cellulose under ammonia leads to nitrogen-doped nanoporous carbon generated through methane formation. *Nano letters*, 14(4):2225–2229, 2014.

[84] Kirill Murashko, Daria Nevstrueva, Arto Pihlajamäki, Tuomas Koiranen, and Juha Pyrhönen. Cellulose and activated carbon based flexible electrical double-layer capacitor electrode: Preparation and characterization. *Energy*, 119:435–441, 2017.

[85] Miao Yu, Yingying Han, Jian Li, and Lijuan Wang. Co 2-activated porous carbon derived from cattail biomass for removal of malachite green dye and application as supercapacitors. *Chemical Engineering Journal*, 317:493–502, 2017.

[86] Yan Han, Na Shen, Shu Zhang, Dejun Li, and Xifei Li. Fish gill-derived activated carbon for supercapacitor application. *Journal of Alloys and Compounds*, 694:636–642, 2017.

[87] Yuan Gao, Shiping Xu, Sinem Ortaboy, Yujiao Kan, Qinyan Yue, and Baoyu Gao. Preparation of well-developed mesoporous activated carbon with high yield by ammonium polyphosphate activation. *Journal of the Taiwan Institute of Chemical Engineers*, 66: 394–399, 2016.

[88] Seiji Kumagai, Masaki Hatomi, and Daisuke Tashima. Electrochemical performance of microporous and mesoporous activated carbons in neat and diluted 1-ethyl-3-methylimidazolium tetrafluoroborate. *Journal of Power Sources*, 343:303–315, 2017.

[89] VK Gupta, Bina Gupta, Arshi Rastogi, Shilpi Agarwal, and Arunima Nayak. A comparative investigation on adsorption performances of mesoporous activated carbon prepared from waste rubber tire and activated carbon for a hazardous azo dye—acid blue 113. *Journal of Hazardous Materials*, 186(1):891–901, 2011.

[90] Orawan Sirichote, Wanna Innajitara, Laemthong Chuenchom, Doungporn Chunchit, Kanokrat Naweekan, et al. Adsorption of iron (iii) ion on activated carbons obtained from bagasse, pericarp of rubber fruit and coconut shell. *Songklanakarin J. Sci. Tech*, 24:235–242, 2002.

[91] SE Abechi, CE Gimba, A Uzairu, and YA Dallatu. Preparation and characterization of activated carbon from palm kernel shell by chemical activation. *Res. J. Chem. Sci*, 3(7): 54–61, 2013.

[92] Collin G Joseph, Hasnul Fazli Md Zain, and Siti Fatimah Dek. Treatment of landfill leachate in kayu madang, sabah: textural and physical characterization (part 1). *Malays J Anal Sci*, 10(1):1–6, 2006.

[93] Carlos Moreno-Castilla, Francisco Carrasco-Marin, M Victoria Lopez-Ramon, and Miguel A Alvarez-Merino. Chemical and physical activation of olive-mill waste water to produce activated carbons. *Carbon*, 39(9):1415–1420, 2001.

[94] Luiz CA Oliveira, Rachel VRA Rios, Jose D Fabris, V Garg, Karim Sapag, and Rochel M Lago. Activated carbon/iron oxide magnetic composites for the adsorption of contaminants in water. *Carbon*, 40(12):2177–2183, 2002.

[95] Kei Mizuta, Toshitatsu Matsumoto, Yasuo Hatate, Keiichi Nishihara, and Tomoki Nakanishi. Removal of nitrate-nitrogen from drinking water using bamboo powder charcoal. *Bioresource technology*, 95(3):255–257, 2004.

[96] Jyotsna Goel, Krishna Kadirvelu, Chitra Rajagopal, and Vinod Kumar Garg. Removal of lead (ii) by adsorption using treated granular activated carbon: batch and column studies. *Journal of hazardous materials*, 125(1):211–220, 2005.

[97] Lei Li, Patricia A Quinlivan, and Detlef RU Knappe. Effects of activated carbon surface chemistry and pore structure on the adsorption of organic contaminants from aqueous solution. *Carbon*, 40(12):2085–2100, 2002.

[98] IAW Tan, A La Ahmad, and BH Hameed. Adsorption of basic dye on high-surface-area activated carbon prepared from coconut husk: Equilibrium, kinetic and thermodynamic studies. *Journal of hazardous materials*, 154(1):337–346, 2008.

[99] Paul Webb Orr and Clyde. *Analytical Methods in Fine Particle Technology*. Micromeritics, Georgia, 1 edition, 1999.

[100] Zulkiffli Bakar. Characteristics of powders and porous solids. LinkedIn Slideshare, 2013. URL https://www.slideshare.net/chemiestar188979/seminar-core-slides-malaysia-dec-2013. Malaysia Slideshare.

[101] P.Eng. Hari Goyal, MS. What is the chemical composition of paper? PULP & PAPER RESOURCES & INFORMATION SITE, May 2017. URL http://www.paperonweb.com/A1056.htm.

[102] Micromeritics. micromeritics product showcase. Website, June 2017. URL http://www.micromeritics.com/Product-Showcase.aspx.

[103] Particle Analytical. Bet introduction to bet (brunauer, emmett and teller). Website, 2017. URL http://particle.dk/methods-analytical-laboratory/surface-area-bet-2/.

[104] Roger Robbins. *Scanning Electron Microscope Operation*. University of texas dallas, University of texas dallas, September 2015. URL https://www.utdallas.edu/~rar011300/SEM/Scanning%20Electron%20Microscope%20Operation.pdf. Scanning Electron Microscope Operation Zeiss Supra-40.

[105] Abdelhakim Elmouwahidi, Esther Bailón-García, Agustín F Pérez-Cadenas, Francisco J Maldonado-Hódar, and Francisco Carrasco-Marín. Activated carbons from koh and h 3 po 4-activation of olive residues and its application as supercapacitor electrodes. *Electrochimica Acta*, 229:219–228, 2017.

[106] Aik Chong Lua and Ting Yang. Effect of activation temperature on the textural and chemical properties of potassium hydroxide activated carbon prepared from pistachio-nut shell. *Journal of colloid and interface science*, 274(2):594–601, 2004.

[107] WT Tsai, CY Chang, SY Wang, CF Chang, SF Chien, and HF Sun. Preparation of activated carbons from corn cob catalyzed by potassium salts and subsequent gasification with co 2. *Bioresource technology*, 78(2):203–208, 2001.